Tarduno, J.A., Duncan, R.A., Scholl, D.W., et al., 2002
Proceedings of the Ocean Drilling Program, Initial Reports Volume 197

6. SITE 1206[1]

Shipboard Scientific Party[2]

BACKGROUND AND SCIENTIFIC OBJECTIVES

Koko Seamount lies at the southern end of the Emperor Seamount chain of volcanoes, ~200 km north of the major inflection ("bend") in the Hawaiian-Emperor lineament. It is also the youngest site in our transect to investigate the paleolatitude history of the Hawaiian hotspot (see the **"Leg 197 Summary"** chapter). The seamount was named for the 58th emperor of Japan (A.D. 885–887) by Davies et al. (1972), who reported the results of bathymetric and seismic surveys and the contents of two dredge hauls (*Thomas Washington*'s Aries-7 cruise) (see **"Underway Geophysics"** p. 24). The gross structure of the seamount is that of an elongate volcanic edifice, aligned northwest-southeast, oblique to the main trend of the Emperor Seamounts. A prominent south-trending ridge extends ~50 km from the summit area toward Kimmei Seamount (Fig. **F1**). Undoubtedly, the basement pedestal of Koko Seamount is a plexus of coalesced volcanoes, much like many of the larger seamounts in this chain, including Nintoku Seamount (Site 1205), but Koko Seamount is covered by a thick carbonate cap that obscures definition of distinct volcanic centers (Davies et al., 1972). The complex is, however, clearly isolated by abyssal depths from Ojin Seamount, ~200 km to the north, and Kimmei Seamount, ~100 km to the south (Fig. **F1**).

In seismic reflection profile, the main edifice of Koko Seamount rises steeply from >5000 m as predominantly unsedimented 7°–9° volcanic slopes to a sedimented summit region that climbs gradually from ~1500 m to a broad plateau of ~500 m depth (Greene et al., 1980). The area of the summit plateau is ~5800 km². Davies et al. (1972) first identified Koko Seamount as a guyot. From analysis of seismic reflection survey data (Dalrymple et al., 1980) and core material recovered during drilling at Deep Sea Drilling Project (DSDP) Sites 308 and 309 (Larson, Moberly, et al., 1975), Greene et al. (1980) proposed that Koko Sea-

F1. Bathymetry in the Koko Seamount region, p. 28.

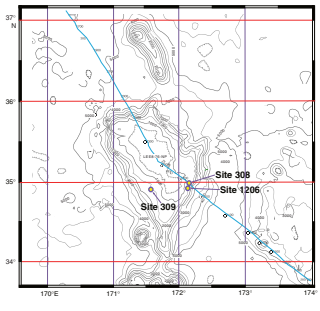

[1]Examples of how to reference the whole or part of this volume.
[2]Shipboard Scientific Party addresses.

mount was a mature carbonate bank or atoll with a nearly circular lagoon and fringing reefs surrounded by depositional terraces. The presence of bryozoans, coral, and ooliths indicates a warm-water carbonate ecosystem (Larson, Moberly, et al., 1975), and the presumed thickness of these deposits (>200 m) suggests that this guyot remained in warm, shallow water longer than any of the other Emperor Seamounts. McKenzie et al. (1980) applied the Schlanger and Konishi (1975) shallow-water carbonate facies model to speculate that in Eocene time Koko Seamount occupied a paleolatitude corresponding to a modern 20° to 22°N, at the boundary between massive coral-algal reef complexes and reef complexes mixed with bryozoan-algal biostromes, sand, and bioclastic debris.

The volcanic surface of Koko Seamount apparently remained at or above sea level long enough to be almost completely flattened by subaerial erosion and wave action. Extensive carbonate sedimentation kept up with subsidence of the volcanic complex until the island moved north out of the latitude range of carbonate reef growth. Once rapid carbonate sedimentation ceased as the seamount slipped below the depth of the photosynthetically supported growth, most of the constructional carbonate relief appears to have been unmodified by erosion (Greene et al., 1980). However, high-resolution reflection profiles gathered during Leg 197's presite survey for Site 1206 revealed bed forms typical of drift deposits. Evidently, bottom currents flowing over the submerged Koko Guyot have been active in redistributing particulate carbonate and volcaniclastic debris across its summit plateau. (Copies of the reflection records can be requested from the Ocean Drilling Program (ODP) Data Librarian; see the **"Related Leg Data"** contents list for contact information.)

DSDP Sites 308 and 309 (Larson, Moberly, et al., 1975) are located on the southeastern and southwestern edges of the summit region of Koko Seamount, respectively, in the gently sloping area mapped as terrace deposits (Greene et al., 1980). Sea conditions forced the termination of drilling at Site 308 after penetration to 68.5 meters below seafloor (mbsf) through lower Eocene calcareous volcaniclastic siltstone and sandstone. At Site 309 drilling terminated at 12 mbsf, owing to loss of a part of the bottom-hole assembly (BHA) in hard carbonate-cemented volcaniclastic sediment.

Site 1206 (34°55.55′N, 172°08.75′E) is located 6.2 km south-southwest of DSDP Site 308, in 1540 m water depth. Site 308 had been targeted during DSDP Leg 32 for a paleolatitude test of the motion of the Hawaiian hotspot, but drilling did not reach basement. We elected to return to Site 308 for a number of reasons. First, a clear basement sequence of reflectors was imaged on existing seismic reflection profiles that promised to provide the required shield-building lava flows ideal for paleomagnetic and petrochemical objectives. We planned a short presite survey around Site 308 (see **"Underway Geophysics,"** p. 24) to examine basement structure near the proposed drill site. Second, the composition of dredged rocks (alkalic basalt, trachyte, and nepheline phonolite) that have been radiometrically dated (whole-rock ^{40}Ar-^{39}Ar) (Clague and Dalrymple, 1973) is most consistent with eruption during a postshield phase of volcano construction. Hence, the measured age, 48.1 ± 0.8 Ma, is likely to underestimate the age of the main sequence of shield-forming lava flows by an unknown amount (see Fig. **F1,** p. 26, in the "Leg 197 Summary" chapter). Deeper drilling in the vicinity of Site 308, we predicted, would penetrate erosional surfaces and sample the older, main sequence of shield-building lava flows.

OPERATIONS

Transit to Proposed Site HE-6A (DSDP Site 308) and Underway Survey over Koko Seamount

The position of Site 1206 is nearly 400 nmi south-southeast of Site 1205 on Nintoku Seamount. Site 1206 is located on the southeastern sector of the lower summit platform of Koko Seamount. The site area was last visited during DSDP Leg 32, in mid-September 1973, when drilling took place at Site 308.

The 377-nmi transit to the first survey waypoint was accomplished at an average speed of 11.6 kt. During the 32.5-hr voyage, the skies were mostly cloudy with good visibility. Seas were flat with a gentle 4-ft swell from the east-northeast. Sea temperature continued to rise from 15° to 24°C during the 1.5-day voyage.

Prior to spudding Hole 1206A and consonant with the routine established during Leg 197, a geophysical survey was conducted to augment the paucity of seismic reflection data available for the site area, to locate a suitable site, and to acoustically characterize its structural and stratigraphic setting. Crossing high-resolution seismic reflection profiles were obtained using a single 80-in³ water gun firing every 4 s. At 1430 hr on 13 August 2001, the vessel slowed to 6 kt to deploy the seismic equipment, and by 2115 hr the survey was completed. The 33-nmi survey was completed at an average speed of 5.5 kt.

Our arrival over Koko Seamount was greeted by Russian fishing trawlers whose crews were tending nets and long lines. We also encountered a small container vessel traveling a great-circle route. The thrusters were lowered as the vessel, using the Global Positioning System (GPS), established the location for Site 1206 selected during the survey. Site 1206 is positioned ~6.2 km south of Site 308 (proposed Site HE-6A identified in the Leg 197 Scientific Prospectus). After the vessel was on station at 2116 hr, the hydrophones were lowered concurrent with making up a new BHA. A beacon was deployed at 2300 hr.

Hole 1206A

The corrected precision depth recorder (PDR) depth referenced to the dual elevator stool (DES) was obtained and indicated a water depth of 1544.1 m. The BHA was made up of a 9.875-in rotary core barrel (RCB) hard formation C-7 bit, a mechanical bit release, a modified head sub, an outer core barrel, a modified top sub, a modified head sub, seven 8.25-in drill collars, a tapered drill collar, six 5.25-in drill pipe sections, and one crossover sub.

Hole 1206A was spudded at 0215 hr on 14 August with the RCB and a wash barrel in place. The bit tagged the seafloor depth at 1557.0 m relative to the DES. The bit was drilled ahead to 57 mbsf, when the penetration slowed, suggesting basement contact. The wash barrel contained a composite of sedimentary material, most of which was a dark, calcareous, sandy siltstone and silty sandstone. Volcanic basement coring began with Core 197-1206A-2R (57.0–58.5 mbsf) (Table **T1**) and proceeded to a depth of 79.8 mbsf, when operations were suspended to conduct a short wiper trip to 35.0 mbsf in order to reduce high erratic torque.

Coring resumed and continued slowly, as frequent deplugger operations were required to free debris jamming the throat of the bit and the

T1. Coring summary, Site 1206, p. 96.

float valve. The recovery dropped off markedly below 104.4 mbsf (47 m into basement). After the hole was deepened an additional 23.8 m (128.2 mbsf) with only 0.45 m obtained (recovery = 1.9%), it was clear that a round trip of the drill string was required to determine and solve the reason for poor core recovery.

A free-fall funnel (FFF) was deployed at 0010 hr on 16 August. The bit cleared the top of the FFF at 0110 hr and was monitored via the vibration-isolated subsea television camera. The FFF was erect following the withdrawal of the bit. After the drill string was recovered, the bit and the area directly under the float valve in the mechanical bit release were found to be full of basalt fragments. Many of the fragments were obviously cored segments that apparently fell out of the core barrel during earlier operations. The reclaimed cored material added an additional 2.0 m to the 0.02-m recovery of the last core barrel (Core 197-1206A-14R). The bit was otherwise in excellent shape, but because it had accumulated 24 rotating hours in drilling 57 m of sediment and cored an additional 71.2 m of basement, it was retired from service. The average recovery for the cored interval of 71.2 m was 39.9%, corresponding to 28.39 m of cored material. The average rate of penetration (ROP) in basement coring was 3.3 m/hr.

Second Reentry (Third of Leg 197)

A new C-7 bit and a fresh mechanical bit release were made up to the BHA, and by 1015 hr on 16 August the bit was suspended above the open hole of Hole 1206A. Sometime in the interval between the extraction of the old bit and reentry positioning, the FFF had tipped over; apparently the 2.5-m length of 13.375-in casing failed to sufficiently penetrate the hard surface of the seafloor. However, the dynamic positioning operator adroitly maneuvered the vessel and at 1021 hr, the bare hole was successfully reentered.

Basement coring resumed in Hole 1206A, and by the evening of 19 August proceeded without incident from 128.2 to 323.2 mbsf. The hole was flushed with mud, and a wiper trip was made to 65 mbsf to prepare the hole for logging. The drill string stuck at two positions in the borehole, 101 and 171 mbsf. The driller had to apply 100,000 lb of overpull to free the pipe at 171 mbsf. The hole was washed and reamed from 65 to 323 mbsf, after which 2 m of fill were found at the bottom of the hole. After considering the unstable nature at the top of the hole and factoring in the 11-ft heave of the vessel, the prospects for a successful logging endeavor appeared dim. We decided to extend coring for the few remaining hours until time expired on site. Coring resumed and deepened the hole to 335.2 mbsf, when it was decided to terminate operations and recover the drill string.

An additional 207.0 m of basaltic basement was cored with the second bit (average recovery = 54.6%). The ROP varied from 1.2 m/hr (Core 197-1206A-23R [191.0–192.7 mbsf]) to 5.8 m/hr (Core 197-1206A-20R [162.2 to 171.8 mbsf]). The average ROP in basement with the second bit was 3.2 m/hr. The total cored interval in Hole 1206A was 278.2 m (average recovery = 50.8%) (Table T1). The average ROP for the two bits was 3.2 m/hr.

The drill string was recovered, and the BHA was inspected before being disassembled. The hydrophones and thrusters were retracted, the beacon was recovered, and all drilling equipment was secured by 2230 hr on 20 August, when the vessel left location for Yokohama.

LITHOSTRATIGRAPHY

Coring at Site 1206 began in volcanic basement rock beneath a thin, 57-m-thick sedimentary sequence. Only an RCB wash core (Core 197-1206A-1W) of firm sedimentary debris was recovered from the sedimentary section. This core consisted of two sections (197-1206A-1W-1 and 1W-2), containing a mixture of Quaternary- to Eocene-age material (see "Biostratigraphy," p. 5) that entered the core barrel during the wash down. Only black carbonate-rich lapilli breccia and a few centimeters of dark gray to black fine-grained sediment were recovered. Below 57 mbsf, red sedimentary interbeds and thick, red-brown weathered flow tops were recovered in the basement section of lava flows and volcaniclastic units (Cores 197-1206A-2R to 45R [57.0–335.2 mbsf]). These sedimentary units are described elsewhere (i.e., "Site 1206 Visual Core Descriptions," p. 1; Table T2).

T2. Sedimentary intercalations in basement basalt, p. 97.

Section 197-1206A-1W-1 contained pieces of very disturbed, mottled brown (4/3 10YR) clayey silt with angular to subangular gravel dispersed within them. The remainder is silt-sized, nonvesicular volcanic fragments. Section 197-1206A-1W-2 consists entirely of disturbed fine- to coarse-grained scoriaceous volcaniclastic breccia with rare ~1-mm-sized bioclasts throughout. The core catcher contained early Eocene (Zone NP14 or NP15) nannofossil-bearing siltstone (see "Biostratigraphy," p. 5).

BIOSTRATIGRAPHY

Calcareous Nannofossils

Hole 1206A

Hole 1206A was drilled in a water depth of 1544 m using a rotary core bit. The only nannofossil-bearing sediment obtained above basement from this hole was Sample 197-1206A-1W-CC. We recorded the abundance and distribution of nannofossils in this sample in the paleontology (PAL) database. Nannofossil preservation is poor to moderate. Sample 197-1206A-1W-CC is in nannofossil Zones NP14 (early to middle Eocene) or NP15 (middle Eocene). Nannofossils present are *Blackites creber, Blackites gladius* s.l., *Braarudosphaera bigelowii, Campylosphaera dela, Chiasmolithus grandis, Chiasmolithus* cf. *Chiasmolithus solitus, Coccolithus pelagicus, Coronocyclus nitescens, Discoaster barbadiensis, Micrantholithus entaster, Micrantholithus flos, Rhabdosphaera pinguis, Sphenolithus moriformis, Sphenolithus spiniger, Toweius gammation,* and *Zygrhablithus bijugatus*. *B. gladius* s.s. has been reported only from Zone NP15. Transitional forms (*B. gladius* s.l.) with slightly less stem swelling have been found in Zone NP14 (Siesser, 1983), associated with *B. creber,* the probable ancestor of *B. gladius*. The specimens in Sample 197-1206A-1W-CC resemble *B. gladius* more than *B. creber,* and we assign them to *B. gladius* s.l.

The Braarudosphaeracea present in this sample suggest a nearshore environment, as described previously for Hole 1205A.

Volcaniclastic Sediment

A number of volcaniclastic sandstone and other volcaniclastic sediment layers were cored in this hole. Most of the volcaniclastic beds are

barren of nannofossils. Samples 197-1206A-27R-1, 99–100 cm; 27R-1, 107–108 cm; 27R-1, 113–114 cm; and 28R-2, 33–34 cm, contain trace amounts of very poorly preserved nannofossils. *Campylosphaera* cf. *Campylosphaera dela, Chiasmolithus* sp., *Coccolithus pelagicus, Sphenolithus* spp., and *Toweius* spp. are present. The age is indeterminate.

Discussion

Hole 308 was drilled on Koko Seamount during DSDP Leg 32. Quaternary nannofossils were found in the upper half of Core 1 in Hole 308, overlying sediment assigned to the early Eocene *Discoaster lodoensis* Zone (Shipboard Scientific Party, 1975). Basement was not reached. The *D. lodoensis* zonal assignment was based on the presence of *D. lodoensis* and *Lophodolithus nascens* in the absence of *Tribrachiatus orthostylus* and *Discoaster sublodoensis* (Shipboard Scientific Party, 1975; Bukry, 1975). *L. nascens* is now known to range from Zone NP9 to lower Zone NP15 and *D. lodoensis* from Zone NP12 to the middle of Zone NP14 (Perch-Nielsen, 1985). These two species thus do not restrict assignment to the *D. lodoensis* Zone (= NP13). The presence of *B. gladius* s.l. in Hole 1206A indicates assignment to Zones NP14 or NP15. The estimated age range of the NP14–NP15 zonal interval is 43.5–49.7 Ma.

Braarudosphaera and *Micrantholithus* were also found in Hole 308, as they were in Hole 1206A. Based on these taxa and other fossils, the DSDP Leg 32 Shipboard Scientific Party (1975) inferred shallow-water deposition for the sediment.

PHYSICAL VOLCANOLOGY AND IGNEOUS PETROLOGY

We encountered basement at 57 mbsf at Site 1206 (Hole 1206A) on Koko Seamount and drilled 278 m into a sequence of lava flows, hyaloclastites, volcaniclastic sandstone, and limestone, of which 144 m (52%) was recovered. Although the basement of Koko Seamount has never been drilled prior to Leg 197, it was dredged during the *Thomas Washington* expedition Aries 7 (Davies et al., 1972; Clague and Dalrymple, 1973) and tholeiitic basalt, alkalic basalt, hawaiite, mugearite, trachyte, and phonolite were recovered.

A biostratigraphic age of early to middle Eocene (nannofossil Zones NP14 and NP15) was assigned to sediment immediately overlying basement at Site 1206, giving a minimum age of 43.5–49.5 Ma (see **"Biostratigraphy,"** p. 5), which is consistent with the 48.1-Ma K-Ar radiometric age for samples of dredged alkalic lava from Koko Seamount (Clague and Dalrymple, 1973). Basement rocks at Site 1206 consist of 15 lava flow units, 4 volcaniclastic sandstone horizons, and 3 thin limestone interbeds. The basaltic eruptive units often include hyaloclastite breccia or multiple lava flow lobes alternating with hyaloclastite. The basalt is mainly tholeiitic, although two samples are alkalic in composition.

Macroscopic Description

This section describes the different lithologies of the basement sequence in Hole 1206A. Detailed descriptions of each core section can be found in **"Site 1206 Core Descriptions,"** p. 1.

The basement in Hole 1206A was divided into 22 lithologic units (Tables T2, T3; Fig. F2) based on major changes in lithology such as the occurrence of weathered flow tops, sedimentary interbeds, or basal flow breccia, or abrupt changes in vesicularity. The basement rocks are mainly lava flows (Units 1, 2b, 4, 5, 6, 7, 10, 13, 17, 18, and 21 and parts of 8, 11, and 14) with associated hyaloclastite breccia beds (Subunits 2a and 2c and Unit 19 and parts of Units 8, 11, and 14) and a few interbeds of limestone (Units 3, 9, and 15) or sandstone (Units 12, 16, 20, and 22). The lava flows are dominantly olivine-phyric to aphyric basalt, although a few units also contain up to 3 modal% plagioclase phenocrysts. Olivine phenocrysts usually make up <5 modal% of the porphyritic basalt, except in Unit 17, and of olivine accumulation layers in Units 1, 4, and 6, which contain up to 25 modal% olivine phenocrysts. Plagioclase and olivine and, occasionally, clinopyroxene may be present together as glomerocrysts. Groundmass minerals include plagioclase, clinopyroxene, black oxides, minor glass, and, rarely, olivine.

Some lava flows are lobed, but most others consist of a single lobe (i.e., cooling unit) that includes a vesicular flow top, a massive interior, and a vesicular flow base often featuring pipe vesicles. Many of the flows are highly vesicular (up to 60%), with 1- to 10-mm-diameter vesicles, especially close to unit boundaries. Vesicles are sometimes filled with secondary minerals, including clay, carbonate, and zeolite. The basalt is moderately to highly altered near the top of the section, but only slightly to moderately altered deeper in the section (see **"Alteration and Weathering," p. 15**). Olivine phenocrysts are the first phase to show signs of alteration and are often completely replaced by serpentine, iddingsite, celadonite, or talc. However, in several units, much of the olivine remains unaltered. Unaltered glass persists in some of the lobe margins and hyaloclastite units.

The hyaloclastite beds are most commonly present at the base of lava flow units, except for Unit 2, where it also caps the lava, but hyaloclastite layers are also interbedded with lobes of aphyric basalt in Units 8, 11, and 14. They are clast-supported hyaloclastite lapilli breccia consisting of angular glass and basalt lapilli to breccia fragments in a matrix of fine lapilli. Large basalt clasts are also present, and in some cores it is difficult to determine whether these are large clasts or discrete flow lobes in the breccia sequence.

Some thin intercalations of sediment (limestone, volcaniclastic sandstone, and grainstone and a red-brown deeply weathered flow top) are also present. These are summarized in Table T2. Detailed descriptions of these intervals are given in **"Site 1206 Core Descriptions," p. 1**, but some general comments can be made. In the upper part of the basement sequence (Cores 197-1206A-2R to 27R) the sediment interbeds consist of layers of matrix-supported calcilutite, calcarenite, and limestone with bioclasts and miliolid foraminifers. In the lower part of the basement section, rather thicker layers are grain-supported calcareous grainstone, volcaniclastic grainstone, sandstone, and conglomerate. Bioclasts include cylindrical particles, miliolid foraminifers, and millimeter-sized fragments of coral, sponge spicules, and bivalves. Moderate bioturbation is limited to vertical burrows at infrequent intervals. The size range, sorting, and biogenic components of these sediment interbeds suggest deposition in a nearshore environment.

T3. Basement units, p. 99.

F2. Recovery, thickness, composition, and lithology of basement units, p. 29.

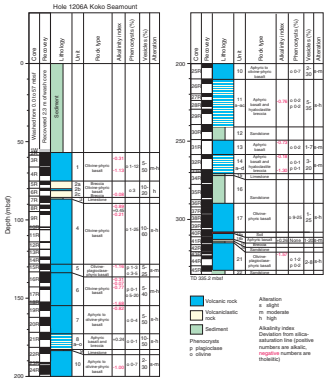

Physical Volcanology

Volcanic Succession

The basement drilled at Site 1206 is composed of a 278-m-thick succession of 22 lithologic units (Fig. F2; Table T3). We have identified 15 units as lava flow formations, and 7 units are sedimentary in origin.

The sedimentary units consist of fossiliferous vitric-lithic sandstone and gravelstone along with minor limestone intervals and exhibit textures, structures, and fossil assemblages indicative of deposition in a wave-dominated nearshore environment (see "Site 1206 Core Descriptions," p. 1; Table T2).

The volcanic rocks make up ~88% of the basement section recovered at Site 1206 (Table T3). They are broadly similar in composition to the magmas erupted during the shield stage of Hawaiian volcanoes (see "Geochemistry," p. 13). We divided the volcanic succession into 15 lava flow units (as defined in Table T3, p. 79, in the "Explanatory Notes" chapter) and 10 eruption units (see Tables T3, T4). However, subsequent paleomagnetic and geochemical measurements have raised some concerns about the validity of this division in intervals of poor recovery (i.e., Unit 4: Cores 197-1206A-8R to 14R and Unit 6: Cores 17R to 19R) (Table T5). These uncertainties are addressed in detail below.

T4. Structure and morphology of basement units, p. 101.

T5. List of cores and recovery, p. 102.

The top part of Unit 4 (i.e., Sections 197-1206A-7R-2 to 7R-4) consists of four 0.1- to 1.1-m-thick pahoehoe lobes containing olivine phenocrysts (5–7 modal%) and plagioclase microphenocrysts (2–3 modal%). Sections 197-1206A-8R-1 and 8R-2 of this unit contain broken core consisting of highly and sparsely vesicular lava fragments. No distinct flow lobe structures are discernible. Furthermore, in Section 197-1206A-8R-1, Pieces 21, 22, 24, 25, and 27 consist of fractured lava with detrital carbonate filling the cracks, whereas Pieces 23, 26, 29, and 30 consist of laminated to massive calcareous lithic-vitric sandstone. The lava in Sections 197-1206A-7R-2 to 8R-1 contains olivine phenocrysts (≤1 mm) along with plagioclase microphenocrysts. Plagioclase microphenocrysts are not present in the lava from Section 197-1206A-8R-2 (below Piece 9) and in subsequent cores in Unit 4. However, this change in plagioclase microphenocryst content of the lava does not coincide with the presence of detrital carbonate as fracture fill. It is present across an inferred lobe boundary placed at 36 cm in Section 197-1206A-8R-2 on the basis of changes in vesicle fabric and lava crystallinity.

Because of drilling problems (i.e., a clogged bit) the recovery in Cores 197-1206A-9R through 13R was exceptionally low (recovery = 0.43%–22%) (Table T5). The lava in Core 197-1206A-14R represents the material recovered from the clogged drill bit, and therefore its stratigraphic significance is ambiguous. Consequently, the internal architecture of the lava in Cores 197-1206A-9R through 14R is unknown, although the vesicularity and vesicle fabric of the lava in these cores is consistent with a pahoehoe flow origin. The olivine phenocryst size (3–5 mm) and abundance (7–25 modal%) of the lava in Cores 197-1206A-9R to 14R is significantly greater than those found in the upper part of Unit 4 (Cores 197-1206A-7R to 8R). Thus, it is possible that this unit is made up of lava from more than one eruption, and this uncertainty will be addressed by shore-based studies.

Unit 6 consists of multiple 0.2- to 2.0-m-thick pahoehoe lobes, characterized by smooth glassy lobe margins, and the overall architecture of the unit is consistent with that of a compound pahoehoe flow (Table T4). A significant change in size and abundance of olivine phenocrysts

occurs across Cores 197-1206A-17R to 18R: from <1 mm and 5–8 modal%, respectively, in Cores 16R to 17R to 4–5 mm and 10–20 modal%, respectively, in Core 18R to Section 19R-1 (see **"Site 1206 Core Descriptions,"** p. 1). This change is coupled with significant deficiencies in recovery (Table **T5**) and changes in magnetic inclination (see **"Paleomagnetism and Rock Magnetism,"** p. 18). This latter evidence suggests that this lava unit may consist of two separate eruption units (i.e., flow fields).

Of the 15 lava flow units, 11 (66%) are composed of subaerial basaltic lavas and 4 are composed of basalt hyaloclastite breccia with lava lobe intervals (34%) (Tables **T3, T4, T6**). Evidence for subaerial emplacement of the Site 1206 lava flow units is derived from their highly vesicular nature, along with the dominance of pahoehoe and a'a flow morphologies (Table **T4**) (Cas and Wright, 1987; Self et al., 1998). We interpret the hyaloclastite breccia units to be flow-foot breccia (also known as lava deltas) to the overlying lava flows. Flow-foot breccia is formed when lavas flow from land into water (Jones and Nelson, 1970; Moore et al., 1973). The breccia is produced by quenched fragmentation upon contact with water in the nearshore environment, whereas pillowlike lobes are formed where the lava is expelled from tube entries situated below the water level.

T6. Statistics on flow types, p. 103.

We next grouped the lava flow units into 10 "eruption units" (= flow fields) (see Table **T3,** p. 79, in the "Explanatory Notes" chapter) by identifying several sets of lava flows that formed by the same eruptions (labeled I–X; Table **T4**). In general terms, this division follows the consolidation of the volcanic section into eruption units in which the flow-foot breccias are grouped with the overlying lava units (e.g., Units 1–2, 7–8, 10–11, and 13–14) (Tables **T3, T4**). The basis for this pairing of the basement units is that the hyaloclastite breccia and the overlying lava flows are consistently present as a characteristic lithofacies association situated above the main sedimentary horizons in the section. Also, the paired basement units that form each eruption unit have similar petrographic characteristics. Moreover, analyzed samples from eruption Units I, II, and IV have similar Ti/Zr ratios (see **"Geochemistry,"** p. 13) (Fig. **F3**). However, analyzed samples from Units 7 and 8, which tentatively are grouped together as eruption Unit V, differ significantly in chemical composition. Only one onboard sample was taken from each unit for thin section and chemical analysis, and the Unit 7 sample was taken from Section 197-1206A-19R-3 near the top of the unit. Therefore, at this stage it is not certain if basement Units 7 and 8 represent one or more eruption units.

F3. Ti/Zr ratio vs. depth in basement, p. 30.

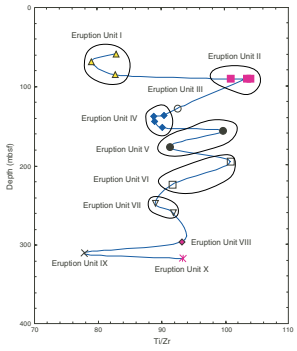

Below, we describe the characteristic architecture of the lava flow units at Site 1206 and briefly discuss the volcanologic implications of the observed lithofacies associations. The terminology used in this section to describe the lavas is outlined in **"Physical Volcanology and Igneous Petrology,"** p. 10, in the "Explanatory Notes" chapter.

Lava Flow Units

Using the type of flow or lobe contacts along with arrangement of internal flow structures, we identified three lava flow types and one subtype in the Site 1206 basement succession (Table **T4**). The Site 1206 lavas are categorized as compound pahoehoe (five units), flow-foot breccia (four units), a'a (four units), and transitional (one unit). Because of poor recovery, the flow type of Unit 13 (Section 197-1206A-31R-1) could not be determined with certainty, but the vesicle fabric of the

lava appears to be consistent with a pahoehoe flow origin. The key features of the lava flow units are listed in Table T4, and the main characteristics of each lava type are summarized below.

Compound Pahoehoe (Units 1, 4, 6, 7, 10, and, Possibly, 13)

At Site 1206 the compound pahoehoe lavas account for 47% of the total thickness of the volcanic succession and are the thickest subaerial eruption units in the succession, varying from 16 to 39 m (Tables T4, T6). Each unit consists of 5 to >14 vertically stacked lobes ranging from 0.1 to 7.7 m in thickness.

The pahoehoe lobes are characterized by smooth glassy lobe margins grading sharply to aphanitic (hypohyaline to hypocystalline) groundmass, whereas the lobe interiors are typically fine grained and holocrystalline. The lobes have highly vesicular upper and lower crusts and moderately vesicular to nonvesicular lobe interiors (Table T4). Smaller lobes are typically vesicular throughout. The vesicle fabric is isotropic (i.e., shows no evidence of viscous deformation of the lava during flow) and is consistent with laminar flow of low viscosity lava beneath a stationary insulating crust. These lobes also feature segregation structures, such as small pipe vesicles, vesicle cylinders, and megavesicles, which are indicative of lava inflation during emplacement (Self et al., 1998).

Flow-Foot Breccia (Sheet Lobes; Subunits 2a–2c, 8a–8o, 11a–11ae, and 14a–14d)

These volcanic units consist of very poorly sorted and clast-supported hyaloclastite lapilli breccia intercalated with up to 15 coherent lava intervals. Each lava interval is composed of one to three lava lobes with smooth glassy margins, and the vesicularity of the lobes is variable, typically between 30% and 40% near the top of each breccia unit and decreasing steadily to <3% at the base. This change in vesicularity is consistent with transformation from pahoehoe to pillow morphologies (Self et al., 1998). The lapilli breccia units are always capped by a compound pahoehoe lava and invariably have a conformable depositional contact with the underlying sedimentary units (Table T4; Fig. F4).

The breccia consists of highly angular and sparsely to moderately vesicular (1%–20%) basalt glass fragments, 2–15 mm in size, which are altered to bright green to dark green clay. The basalt glass fragments are well preserved and are characterized by blocky shapes, with straight to highly irregular and convoluted outlines (Fig. F5). Present in the lapilli breccia are larger (20–70 mm) angular clasts of aphanitic lava that have the same lithology as the basalt glass clast population, except for a higher degree of crystallinity. Many of the lava clasts have unaltered glassy lobe margins along one or more of their edges, indicating that they were formed by disintegration of small lava lobes. The breccia has a matrix of black clay (after silt-sized fractions of glassy basalt fragments?). The matrix often contains green clay pseudomorphs of sand-sized basaltic glass shards that exhibit blocky and splinterlike morphologies.

The overall characteristics (or architecture) of the hyaloclastite lapilli breccia units, volcaniclastic texture, and lithofacies associations suggests that they were formed as flow-foot breccia when subaerial lava flowed from land into water.

F4. Internal architecture of an eruption unit, p. 31.

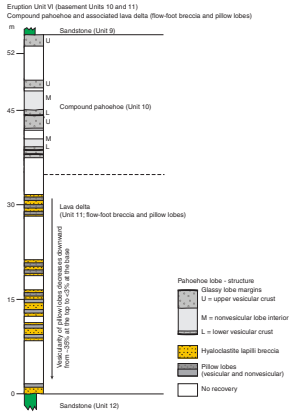

F5. Clast morphologies in hyaloclastite lapilli breccia, p. 32.

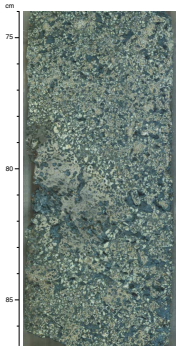

A'a Lavas (Units 5, 17, and 21)

Three lava units at Site 1206 were identified as a'a flows and account for ~17% of the total lava thickness in the succession (Table T4). The a'a lavas range in thickness from 7 to 17 m (average = 8.4 m). Units 5 and 21 consist of a single lobe (or cooling unit), whereas Unit 17 is composed of two lobes. These lavas are characterized by massive interiors enveloped by thin flow-top and flow-base breccias (0.1–2.3 m thick) consisting of spinose and clinkerlike lapilli-sized basalt clasts (Fig. F6). However, the flow-top breccia of Unit 5 was not recovered and the basal breccia of Unit 21 contains an ash-sized matrix of splinterlike and blocky fragments, indicating fragmentation by contact with water. Internally, these lavas are characterized by a central region with moderately developed viscous flow fabric that is enveloped by zones showing distinct viscous flow fabric (Fig. F6). This fabric is expressed by a subparallel arrangement of flow bands (present as 1- to 2-mm-thick dark gray and subhorizontal wispy bands) and by elongate vesicles drawn out in response to viscous flow at high strain rates. The observed flow fabric is best explained by a sheared laminar flow around a flow center that is transported within a viscous flow as a plug.

F6. Internal architecture and velocity profile of a'a lava, p. 33.

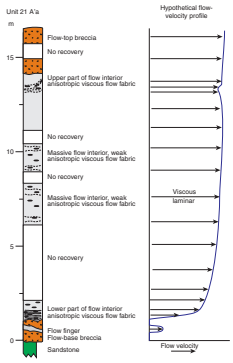

Transitional Lava (Unit 18)

Unit 18 is a 3.1-m-thick lava unit that has a pahoehoe base and is capped by a deeply weathered scoriaceous flow top. It features well-developed viscous flow fabric and is the only lava at Site 1206 identified as a transitional type (Table T4). This low frequency of transitional flow type occurrence at Site 1206 contrasts strongly with that of Site 1205 at Nintoku Seamount, where transitional lavas are the most common flow type (see **"Physical Volcanology and Igneous Petrology,"** p. 8, in the "Site 1205" chapter). The reason for this difference is not obvious but may indicate gentler slopes at Site 1206 compared to those of Site 1205.

Remarks

The pahoehoe lavas and their subaqueous derivatives make up >80% of the lava succession at Site 1206 and represent the low-viscosity end-member of the lava types in the section. These lavas exhibit internal flow architecture similar to that found in modern pahoehoe flow fields in Hawaii and at other Emperor Seamounts (e.g., Hon et al., 1994) (see also the "Physical Volcanology and Igneous Petrology" sections in each site chapter), implying that endogenous growth was an important mechanism for dispersing lava from the source vents at Koko Seamount. We envision that the lava was transported in insulating pathways from the source vents to the active flow fronts, which were nearshore entries similar to those depicted on Figures F7 and F8. As the lava broke out from its pathway, it advanced onward into the sea, where it was subjected to quench fragmentation, which contributed to the growth of the flow-foot breccia (see also Fig. F56, p. 83, in the "Leg 197 Summary" chapter).

The a'a lavas of Site 1206 represent flows that had the highest bulk viscosity when they were emplaced, which indicates thermally inefficient lava emplacement in open lava channels rather than higher initial melt viscosities (see **"Physical Volcanology and Igneous Petrology,"** p. 8, in the "Site 1205" chapter).

F7. Photograph of lava flowing into the sea, p. 34.

F8. Features of the lava emplacement environment, p. 35.

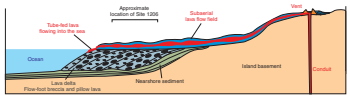

Petrography

Silicate Mineralogy

The lavas recovered from Site 1206 are all aphyric or olivine-phyric to olivine-plagioclase-clinopyroxene-phyric basalt. Olivine is the most abundant phenocryst phase (up to 10% of rocks examined in thin section). Olivine is observed in both the phenocryst (0.8–5 mm size) and microphenocryst (0.1–0.8 mm size) phases. Euhedral olivine phenocrysts are typically altered to brown clay, serpentine, or green clay, with iddingsite or Fe oxyhydroxide alteration concentrated along the rims or fractures (e.g., Figs. F9, F10, F11, F12). Rarely, they are replaced by calcite or zeolite. In some cases an unaltered interior remains (e.g., Figs. F13, F14, F15). Embayed margins and hollow centers (infrequently observed) are evidence for disequilibrium of the phenocryst phase with the groundmass. Often, Cr spinel inclusions (<0.1 mm in size) are observed in the olivine phenocrysts (e.g., Figs. F16, F17).

Plagioclase phenocrysts constitute up to 4 modal% of some rocks. These are present as subhedral laths that average ~0.7 mm in length. They often exhibit optical zonation, fractures, resorbed margins, and embayments, indicating resorption (e.g., Fig. F18). Frequently, plagioclase forms glomerocrysts with clinopyroxene and, rarely, olivine (e.g., Figs. F19, F20, F21).

Where present, clinopyroxene phenocrysts account for up to 3 modal% of some rocks. These are subhedral and 0.5–2 mm in size. They commonly are incorporated in glomerocrysts with plagioclase. Rare Cr spinel phenocrysts (average size = 0.4 mm) are present in samples from Units 6 and 17 (e.g., Fig. F22).

Many basalt samples exhibit a porphyritic texture, composed of larger phenocrysts in a fine-grained to aphanitic groundmass of plagioclase, clinopyroxene, glass, titanomagnetite, and, occasionally, olivine. Sometimes the groundmass is characterized by a subophitic texture, but most commonly it has an intergranular to intersertal texture.

In the groundmass, plagioclase laths are euhedral to subhedral, averaging ~0.3 mm in length, and are sericitized and/or altered to clay in some samples. In Subunit 2c, groundmass plagioclase laths exhibit swallow-tail terminations, indicative of high cooling rates and rapid growth. These can be found sericitized and altered to clay in some samples. Groundmass clinopyroxene is usually anhedral. Titanomagnetite is a minor constituent of the groundmass, exhibiting small, often octahedral, and sometimes dendritic morphologies (<0.5 mm in size) that are sometimes partially altered to maghemite (e.g., Fig. F23; see also below). Groundmass olivine is rare, but when present it is completely altered to iddingsite or green clay. In some instances (such as Section 197-1206A-19R-3), groundmass olivine may actually be a microphenocryst phase (e.g., Fig. F24). In other areas, olivine displays a seriate texture. Glass is usually devitrified and completely altered to brown clay, green clay, or zeolite. Vesicles are variable in abundance (up to 20%). Some are surrounded by segregated material, often composed of plumose altered clinopyroxene and titanomagnetite crystals that radiate out from skeletal plagioclase (e.g., Fig. F25).

Basalt recovered from Site 1206 differs from that recovered from Site 1205 in the lower abundance of groundmass olivine. The overall texture of the groundmass also differs, from subtrachytic in basalt from Site 1205 to generally intersertal to subophitic in that from Site 1206. In contrast to basalt from Sites 1203 and 1205, where plagioclase is the

F9. Euhedral olivine altered to iddingsite, p. 36.

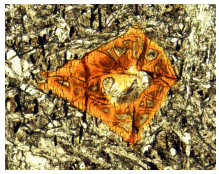

F10. Olivine partially altered to talc, p. 37.

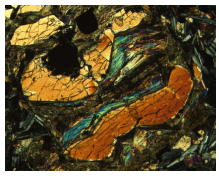

F11. Another view of olivine partially altered to talc, p. 38.

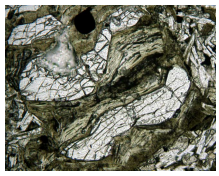

F12. Olivine altered to iddingsite, p. 39.

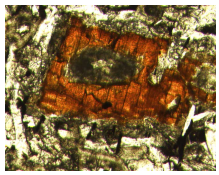

F13. Unaltered euhedral olivine in aphanitic groundmass, p. 40.

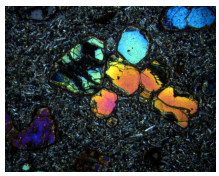

F14. Euhedral olivine: unaltered interior; rims altered to iddingsite and green clay, p. 41.

dominant phenocryst phase, basalt from Site 1206 is dominantly olivine-phyric.

Opaque Mineralogy

The opaque mineralogy of the Site 1206 basalt units is dominated by titanomagnetite. Primary sulfide is notably absent from every thin section examined from this site. Secondary pyrite was observed in only two instances (Units 7 and 21) (see Table T7). In general, titanomagnetite has a morphology that is predominantly a mixture of subhedral skeletal octahedra and dendritic forms (Fig. F26), but with a few units exhibiting only subhedral skeletal octahedral forms (e.g., Units 5 and 21) (Fig. F27). Titanomagnetite exhibits varying degrees of oxidation (see Table T7); ilmenite oxidation lamellae are present in the titanomagnetite throughout the basalt units (e.g., Fig. F28). The development of ilmenite oxidation lamellae is occasionally accompanied by alteration to maghemite along cleavage planes, fractures, and at the crystal margins (e.g., Figs. F28A, F29). In basalt units containing maghemite, it is common that many titanomagnetite crystals have escaped this alteration (e.g., Fig. F30). As we note in other site reports from Leg 197, maghemite and titanomaghemite (or Ti-bearing maghemite) are indistinguishable using reflected-light microscopy.

Cr spinel is also found in all lava flow units except Units 7, 8, 10, 18b, and 21. The Cr spinel is usually found as inclusions in olivine phenocrysts (e.g., Figs. F31, F32) and may exhibit titanomagnetite overgrowths (Fig. F33). Cr spinel is present in the olivine-rich regions of Units 6 and 17 as both inclusions in olivine and as discrete phenocrysts. In Unit 6, the Cr spinel phenocrysts are euhedral (Fig. F33) with a small titanomagnetite overgrowth (Fig. F34). The titanomagnetite overgrowths on Cr spinel contain ilmenite oxidation lamellae and maghemite development along fractures, but these features are truncated by the Cr spinel (Fig. F35). Olivine in Unit 6 is highlighted by a rim of Fe oxyhydroxide–rich iddingsite (Fig. F36A), a reddish brown substance consisting of smectite, chlorite, and goethite + hematite (e.g., Deer et al., 1992). In Unit 17, olivine is highlighted by a rim of serpentine and the Cr spinel phenocrysts are round (Fig. F36B). The morphology of the Cr spinel phenocrysts is due to extensive overgrowths of and complete replacement by titanomagnetite (Fig. F37). The titanomagnetite has subsequently been oxidized and exhibits ilmenite oxidation lamellae (Fig. F37C, F37D). A similar relationship between titanomagnetite and Cr spinel is seen in Unit 5 (Sample 197-1206A-15R-1 [Piece 7A, 72–74 cm]) and suggests discrete Cr spinel phenocrysts may also have been present in this unit but have subsequently been replaced by titanomagnetite (cf. Figs. F37A, F37B, F38). Cr spinel inclusions in olivine from Unit 6 are usually replaced by titanomagnetite, especially if they lie in the iddingsite alteration rim (Fig. F39).

Plagioclase and clinopyroxene in the glomerocrysts present in Unit 5 also contain Cr-rich opaque minerals (Fig. F40). These may be small chromite crystals, as they are dull gray in reflected light compared to titanomagnetite and lack the characteristic blue-gray color of Cr spinel.

Geochemistry

Major and trace element abundances were determined by inductively coupled plasma–atomic emission spectroscopy (ICP-AES) (see "Physical Volcanology and Igneous Petrology," p. 10, in the "Explanatory

F15. Another view of euhedral olivine: unaltered interior; rims altered to iddingsite and green clay, p. 42.

F16. Olivine phenocryst with Cr spinel inclusion, p. 43.

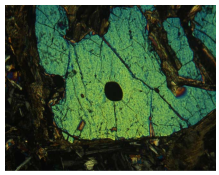

F17. Another view of an olivine phenocryst with Cr spinel inclusion, p. 44.

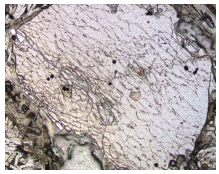

F18. Anhedral plagioclase showing strongly resorbed margins, p. 45.

F19. Plagioclase-clinopyroxene glomerocryst, p. 46.

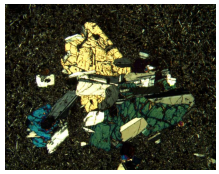

F20. Olivine-plagioclase-clinopyroxene glomerocryst, p. 47.

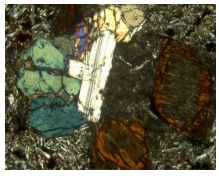

Notes" chapter) for 20 basaltic samples from the basement rocks at Site 1206 (Table T8). In the total alkalis vs. SiO_2 classification plot only three of the 20 samples are alkalic basalt (basalt from Units 8 and 18 and one of the three samples from Unit 4), whereas all other samples plot in the tholeiitic basalt field (Fig. F41). The alkalic nature of basalt from Units 8 and 18 is confirmed by their relatively high TiO_2 and Zr content at a given MgO content; however, the compositionally heterogeneous samples of Unit 4 do not have equally high TiO_2 and Zr contents (Fig. F42), so the lone sample from Unit 4 that plots in the alkalic field may have experienced K_2O addition during alteration. At 7 wt% MgO, Site 1206 samples range significantly in TiO_2 and Zr content; clearly, the lavas do not define a single liquid line of descent. Apparently, the lavas recovered at Site 1206 evolved from a continuum of parental magmas ranging from tholeiitic basalt with relatively high abundances of incompatible elements to slightly alkalic basalt with higher abundances of incompatible elements.

Basalt from Koko, Nintoku, and Suiko Seamounts define inverse trends in plots of Al_2O_3, TiO_2, Na_2O, K_2O, and Zr abundance vs. MgO content (Fig. F42). Samples from Koko and Suiko Seamounts overlap in MgO variation plots. In contrast, many of the alkalic lavas at Nintoku Seamount have lower MgO contents and they show trends to lower CaO and Sc contents (Figs. F42, F43), indicative of clinopyroxene fractionation. Such trends are typical of the alkalic lavas erupted during the postshield growth stage of Hawaiian volcanoes (see "Physical Volcanology and Igneous Petrology," p. 8, in the "Site 1205" chapter). Two of the three Site 1206 samples (one from Unit 4 and one from Unit 8) that plot in the alkalic field (Fig. F41) also have relatively low CaO contents, but they do not have low abundances of Sc (Fig. F42; Table T8).

Abundances of incompatible trace elements such as Ba, Sr, and Zr further demonstrate the geochemical similarity of basalt from Koko and Suiko Seamounts and the higher abundance of Ba and Sr in basalt from Nintoku Seamount (Fig. F44). The alkalic basalt from Koko Seamount does not have the high Sr and especially the high Ba content that characterizes the alkalic basalt from Nintoku Seamount (Fig. F44). In contrast to the differences in Sr and Ba, basalt from all three seamounts define the same Ti vs. Zr trend (Fig. F44).

An important aspect of the growth of most Hawaiian volcanoes is the gradual temporal trend from dominantly tholeiitic basalt during the shield stage followed by dominantly alkalic basalt during the postshield stage (Clague and Dalrymple, 1987). The dominance of alkalic lavas at Site 1205 on Nintoku Seamount (Fig. F45) clearly shows that the basement represents the postshield stage, whereas at Suiko Seamount only the uppermost three lava units are clearly alkalic basalt (Jackson et al., 1980). Like lavas from Hole 433C at Suiko Seamount, basalt from Site 1206 at Koko Seamount is dominantly tholeiitic (Fig. F45). We infer that at Site 1206 the late shield–stage of growth at Koko Seamount was sampled, but lavas that likely represent the postshield and rejuvenated stages have been recovered by dredging (Clague and Dalrymple, 1973, 1987).

As discussed in "Physical Volcanology," p. 8, the 22 lithologic units (Fig. F2) can be grouped into 10 eruption units and 7 intercalated sediment units (Table T3). Multiple samples were analyzed from eruption Units I, II, and IV, but recovery was low in the intervals represented by these units, especially from Cores 197-1206A-4R to 6R, 9R to 15R, and 16R to 17R (Fig. F2). Our goal was to geochemically evaluate the inter-

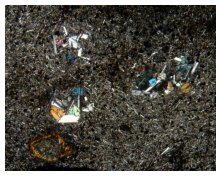

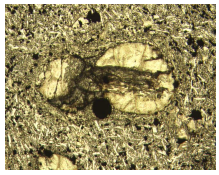

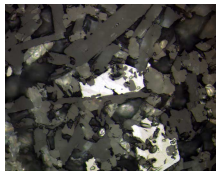

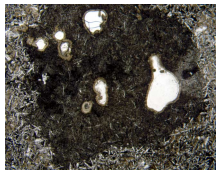

pretation that these intervals might contain more than one eruption unit. Abundances of Ti and Zr are relatively immobile during postmagmatic alteration; hence, the Ti/Zr abundance ratio can be used to evaluate the grouping of lithologic units into eruption units. The Ti/Zr ratio clearly distinguishes eruption Units I, II, and IV (Fig. F3). However, samples analyzed from eruption Units V and VI have disparate Ti/Zr ratios (Fig. F3). In particular, eruption Unit V contains one of the two distinctly alkaline samples. In this case, the geochemical data are inconsistent with the grouping of lithologic Units 7 and 8 into a single eruption Unit V.

Lavas in eruption Units I, II, and IV contain variable amounts of olivine (Fig. F2), and undoubtedly the variable MgO content of samples from eruption Units I and IV reflects varying amounts of olivine in the analyzed samples (Fig. F46). The compositional variation of eruption Units I and IV in Figure F46 could be explained by addition and subtraction of Fo_{70} olivine. It is likely, however, that olivine in these lavas has a higher forsterite content; approximately Fo_{82} is inferred using the whole-rock (wr) Fe/Mg ratio (assuming 90% of Fe is Fe^{2+} and $(Fe/Mg)_{ol}/(Fe/Mg)_{wr} = 0.3$). A more realistic explanation of the trend in Figure F46 may be combined fractionation of olivine and plagioclase. Plagioclase is a minor phenocryst phase in these eruption units.

Although the three samples from eruption Unit II have similar Ti/Zr ratios and abundances of Ti, Zr, and MgO (Figs. F3, F46), each sample has distinctive geochemical features. Among these three samples, Sample 197-1206A-8R-1, 99–101 cm, has the highest Al_2O_3 content (16.1 vs. ~15 wt%), whereas Sample 197-1206A-8R-1, 2–3 cm, has the lowest K_2O content (0.55 vs. 0.8–0.9 wt%) and Sample 197-1206A-8R-2, 3–5 cm, has much lower abundances of CaO, Na_2O, Sr, and Ba (Table T8). These differences may indicate that this eruption unit was formed by more than one geochemically distinct magma or possibly that these compositional differences reflect the effects of postmagmatic alteration.

ALTERATION AND WEATHERING

Twenty-two units and additional associated subunits have been identified in the basement section recovered from Hole 1206A. The entire sequence is characterized by alternating basaltic flow units, volcaniclastic sediment units, and biogenic-lithic sediment units (see "Physical Volcanology and Igneous Petrology," p. 6).

All lava flows and volcaniclastic sediment have undergone secondary alteration. Alteration mineralogy and vesicle and vein fillings were defined in rocks from Site 1206 by color, habit, and hardness in hand specimen, by optical properties in thin section, and by analogy with well-studied minerals identified during previous legs. Some X-ray diffraction (XRD) analyses were conducted to confirm identification of secondary minerals. Because of instrumental problems encountered on board, these data should, however, be used with caution and only as a general guide for mineral identification.

The effects of alteration in rocks from Site 1206 are identified in the lava flow units in terms of (1) alteration assemblages and vein and vesicle filling and (2) alteration chemistry.

F26. Skeletal octahedral and dendritic titanomagnetite morphologies, p. 53.

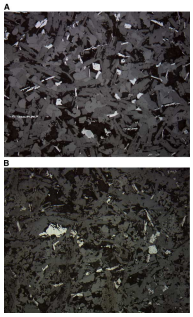

F27. Skeletal octahedral titanomagnetite morphologies, p. 54.

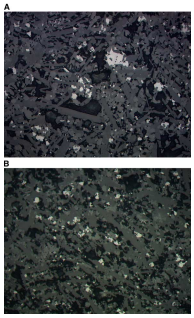

F28. Ilmenite oxidation lamellae in titanomagnetite, p. 55.

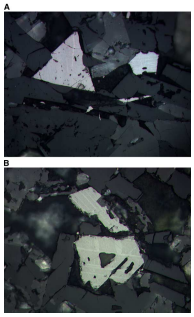

F29. Maghemite development along cleavage planes and fractures, p. 56.

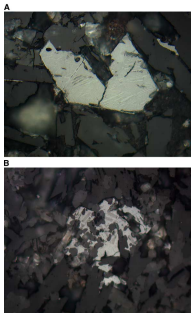

Alteration Assemblages and Vein and Vesicle Fillings

All lava flows recovered are slightly to highly altered basalt (Fig. F47). Overall, the degree of alteration is slight to moderate in the Hole 1206A basement sequence, although some units show higher degrees of alteration (e.g., Unit 1, parts of Unit 6, and the top of Unit 17). The alteration degree is fairly constant downhole.

The core sample color is the first indication of the alteration conditions. Cores fall mainly within the range of dark gray (N3) to medium-light gray (N6), which are characteristic of unaltered basalt. In more altered intervals, colors are variable between light brownish gray (5YR 6/1), grayish green (10GY 5/2), grayish red (5R 4/2), moderate yellowish brown (10YR 5/4), or grayish brown (5YR 3/2). No clear zonation was observed in the cores of Hole 1206A that could be related to different redox conditions in the sequence.

In the following sections, the alteration assemblages and vesicle and vein fillings are described. For a summary of downhole alteration assemblages and vesicle fillings, see Figure F47. Alteration assemblage and vein information were also recorded in the alteration and vein logs (see "Site 1206 Alteration Logs," p. 204, and "Site 1206 Vein Logs," p. 206). The alteration assemblages and vein and vesicle fillings show only slight variations downhole.

The alteration assemblages are dominated by Fe oxyhydroxide, clay, and zeolite. Green clay such as smectite (saponite and nontronite) and blue-green clay such as celadonite are the main phases. Some brown clay is also present as well as white–pale green expanding smectite. The latter was recognized by XRD as aliettite (alternating talc- and saponite-layered smectite). Zeolite is present in almost all of the sequence. The main zeolite mineral was identified by XRD as phillipsite. Some carbonate (calcite) is present in the most altered part of the sequence (e.g., Units 1, 6, and 17).

Vesicularity is high in some intervals of the Hole 1206A sequence (see also "Physical Volcanology and Igneous Petrology," p. 6). Vesicles are variably unfilled, lined, or filled by secondary minerals. Figures F48 and F49 show examples of vesicles filled with brown clay, saponite (pale green), and celadonite (blue green). As for alteration assemblages, the dominant minerals are clay (brown clay, aliettite, saponite/nontronite, and celadonite), Fe oxyhydroxide, and zeolite. Zeolite is often present as small well-shaped crystals. Carbonates (mainly calcite) are also present in most of the sequence (Fig. F47).

The sequence in Hole 1206A is sparsely veined. Veins are usually very thin (~0.5 mm wide) and do not present a preferred orientation. Veins are mostly filled with carbonate associated with variable proportions of green clay (saponite/nontronite) and blue-green clay (celadonite). Zeolite is also present in the veins but in lesser amounts than in the vesicles (Fig. F47).

Alteration Chemistry

ICP-AES analyses performed on board are used in this section to evaluate the effects of alteration on whole-rock chemistry. It should be noted, however, that only the freshest samples were analyzed, and the data reported here might not be representative of the overall alteration effects. Variations in the abundance (K_2O) and ratios (Cu/Zr, Co/Zr, and Zn/Zr) of some chemical elements and loss on ignition (LOI) vs. depth are reported in Figure F50. LOI is generally low in the whole sequence,

F30. Maghemite development around groundmass titanomagnetite, p. 57.

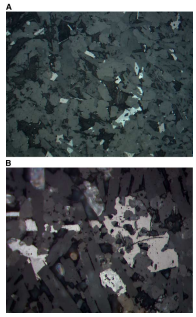

F31. Cr spinel inclusions in unaltered olivine phenocrysts, p. 58.

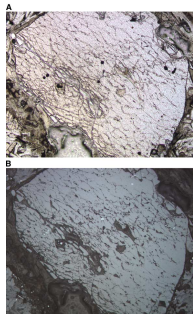

F32. Cr spinel inclusions in altered olivine phenocrysts compared to groundmass titanomagnetite, p. 59.

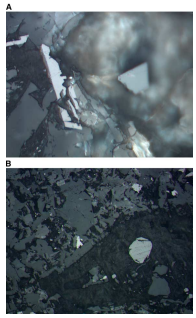

F33. Cr spinel inclusions in a partially altered olivine phenocryst, p. 60.

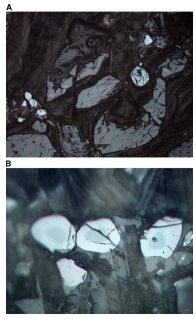

varying from –0.32 to ~3 wt%. Six samples have LOI >3 wt% (Fig. F50) and are in Units 4, 6, 7, 11, and 17. These higher values confirm hand specimen observations. K_2O abundances are low in the Site 1206 sequence, with values ~0.5 wt%. Three samples display slightly higher K_2O content in Units 4 and 18 (Fig. F50). As these units are composed of alkali basalt, we believe that the higher K_2O abundances are related to the parental magma composition. K_2O abundance is mostly well correlated with LOI (Fig. F50), but the overall amounts remain very low, suggesting very slight chemical mobilization during alteration processes. The exception is the sample from Unit 18, which has high K_2O content and low LOI. As Unit 18 is alkali basalt, this feature is likely related to the primary composition of the magma.

Co/Zr ratios are very constant downhole, with values of ~0.4. Zn/Zr ratios are also fairly constant downhole, with values of ~0.8. Three samples from Subunit 2c and Units 6 and 11 display higher ratios (>1), compatible with their higher LOI and K_2O abundances. One sample from Unit 21 displays a high Zn/Zr ratio (>2) associated with low LOI. This feature is therefore more likely related to the primary composition of the magma. Two groups of samples can be identified with Cu/Zr ratios: a low Cu/Zr group with values of ~0.5 and a high Cu/Zr group with values of 1.1–1.2. The latter is composed of samples from Units 4 and 5 and one sample from Unit 6 (e.g., Sample 197-1206A-18R-1, 80–83 cm). No differences were noted between the alteration assemblages of both groups, and further studies are needed to determine whether the high Cu/Zr ratios are related to alteration processes or to the parental magma composition. The fairly constant Co/Zr and Zn/Zr ratios of the Hole 1206A sequence suggest that mobilization of these trace metals was relatively minor during alteration processes.

Volcaniclastic Units

Subunits 2a and 2c and parts of Units 8, 11, and 14 are described as hyaloclastite olivine basalt breccia. Unit 19 is described as a volcaniclastic basalt breccia (see **"Physical Volcanology and Igneous Petrology,"** p. 6). Alteration features associated with this breccia are similar to those described for basaltic lava flow units; olivine phenocrysts are variably altered to serpentine, iddingsite, or carbonate, and the groundmass is variably altered to clay, Fe oxyhydroxide, or zeolite. Cement is mostly composed of variable proportions of zeolite, green clay, and Fe oxyhydroxide (see also **"Physical Volcanology and Igneous Petrology,"** p. 6).

Summary

All igneous rocks recovered at Site 1206 (Hole 1206A) have undergone low-temperature alteration. Alteration features are defined in the lava flow units in terms of the secondary mineral assemblage, apparent as vesicle filling, vein filling, and replacement of groundmass and primary minerals. Overall, the lava flows are slightly altered, with some exceptions in Units 1, 6, and 17, where the degree of alteration is higher. The alteration assemblage is homogeneous downhole and is composed of Fe oxyhydroxide, saponite and/or nontronite, celadonite, and zeolite. In some specific intervals (e.g., Unit 6 [Core 197-1206A-18R] and Unit 17 [Core 197-1206A-37R]) the occurrence of white–pale green expanding smectite (aliettite) produced a complete disaggrega-

F34. Discrete Cr spinel phenocryst, p. 61.

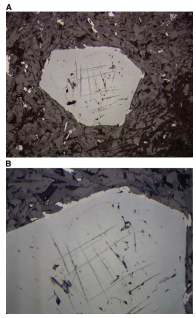

F35. Titanomagnetite overgrowths on Cr spinel crystals, p. 62.

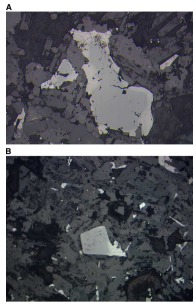

F36. Morphology of olivine phenocrysts and Cr spinel inclusions, p. 63.

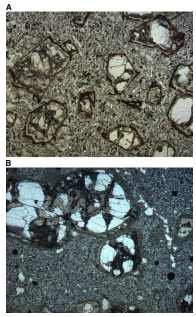

F37. Morphology and composition of Cr spinel phenocrysts, p. 64.

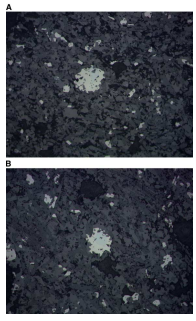

tion of portions of the rock as soon as the core came in contact with water at ambient pressure. This phenomenon can be related to the expandability of smectite, replacing the groundmass in large proportions. Despite this very high level of fracturing, part of these intervals are almost unaltered and contain fresh olivine (see also "Physical Volcanology and Igneous Petrology," p. 6, and "Site 1206 Thin Sections," p. 176). Vesicle and vein fillings present the same mineralogical features. The entire Hole 1206A sequence is sparsely veined, indicating only small-scale fluid circulation. Most of the secondary alteration probably developed in diffuse fluid circulation systems.

All the identified alteration minerals are characteristic of very low temperature conditions. The estimated temperature for the formation of celadonite and nontronite are within the range of 30°–60°C (Alt, 1995), and saponite can form at slightly higher temperature (from 15° to 170°C) (Alt, 1995). In contrast to the first two sites of Leg 197 (Sites 1203 and 1204), K_2O was not greatly mobilized during alteration event(s) at Site 1206. Trace elements also do not show evidence for mobilization, as expected for low-temperature fluid flow.

PALEOMAGNETISM AND ROCK MAGNETISM

Paleomagnetic and rock magnetic measurements at Site 1206, situated south of the summit of Koko Seamount and 6.2 km from DSDP Site 308, focused on assessing the natural remanent magnetization (NRM) of basement rock and obtaining a preliminary paleolatitude estimate for the site during basement formation. Based on nannofossils identified in the washed section of Core 197-1206A-1W and the polarity sequence of minicores sampled, the top of the basement may have formed during magnetic polarity Chron C20n, C21n, or C22n (Berggren et al., 1995; Cande and Kent, 1995) (see "Biostratigraphy," p. 5). Priority was given to shore-based sampling for high-resolution paleomagnetic and rock magnetic study. However, a preliminary estimate of paleolatitude for Koko Seamount is presented below based on paleomagnetic analysis of shipboard samples.

Rock Magnetism

Magnetic Susceptibility, Koenigsberger Ratio, and Stability against Alternating-Field Demagnetization

Low-field volume-normalized magnetic susceptibility was measured on oriented samples (72 basalt and 23 volcaniclastic samples) after alternating-field (AF) demagnetization with the Kappabridge KLY-2 magnetic susceptibility meter. Three measurements were taken for each sample and then averaged. Measurements were repeatable to within 1% of the average value. The range of magnetic susceptibilities of basalt is 2.0×10^{-3} to 39×10^{-3} SI, with an arithmetic mean of 14.4×10^{-3} SI. The range of volcaniclastic samples is 0.34×10^{-3} to 16×10^{-3} SI (mean = 5.57×10^{-3} SI).

The Koenigsberger ratio (Q) was calculated for each sample using a present geomagnetic field intensity of 31.4 A/m (International Geomagnetic Reference Field) (Barton et al., 1995). Koenigsberger ratios of basalt range from 1.8 to 72 (mean = 13.0). Volcaniclastic samples have Koenigsberger ratios that range from 0.3 to 177 (mean = 19).

F38. Titanomagnetite growing around a relict Cr spinel crystal, p. 66.

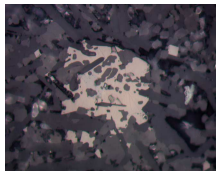

F39. Cr spinel inclusions in altered olivine phenocryst with iddingsite rim, p. 67.

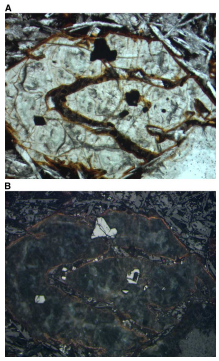

F40. Plagioclase-clinopyroxene glomerocryst containing chromite inclusions, p. 68.

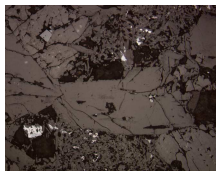

T8. Major and trace elements in basement, p. 106.

F41. Total alkali vs. SiO_2 classification plot, p. 69.

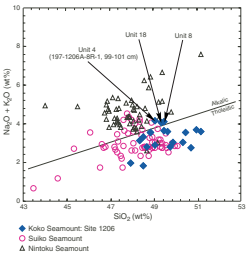

Median destructive fields (MDF) range from 7.5 to >80 mT (above the maximum limit of the AF demagnetizer in line with the superconducting quantum interference device [SQUID] magnetometer) (mean = 29.5 mT). The MDF values of volcaniclastic samples range from 9 to 78 mT (mean = 25.9 mT). Some samples from this site show much higher MDF values as compared to samples from previous Leg 197 sites; the reason for this is not clear given the limits of our preliminary data. We also calculated the ratio of the magnetic component demagnetized between 0 and 5 mT to that demagnetized between 20 and 50 mT (ΔRM) (see "Discussion," p. 21). Figure F51 shows a plot of volume magnetic susceptibility (*K*), the Koenigsberger ratio (*Q*), MDF, and ΔRM vs. depth. *Q*-ratios and MDF values, in general, suggest that a majority of the samples carry a stable remanence that can be used to estimate paleolatitude.

Lowrie-Fuller Tests and Coercivity of Remanence Measurements

Lowrie-Fuller tests (Lowrie and Fuller, 1971) as well as isothermal remanent magnetization acquisition and backfield demagnetization used to measure coercivity of remanence were performed on some samples selected from the lava flow units having a high MDF of NRM (Table T9). In all cases, the MDFs of anhysteretic remanent magnetizations (ARMs) and saturation isothermal remanent magnetization (SIRM) are smaller than the MDFs of NRM.

Some samples (e.g., Samples 197-1206A-3R-2, 99–101 cm, and 16R-5, 75–77 cm) (Figs. F52A, F52D, F53A, F53D) show a rapid decrease of ARM and SIRM and a fairly low coercivity of remanence. This behavior, together with the high MDF of NRM, suggests a mixture of magnetic grains having different sizes. In other samples, the sigmoidal shape of the ARM and SIRM decay and the high value of the coercivity of remanence indicates the presence of single-domain grains (e.g., Samples 197-1206A-4R-5, 55–57 cm; 9R-2, 29–31 cm; 22R-1, 117–119 cm; and 28R-1, 97–99 cm) (Figs. F52B, F52C, F52E, F53B, F53C, F53E). These samples also show little or no decrease in NRM when demagnetized up to 20 mT (Samples 197-1206A-4R-5, 55–57 cm, and 22R-1, 117–119 cm) (Fig. F54), suggesting single-domain behavior.

The behavior of Sample 197-1206A-28R-1, 97–99 cm (Fig. F52F), is more complex. The MDF of NRM is very high. The ARM does not decrease before demagnetization to 25 mT, but the SIRM shows a continuous, slow decrease with AF demagnetization. This may be explained by the presence of a high-coercivity mineral (such as goethite) in the dark brown clay observed in the sample matrix in addition to titanomagnetite (see "Physical Volcanology and Igneous Petrology," p. 6).

Secondary Magnetic Components

Most of samples have a soft magnetic component that is demagnetized after treatment to 5 mT (Figs. F54, F55, F56, F57). The ratio of this soft component (0–5 mT) to a part of the stable component (20–50 mT) (ΔRM) is useful to illustrate the relative contribution of the soft component to the total NRM (Fig. F55B). ΔRM derived from paleomagnetic data from lava flow and volcaniclastic samples is not strongly correlated to the compressional wave velocity (V_P) measured with a PWS3 system (see "Physical Properties," p. 22; Fig. F55A). These observations contrast with those from Site 1205 (see "Paleomagnetism and Rock Magnetism," p. 21, in the "Site 1205" chapter) and attest to the relatively

F42. Na_2O, K_2O, TiO_2, CaO, Al_2O_3, and Zr vs. MgO, p. 70.

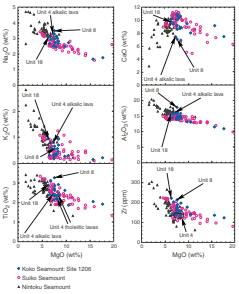

F43. Abundance of Sc vs. MgO, p. 71.

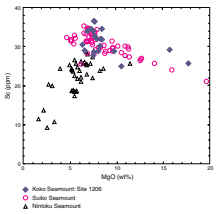

F44. Ba, Sr, and Ti vs. Zr, p. 72.

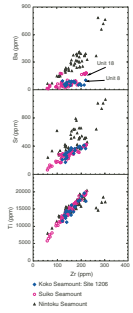

F45. Alkalinity vs. depth in igneous basement, p. 73.

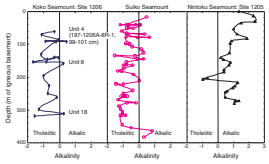

F46. TiO_2 and Zr vs. MgO, p. 74.

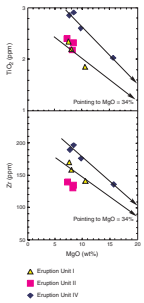

unaltered state of the rocks. The inclination of the 0- to 5-mT soft component from samples with log (ΔRM) > 1.0 tends to be steep and positive (>70°). Magnetic minerals responsible for the origin of the soft components will be studied on shore.

Paleomagnetism of Lava Flows and Volcaniclastic Rocks in Basement

Lava flows and sedimentary units comprising basement (see "Physical Volcanology and Igneous Petrology," p. 6) were sampled for paleomagnetic analysis. Four or more samples were measured for most lava flows. Fewer samples (one to three) were taken for shipboard analysis from the units dominated by lapilli breccia with basalt lobes and lava flow units that showed extensive fracturing due to the expansion of clay; material was reserved in these units for high-resolution shore-based studies. Sample inclinations for each basement unit were averaged using the method of McFadden and Reid (1982).

Minicore samples of lava flow and volcaniclastic sediment were measured using the 2-G Enterprises SQUID magnetometer. Each minicore was demagnetized by stepwise AF demagnetization following the same measurement routine employed at Site 1205. A total of 72 lava flow and 23 volcaniclastic minicores were measured.

Demagnetization Behavior

Orthogonal vector diagrams were used to characterize the demagnetization behavior and assess the number of magnetization components represented (Figs. F57, F58). Normal and reversed polarities were recorded. Reversed polarity samples showed a small normal polarity overprint that was demagnetized after 5–10 mT. Normal polarity samples often displayed curved behavior at low-field steps (Fig. F59A, F59B, F59D), suggesting the presence of more than one magnetic component. Primary characteristic remanent magnetization (ChRM) directions were fit using principal component analysis (Kirschvink, 1980) from 35 or 40 mT through 80 mT on many of the normal polarity lava flow samples.

Volcaniclastic samples, in general, had weak NRM values (one to two orders of magnitude less than the NRM values of the lava flows) and were often demagnetized to <10% of the NRM intensity at low-field steps (Fig. F56). Lava flow samples showed uniform demagnetization toward the origin after the removal of a small overprint (Fig. F57). The presence of a high-coercivity mineral is suggested by the inability of AF demagnetization to remove the remanence to <10% of the NRM value in ~60% of the samples (Fig. F58). In three samples (e.g., Fig. F59C), <50% of the total NRM was demagnetized by the last measurement step.

Characteristic Remanent Magnetization Directions and Inferred Paleolatitudes

Three polarity intervals were recognized in the Site 1206 basement section. Samples from Cores 197-1206A-2R through 6R are normal polarity. Core 197-1206A-7R through Sample 197-1206A-9R-1, 29–31 cm, are reversed polarity. Sample 197-1206A-9R-2, 110–112 cm, is normal polarity. Because of limited recovery and/or unoriented core pieces in Cores 197-1206A-10R through 14R, samples were not taken for shipboard analysis. Samples from Cores 197-1206A-15R through 43R are

F47. Alteration minerals, veins, and vesicle fillings, p. 75.

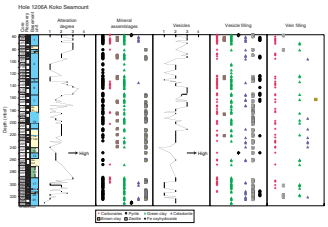

F48. Vesicle filled with brown clay and saponite, p. 76.

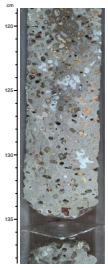

F49. Vesicle filled with brown clay, saponite, celadonite, and carbonate, p. 77.

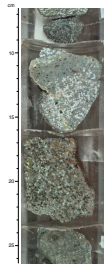

F50. LOI, K_2O, Cu/Zr, Co/Zr, and Zn/Zr, p. 78.

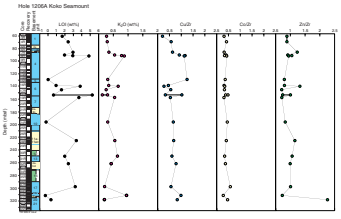

F51. Magnetic susceptibility, Q-ratio, MDF, and ΔRM, p. 79.

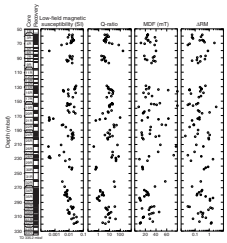

normal polarity. Based on the observed polarity sequence and time constraints based on nannofossils from the washed core (see **"Biostratigraphy,"** p. 5), the sequence of magnetic chrons recorded may be C20n–C20r–C21n, C21n–C21r–C22n, or C22n–C22r–C23n. Given a radiometric age of 48.1 ± 0.8 Ma based on dredge samples from Koko Seamount (Clague and Dalrymple, 1973), one of the latter two polarity chron assignments is more probable.

ChRM inclinations for volcaniclastic sediments were generally fit between 15–45 or 50 mT. Only samples with maximum angular dispersion angles <10° were considered reliable. In some samples (three of the volcaniclastic samples measured), the demagnetization vectors were stable but did intersect the origin. Nine samples had a stable magnetization with vectors going into the origin. The remaining samples (11) did not have a stable demagnetization.

Sediment generally averages more geomagnetic time than a single lava flow. If we give equal weight to data from each of the volcaniclastic sediment samples that have reliable ChRM inclination fits, the mean inclination is 42.5° (95% confidence interval = ±2.5°) using the method of McFadden and Reid (1982). This suggests a paleolatitude of 24.6° (95% confidence interval = ±1.9°; N = 9) (Table **T10**).

ChRM inclination directions from lava flow samples were fit between 30 or 35 mT through 80 mT. Inclinations were grouped first according to petrologic units (see **"Physical Volcanology and Igneous Petrology,"** p. 6) and averaged using the method of McFadden and Reid (1982). Two petrologic units were further broken down in terms of magnetic time units on the basis of polarity change (basement Unit 4) and stratigraphic inclination groupings (basement Unit 6) (see Table **T11**). Fourteen magnetic time units were identified, with a mean inclination value of 38.5° (95% confidence interval = +8.4°/–10.9°), suggesting a paleolatitude of 21.7° (95% confidence interval = +6.4°/–7.0°) (Table **T11**).

Discussion

Paleolatitudes based on sediment may suffer from a bias toward shallower values because of detrital inclination error (King, 1955) or compaction-induced inclination shallowing (Anson and Kodama, 1987). The paleolatitude of the volcaniclastic interbeds (24.6°; 95% confidence interval = ±1.9°), however, is similar to that based on the basalt units (21.7°; 95% confidence interval = +6.4°/–7.0°). But because of the small number of samples used in the inclination average, the uncertainty of the paleolatitude based on the volcaniclastic units may be underestimated.

The angular polar dispersion (S) of the paleomagnetic data from the lava flow units can be estimated by transforming the estimate of the directional precision parameter (k) (McFadden and Reid, 1982) into pole space (Cox, 1970; Tarduno and Sager, 1995). For 14 inclination units, S = 16.2°. This value is slightly higher than that expected based on global data from 45- to 80-Ma lava flows (S = 12.2° ± 1.6°) (McFadden et al., 1991). The distribution of lava flow inclinations appears to represent well the range of values expected from a Fisher distribution (Fisher, 1953) (Fig. **F60**). Some serial correlation may exist between some of the lava flow units sampled (e.g., Units 5 and 6, 10, and 11). However, the limited number of samples collected per lava flow unit for shipboard analysis limits further consideration of this aspect; this will be addressed in shore-based studies.

T9. Lava flow rock magnetic parameters, p. 108.

F52. Lowrie-Fuller tests on lava flow samples, p. 80.

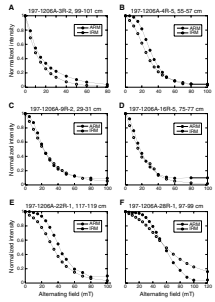

F53. IRM acquisition and demagnetization, p. 81.

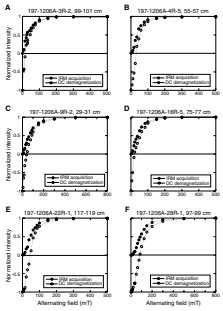

F54. NRM decay spectra and Lowrie-Fuller tests, p. 82.

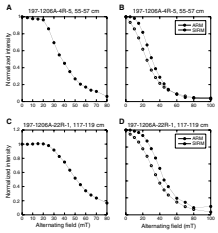

F55. Logarithm of ΔRM vs. compressional wave velocity, p. 83.

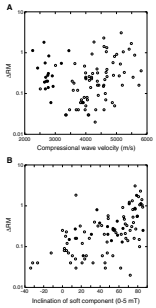

The preliminary paleolatitude mean derived from the Site 1206 lava flow samples is ~3° from the present-day latitude of the Hawaiian hotspot (~19°). Paleomagnetic data from Sites 1203, 1204, 1205, and 1206 are consistent with Late Cretaceous–early Tertiary hotspot motion during the formation of the Emperor Seamounts (Tarduno and Cottrell, 1997; Cottrell and Tarduno, in press). The preliminary paleomagnetic data from Site 1206 hint at a slowing of hotspot motion at 48 Ma, near the bend in the Hawaiian-Emperor chain. This possibility will be further examined in shore-based studies utilizing thermal demagnetization.

PHYSICAL PROPERTIES

All cores from Section 197-1206A-2R-2 through Core 45R were run through the multisensor track (MST) to measure natural gamma radiation (NGR). Because of the limited amount of sedimentary material recovered, gamma ray attenuation (GRA) bulk density and magnetic susceptibility were only measured on Sections 197-1206A-34R-2 through 36R-2. Index properties (bulk density, grain density, and porosity) and thermal conductivity were determined on one or two discrete samples per core, except for some of the sedimentary units where one sample was collected per section. Compressional wave velocities were measured at a frequency of one or two samples per section.

MST Measurements

Magnetic Susceptibility

Volume-normalized magnetic susceptibility was measured at 5-cm intervals on Sections 197-1206A-34R-2 through 36R-2 to assist in interpretation of the lithostratigraphy (Table **T12**). Magnetic susceptibility values for this section range from 20×10^{-6} to 1480×10^{-6} SI (mean = 605×10^{-6} SI).

GRA Density

Bulk density was measured by the GRA densitometer every 5 cm on Sections 197-1206A-34R-2 through 35R-6 (Table **T13**). GRA bulk density generally ranges from 0.3 to 2.2 g/cm³ (mean = 1.8 g/cm³) and over the measurement interval varies little with depth. Data points with negative or very low density (<< 1.0 g/cm³) probably represent voids or areas of drilling disturbance.

Natural Gamma Radiation

NGR was measured every 10 cm from Section 197-1206A-2R-2 to Core 45R (Table **T14;** Fig. **F61A**). Total counts are reported here because the corrected counts (which are less by ~16 counts per second [cps]) include negative values that are physically unreasonable.

NGR values at Site 1206 range from 12.9 to 34.3 cps (mean = 18.8 cps). In the upper part of the basement section, from ~57 to 99 mbsf, total gamma ray counts decrease slightly with depth from ~19 to ~16.7 cps. This is succeeded by cycles of overall increasing NGR with depth, from 123 to 145.5 and from 145.5 to 246 mbsf. A slight decrease in NGR is observed at 267 mbsf that is succeeded by an increase from ~18

F56. Orthogonal vector plots of volcaniclastic sediments, p. 84.

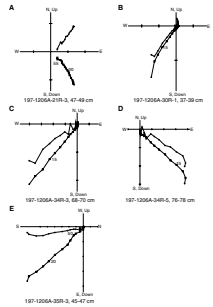

F57. Orthogonal vector plots of lava flows, p. 85.

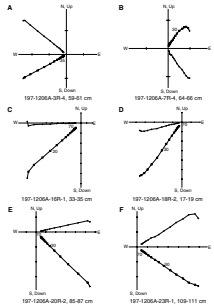

F58. Orthogonal vector plots of incompletely demagnetized lava flow samples, p. 86.

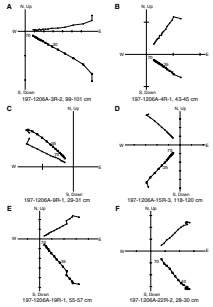

F59. Orthogonal vector plots of nonideal behavior by lava flow samples, p. 87.

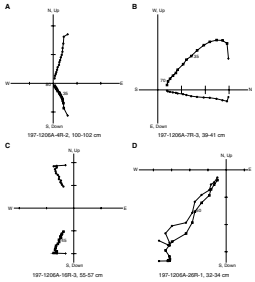

T10. Volcaniclastic ChRM inclination and summary statistics, p. 109.

to ~22 cps between 267 and 287 mbsf in the base of basement Unit 17 (see "Physical Volcanology and Igneous Petrology," p. 6). An abrupt decrease in NGR occurs at 287 mbsf. Below this depth core sections show a wide range of NGR values; this behavior continues to the base of the recovered sequence. Total NGR counts in basement Units 8 and 19, which contain breccia, tend to be higher than the counts in the basalt units above and below. The highest counts were measured in the sedimentary sandstone, limestone, and soil Units 12, 15,16,18, 20, and 22.

Core Imaging

Whole-round core images were taken of cylindrical pieces from the Hole 1206A core. Over 110 m of core images were recorded, representing ~77% of the recovered material. However, because of hole deterioration and wall collapse, downhole logging was not performed at Site 1206; hence, correlation of core image and logging data is not possible at this site.

Thermal Conductivity

Thermal conductivity was measured on one or two pieces per core at Site 1206 (Table T15; Fig. F62). Thermal conductivity values of the 30 basalt samples measured ranged between 1.057 and 2.283 W/(m·K) (average = 1.626 W/[m·K]). Five measurements taken on samples from sandstone units in the basement generally gave lower values, between 1.076 and 1.601 W/(m·K) (average = 1.314 W/[m·K]). Five measurements taken on breccia generally gave still lower values, between 0.96 and 1.419 W/(m·K) (average = 1.314 W/[m·K]). One measurement taken on a deeply weathered flow top yielded 1.076 W/(m·K).

Index Properties

At Site 1206, index properties were usually determined on one sample per core. If different lithologies were present in the core, more than one sample per core was taken. Values of wet mass, dry mass, and dry volume of the samples were measured and used to calculate moisture content, bulk density, grain density, and porosity (Table T16; Fig. F61B, F61C, F61D). Basement lava flow units showed considerable variation in bulk density with depth, with values ranging between ~2.0 and 3.0 g/cm³. There is also a corresponding variation in porosity, with values ranging between ~5% and 40%. Grain density of basalt was more uniform, with mean values of ~3.0 g/cm³. Little systematic variation with depth is observed. Units of breccia and fine-grained sedimentary beds both in and above the basement all had a grain density of ~2.8 g/cm³, bulk density of ~2.1 g/cm³, and porosity of ~40%.

Compressional Wave Velocity

Compressional wave velocity measurements were made on discrete samples from Hole 1206A at a frequency of approximately one per section. *P*-wave velocity was measured in the x- and z-directions for the basement samples. On selected samples, *P*-wave velocity was also measured in the y-direction.

P-wave velocity varies widely throughout Hole 1206A, ranging from ~2215 to 5820 m/s (mean = ~ 4000 m/s) (Table T17; Fig. F63). Velocities determined in the x-, y-, and z-directions differ by up to 300 m/s, and it

T11. Lava flow ChRM inclination and summary statistics, p. 110.

F60. Inclination values compared to a synthetic Fisher distribution, p. 88.

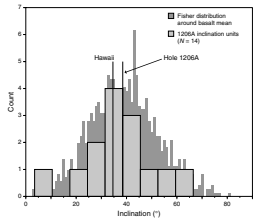

T12. Magnetic susceptibility, p. 111.

T13. GRA bulk density, p. 112.

T14. Natural gamma ray measurements, p. 113.

F61. Physical properties, p. 89.

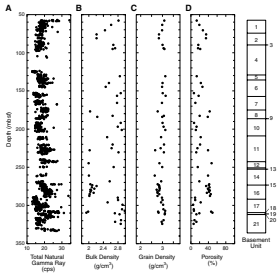

T15. Thermal conductivity, p. 114.

F62. Thermal conductivity, p. 90.

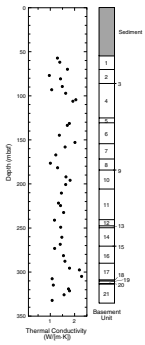

is not immediately apparent whether this represents anisotropy or inadequate coupling between sample and transducers as described in previous chapters. As would be expected, higher compressional wave velocity is present in the lava flow units than in the volcaniclastic and sedimentary interbeds. Particularly high compressional wave velocity (>5500 m/s) was recorded in basement Unit 17, a highly olivine-phyric basalt (see "Physical Volcanology and Igneous Petrology," p. 6).

When plotting *P*-wave velocity vs. bulk density at the same sampling locations, it is apparent that *P*-wave velocity and bulk density of basalts are correlated; the lowest densities (~2.4 g/cm³) correspond to the lowest velocities (~3400 m/s), and the highest densities (~2.9 g/cm³) correspond to the highest velocities (~5300 m/s) (Fig. F64). Data points for sediments plotted on the same bulk sound velocity vs. density diagram plot as a separate cluster around 2800 m/s and 2.05 g/cm³.

UNDERWAY GEOPHYSICS

Seismic Reflection Profiling

Initial selection of proposed Site HE-6A, the target location for Site 1206, was based on data gathered at DSDP Site 308. Previous drilling at this site penetrated ~70 m of clay and volcaniclastic sandstone but did not reach basement (Larson, Moberly, et al., 1975). We conducted a single-channel seismic survey, 3.5-kHz PDR, and magnetometer survey in the vicinity of Site 308 to ensure proper hole location and suitability for basement drilling. Analog seismic data (*S.P. Lee,* 8-76-NP, 9 October 1976, 0700 hr universal time coordinated) were available in the vicinity of Site 308. Figure F65 shows the track line of the *S.P. Lee* cruise and the Leg 197 survey superimposed on ETOPO5 seafloor bathymetry with a contour interval of 250 m. Tick marks along our survey lines mark half-hour intervals. Line 1 is approximately in the same location and azimuth as the *SP Lee* 8-76 line.

Survey Lines 3 and 6 pass directly over Site 1206, which is ~6.2 km south of DSDP Site 308. Approximately 2.5-km-long sections from Lines 3 and 6 are shown in Figures F66 and F67, respectively. The midpoint of the active part of the streamer was ~218 m astern of the water gun source, which was ~4.5–6 m deep. The midpoint between the active section of the streamer and the water gun source was ~191 m astern of the ship's recorded GPS position. Firing of the water gun was set at 4 s. Each shot record is 3 s in record length, beginning 100 ms before the water gun was triggered. This 100-ms delay, created by the trigger control panel, was removed during SIOSEIS record processing. Ship speed averaged 6.02 kt (3.25 m/s) during Line 1 and 6.05 kt (3.27 m/s) during Line 6. Both lines were processed with SIOSEIS seismic processing software (version 2001.3) (http://sioseis.ucsd.edu), using predictive deconvolution, bandpass filtering from 55 to 150 Hz (Line 3) and 45 to 120 Hz (Line 6), and finite-difference migration using a simple velocity model. Table T18 shows the SIOSEIS script processing parameters for each line.

At Site 1206, a thin sequence of internally reflective sediment, ~57 m thick, overlies a reverberant volcanic basement. A series of laterally coherent reflections characterizes this section, which has a reflection time of 0.04 s two-way traveltime (TWT). Acoustically defined bedding generally conforms to basement topography. A sharp decrease in lateral continuity of reflection events delineates the top of the volcanic basement. From ~2.1 s TWT at the northeast end of Line 3 (Fig. F66), the

T16. Index properties, p. 115.

T17. Compressional wave velocity, p. 116.

F63. Compressional wave velocity, p. 91.

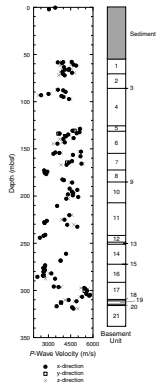

F64. Bulk density vs. *P*-wave velocity, p. 92.

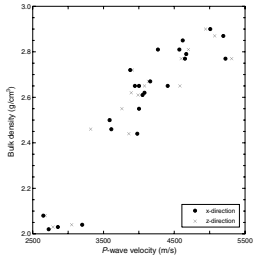

F65. Site 1206 and *SP Lee* 8-76 surveys, p. 93.

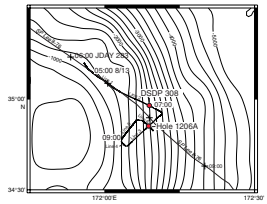

F66. Survey Line 3 migrated time section, p. 94.

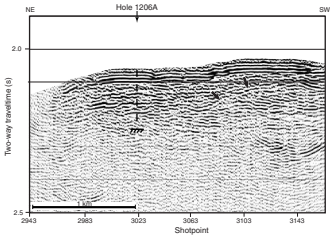

top of the basement slopes gently upward to ~2.075 s TWT near shotpoint 3080. Relatively large-amplitude, laterally coherent basement reflections are attributed to the presence of volcaniclastic units and shallow-water sediment interbedded with lava flows. Truncation of slightly southwest-dipping basement reflections between 2.125 and 2.2 s TWT and shotpoints 3083 and 3163 on Line 3, indicated by arrows in Figure **F66,** might record a boundary separating two sequences of lava flows. Line 6 (Fig. **F67**) shows a sharp apparent offset, nearly 0.1 s TWT down to the southeast, in the sediment sequence at shotpoint 4947. This apparent offset is probably a small fault scarp, although the apparent offset might be due to the inability of SIOSEIS's finite-difference migration algorithm to properly migrate the steep dip of the sediment reflections. Finally, because elsewhere the sediment layer appears to conform to basement topography, another possible explanation is that the sediment sequence along Line 3 may have been largely deposited as a drape over a preexisting step in the basement.

F67. Survey Line 6 migrated time section, p. 95.

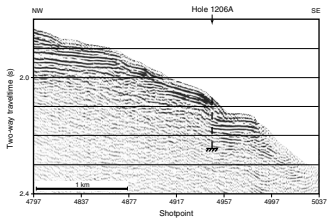

T18. SIOSEIS process parameters, p. 117.

REFERENCES

Alt, J.C., 1995. Subseafloor processes in mid-ocean ridge hydrothermal systems. *In* Humphris, S.E., Zierenberg, R., Mullineaux, L., and Thomson, R. (Eds.), *Seafloor Hydrothermal Systems: Physical, Chemical, Biological and Geological Interactions within Hydrothermal Systems*. Geophys. Monogr., Am. Geophys. Union, 91:85–114.

Anson, G.L., and Kodama, K.P., 1987. Compaction-induced shallowing of the post-depositional remanent magnetization in a synthetic sediment. *Geophys. J. R. Astron. Soc.,* 88:673–692.

Barton, C.E., Baldwin, R.T., Barraclough, D.R., et al., 1995. International Geomagnetic Reference Field, 1995 revision presented by IAGA Division V, Working Group 8. *Phys. Earth Planet. Int.,* 97:23–26.

Berggren, W.A., Kent, D.V., Swisher, C.C., III, and Aubry, M.-P., 1995. A revised Cenozoic geochronology and chronostratigraphy. *In* Berggren, W.A., Kent, D.V., Aubry, M.-P., and Hardenbol, J. (Eds.), *Geochronology, Time Scales and Global Stratigraphic Correlation*. Spec. Publ.—Soc. Econ. Paleontol. Mineral., 54:129–212.

Bukry, D., 1975. Coccolith and silicoflagellate stratigraphy, northwestern Pacific Ocean, Deep Sea Drilling Project Leg 32. *In* Larson, R.L., Moberly, R., et al., *Init. Repts. DSDP,* 32: Washington (U.S. Govt. Printing Office), 677–701.

Cande, S.C., and Kent, D.V., 1995. Revised calibration of the geomagnetic polarity timescale for the Late Cretaceous and Cenozoic. *J. Geophys. Res.,* 100:6093–6095.

Cas, R.A.F., and Wright, J.V., 1987. *Volcanic Successions: Modern and Ancient:* London (Allen and Unwin).

Clague, D.A., and Dalrymple, G.B., 1973. Age of Koko Seamount, Emperor Seamount chain. *Earth. Planet. Sci. Lett.,* 17:411–415.

————, 1987. The Hawaiian-Emperor volcanic chain, Part I. Geologic evolution. *In* Decker, R.W., Wright, T.L., and Stauffer, P.H. (Eds.), *Volcanism in Hawaii*. Geol. Surv. Prof. Pap. U.S., 1350:5–54.

Cottrell, R.D., and Tarduno, J.A., in press. A Late Cretaceous pole for the Pacific plate: implications for apparent and true polar wander and the drift of hotspots. *Tectonophysics.*

Cox, A.V., 1970. Latitude dependence of the angular dispersion of the geomagnetic field. *Geophys. J. R. Astron. Soc.,* 20:253–269.

Dalrymple, G.B., Greene, H.G., Ruppel, B.D., Bear, T.E., and Clague, D.A., 1980. Pre-Leg 55 site survey geophysical data from R/V *S.P. Lee* cruise LEE8-76-NP. *In* Jackson, E.D., Koizumi, I., et al., *Init. Repts. DSDP,* 55: Washington (U.S. Govt. Printing Office), 801–844.

Davies, T.A., Wilde, P., and Clague, D.A., 1972. Koko seamount: a major guyot at the southern end of the Emperor seamounts. *Mar. Geol.,* 13:311–321.

Deer, W.A., Howie, R.A., and Zussman, J., 1992. *An Introduction to the Rock-Forming Minerals* (2nd ed.): London (Longman).

Fisher, R.A., 1953. Dispersion on a sphere. *Proc. R. Soc. London A,* 217:295–305.

Folk, R.L., 1962. Practical petrographical classification of limestones. *AAPG Mem.,* 1:108–121.

Greene, H.G., Clague, D.A., and Dalrymple, G.B., 1980. Seismic stratigraphy and vertical tectonics of the Emperor Seamounts, DSDP Leg 55. *In* Jackson, E.D., Koizumi, I., et al., *Init Repts. DSDP,* 55: Washington (U.S. Govt. Printing Office), 759–788.

Hon, K., Kauahikaua, J.P., Denlinger, R., and Mackay, K., 1994. Emplacement and inflation of pahoehoe sheet flows: observations and measurements of active lava flows on Kilauea, Hawaii. *Geol. Soc. Am. Bull.,* 106:351–370.

Jackson, E.D., Koizumi, I., Dalrymple, G.B., Clague, D.A., Kirkpatrick, J., and Green, H.G., 1980. Introduction and summary of results from DSDP Leg 55, the Hawaiian-Emperor hotspot experiment. *In* Jackson, E.D., Koizumi, I., et al., *Init. Repts., DSDP,* 55: Washington (U.S. Govt. Printing Office), 5–31.

Jones, J.G., and Nelson, P.H.H., 1970. The flow of basalt from air into water: its structural expression and stratigraphic significance. *Geol. Mag.,* 107:13–21.

King, R.F., 1955. The remanent magnetism of artificially deposited sediments. *Mon. Not. R. Astron. Soc., Geophys. Suppl.,* 7:115–134.

Kirschvink, J.L., 1980. The least-squares line and plane and the analysis of palaeomagnetic data. *Geophys. J. R. Astron. Soc.,* 62:699–718.

Larson, R.L., Moberly, R., et al., 1975. *Init. Repts. DSDP,* 32: Washington (U.S. Govt. Printing Office).

Lowrie, W., and Fuller, M., 1971. On the alternating field demagnetization characteristics of multidomain thermoremanent magnetization in magnetite. *J. Geophys. Res.,* 76:6339–6349.

Macdonald, G.A., and Katsura, T., 1964. Chemical composition of Hawaiian lavas. *J. Petrol.,* 5:82–133.

McFadden, P.L., Merrill, R.T., McElhinny, M.W., and Lee, S., 1991. Reversals of the Earth's magnetic field and temporal variations of the dynamo families. *J. Geophys. Res.,* 96:3923–3933.

McFadden, P.L., and Reid, A.B., 1982. Analysis of paleomagnetic inclination data. *Geophys. J. R. Astron. Soc.,* 69:307–319.

McKenzie, J., Bernoulli, D., and Schlanger, S.O., 1980. Shallow-water carbonate sediments from the Emperor Seamounts: their diagenesis and paleogeographic significance. *In* Jackson, E.D., Koizumi, I., et al., *Init. Repts DSDP,* 55: Washington (U.S. Govt. Printing Office), 415–455.

Moore, J.G., Phillips, R.L., Grigg, R.W., Peterson, D.W., and Swanson, D.A., 1973. Flow of lava into the sea, 1969–1971, Kilauea volcano, Hawaii. *Geol. Soc. Am. Bull.,* 84:537–546.

Perch-Nielsen, K., 1985. Cenozoic calcareous nannofossils. *In* Bolli, H.M., Saunders, J.B., and Perch-Nielsen, K. (Eds.), *Plankton Stratigraphy:* Cambridge (Cambridge Univ. Press), 427–554.

Schlanger, S.O., and Konishi, K., 1975. The geographic boundary between the coral-algal and the bryozoan-algal limestone facies: a paleolatitude indicator. Theme I, Indicateurs Sedimentologiques, IX^{me} Congres Int. De Sedim., Nice, France, 187–190.

Self, S., Keszthelyi, L., and Thordarson, T., 1998. The importance of pahoehoe. *Annu. Rev. Earth Planet. Sci,* 26:81–110.

Shipboard Scientific Party, 1975. Site 308: Koko Guyot. *In* Larson, R.L., Moberly, R., et al., *Init. Reports DSDP,* 32: Washington (U.S. Govt. Printing Office), 215–226.

Siesser, W.G., 1983. Paleogene calcareous nannofossils from Alabama, Mississippi, and Tennessee. *Miss. Bull. Geol.,* 53.

Tarduno, J.A., and Cottrell, R.D., 1997. Paleomagnetic evidence for motion of the Hawaiian hotspot during formation of the Emperor Seamounts. *Earth Planet. Sci. Lett.,* 153:171–180.

Tarduno, J.A., and Sager, W.W., 1995. Polar standstill of the mid-Cretaceous Pacific plate and its geodynamic implications. *Science,* 269:956–959.

Figure F1. Bathymetry in the region of Koko Seamount, southern Emperor Seamount chain, from ETOPO2 database. Shown are the *S.P. Lee* cruise LEE8-76-NP seismic reflection survey track line and the locations of DSDP Sites 308, 309, and ODP Site 1206 (34°55.55′N, 172°08.75′E). Kimmei Seamount rises south of 34°.

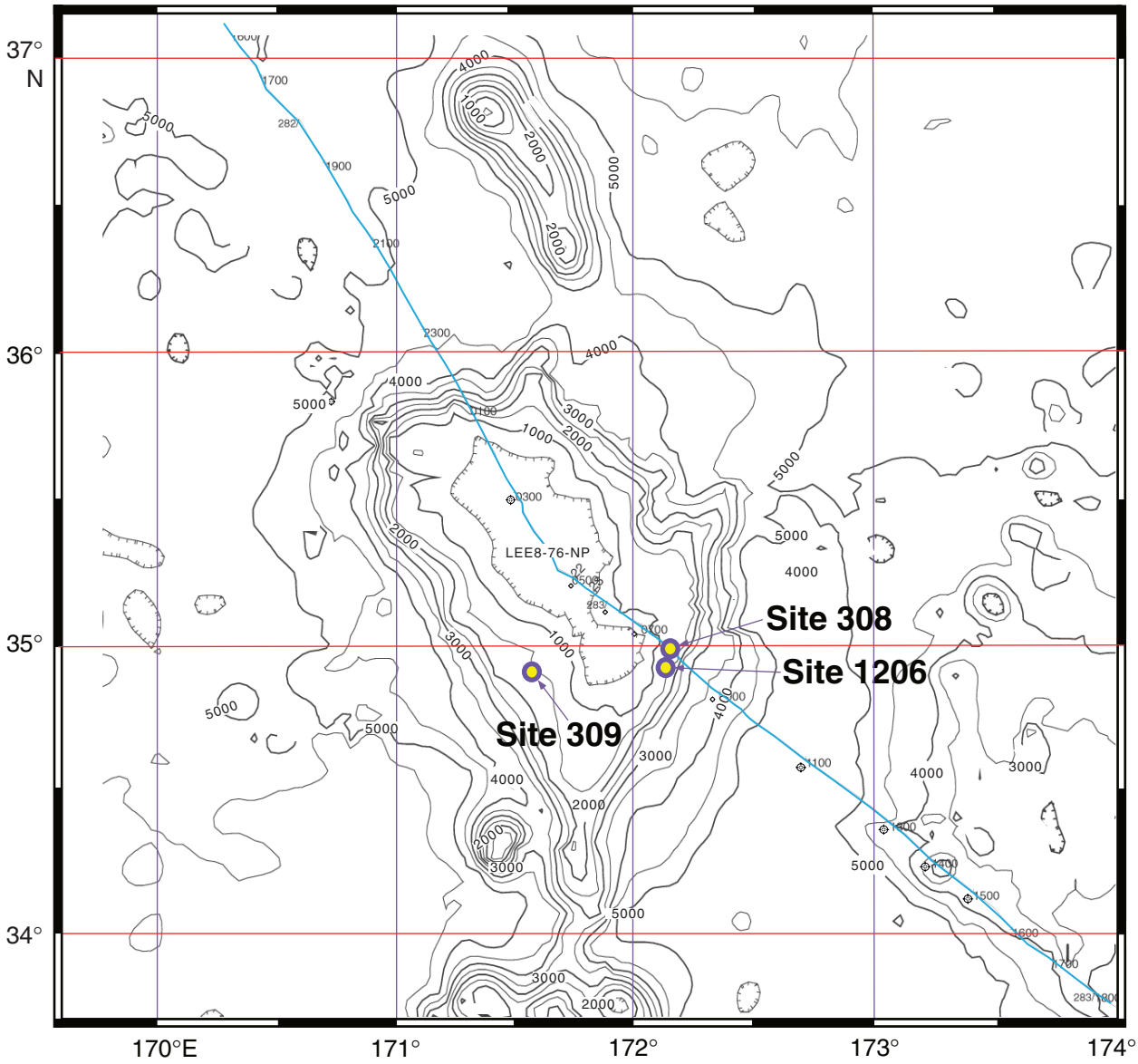

Figure F2. Diagram summarizing the recovery, thickness, chemical composition, and major lithologic features of the basement units from Hole 1206A.

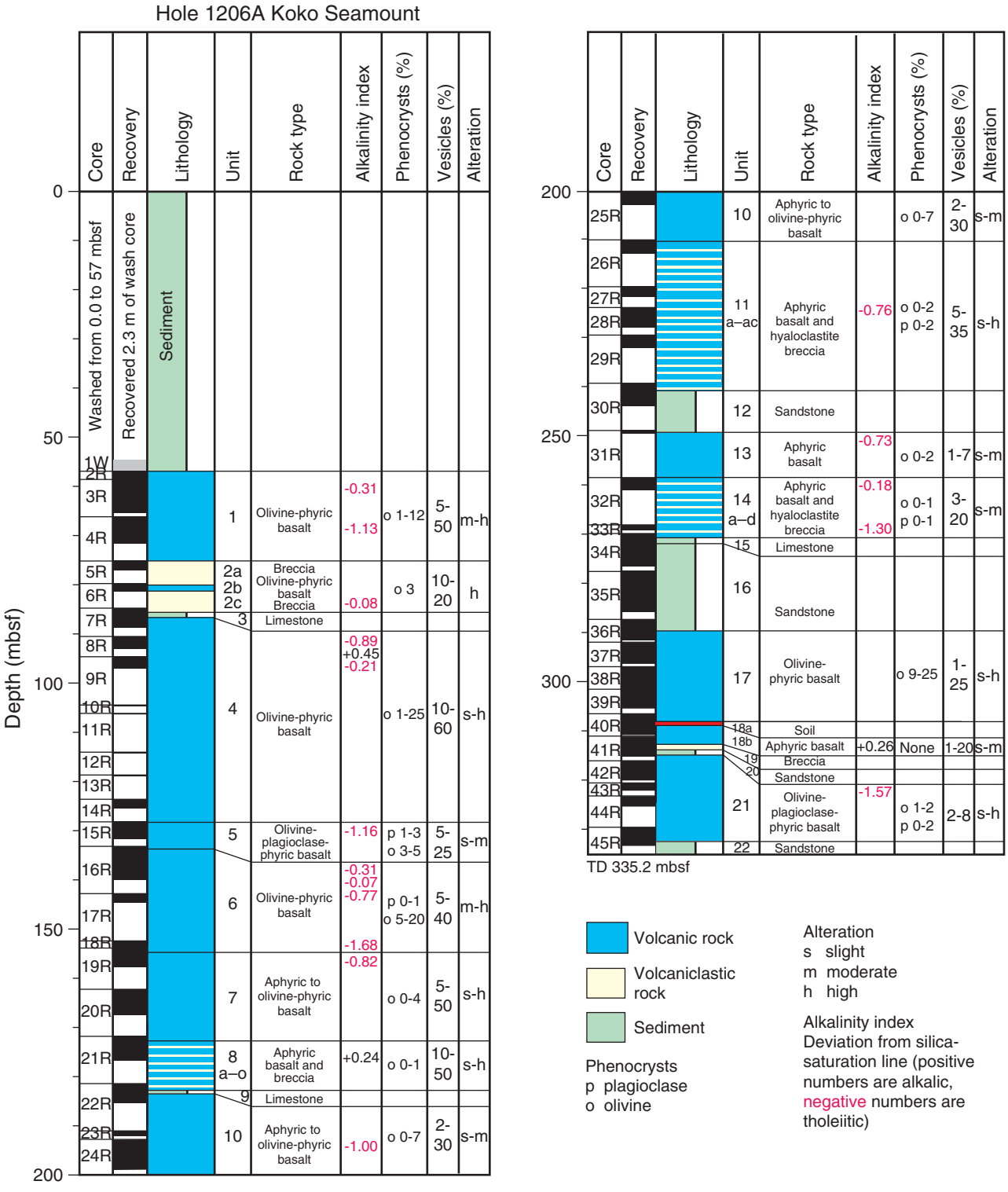

Figure F3. Ti/Zr ratio vs. depth in the basement showing that samples in Eruption Units I, II, IV, and VII have similar Ti/Zr, but samples in Eruption Units V and VI have different Ti/Zr.

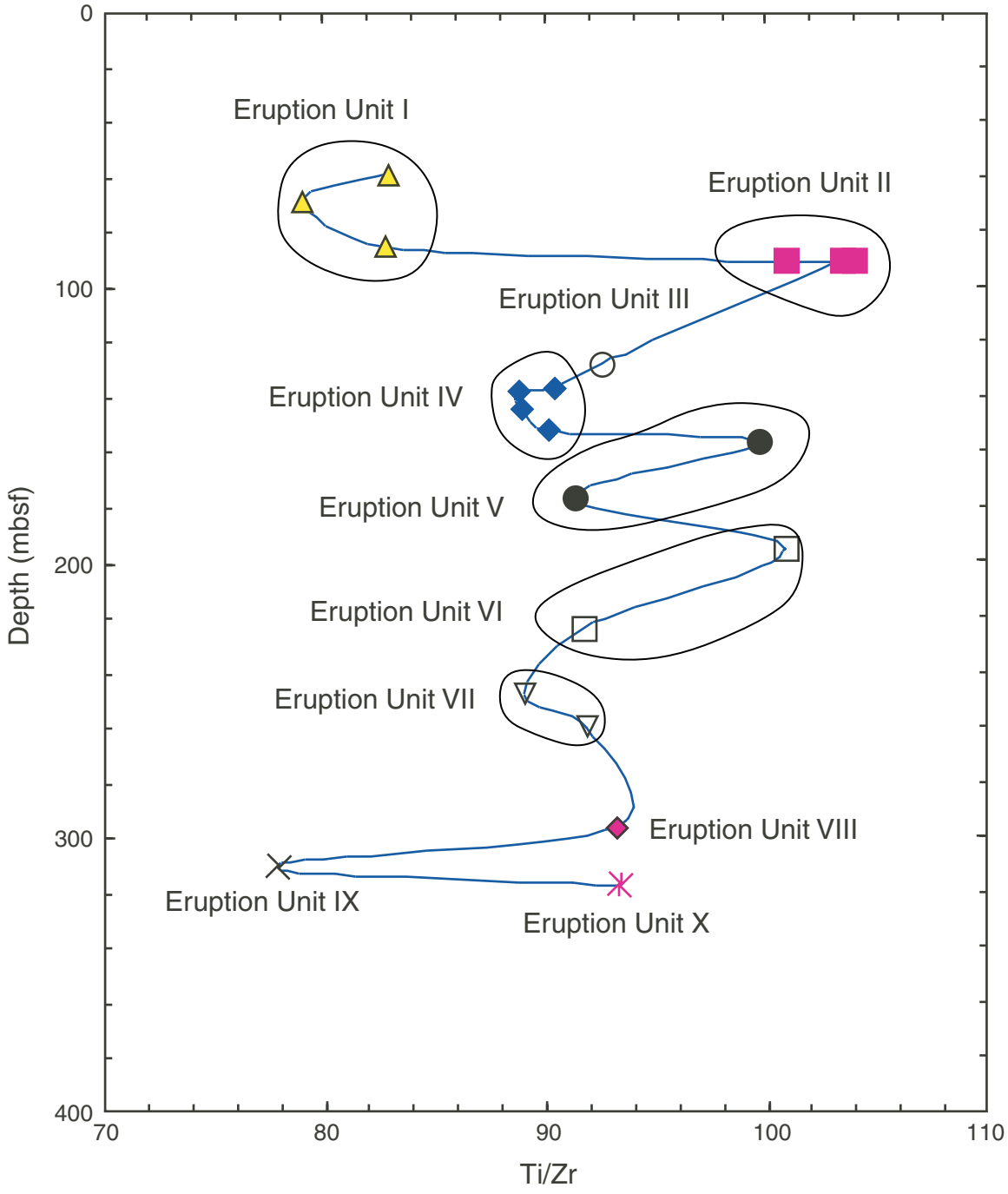

Figure F4. Example of the characteristic internal architecture of an eruption unit (VI) at Site 1206, represented by subaerial compound pahoehoe (Unit 10) and the associated lava delta (Unit 11).

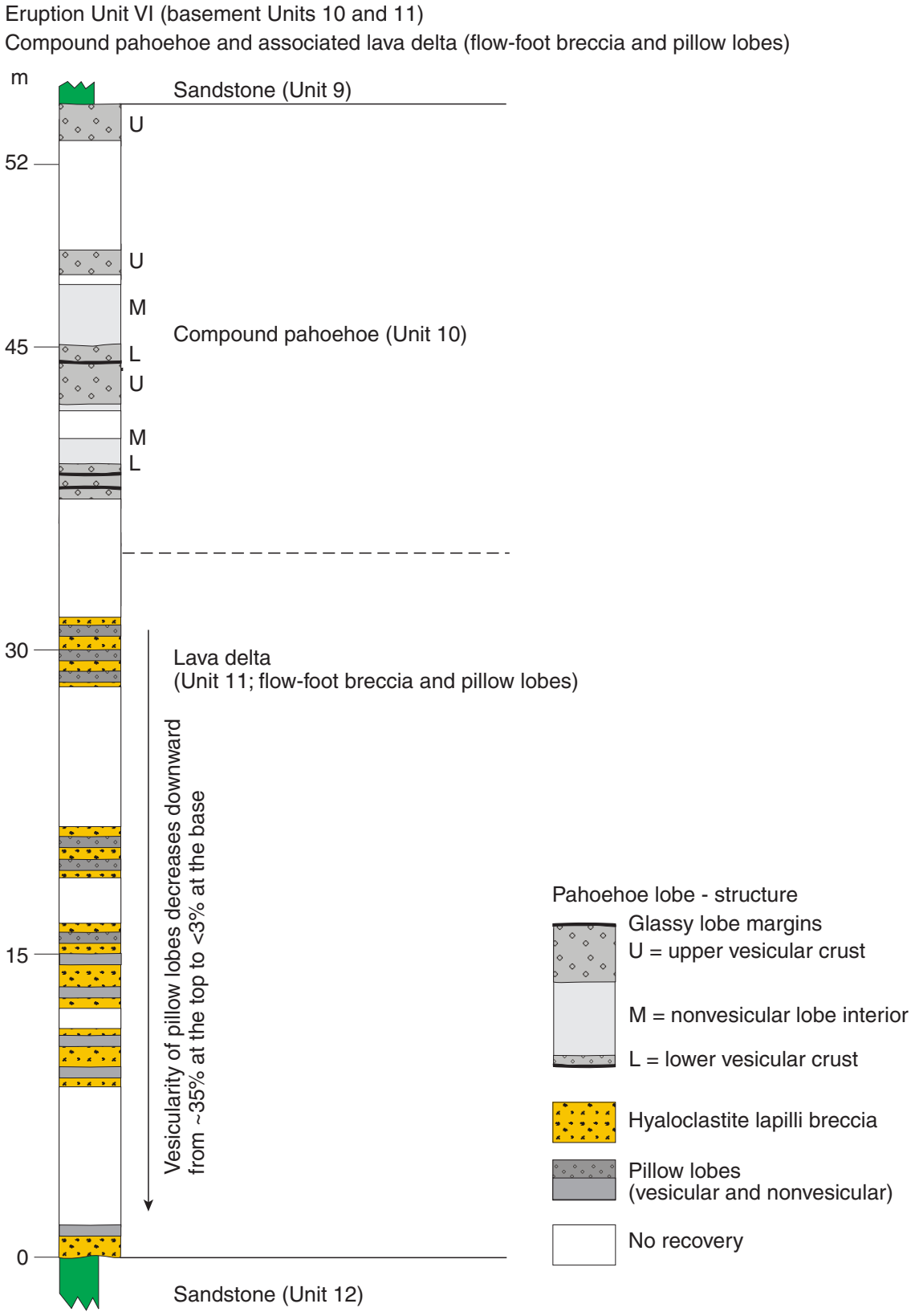

Figure F5. Photograph showing the characteristic clast morphologies in the hyaloclastite lapilli breccia (interval 197-1206A-26R-2, 74–88 cm).

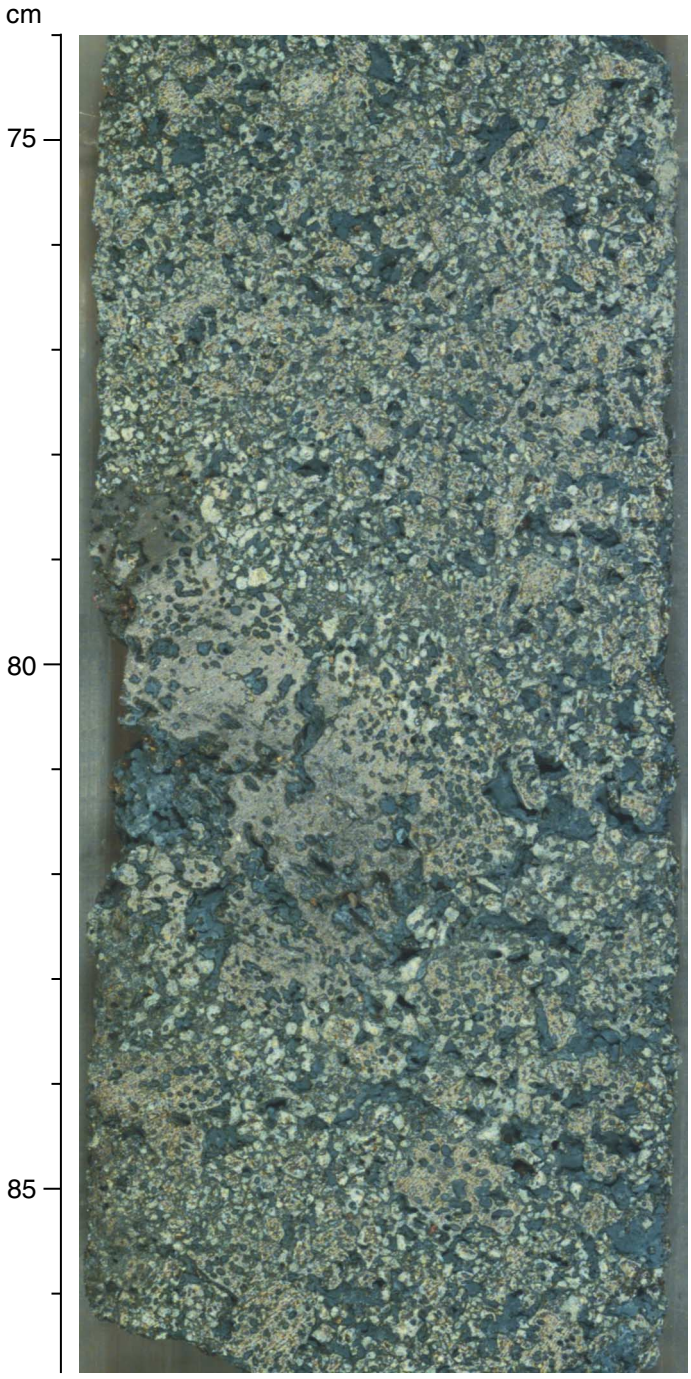

Figure F6. Example of the characteristic internal architecture and hypothetical velocity profile of a'a lava (Unit 21) at Site 1206.

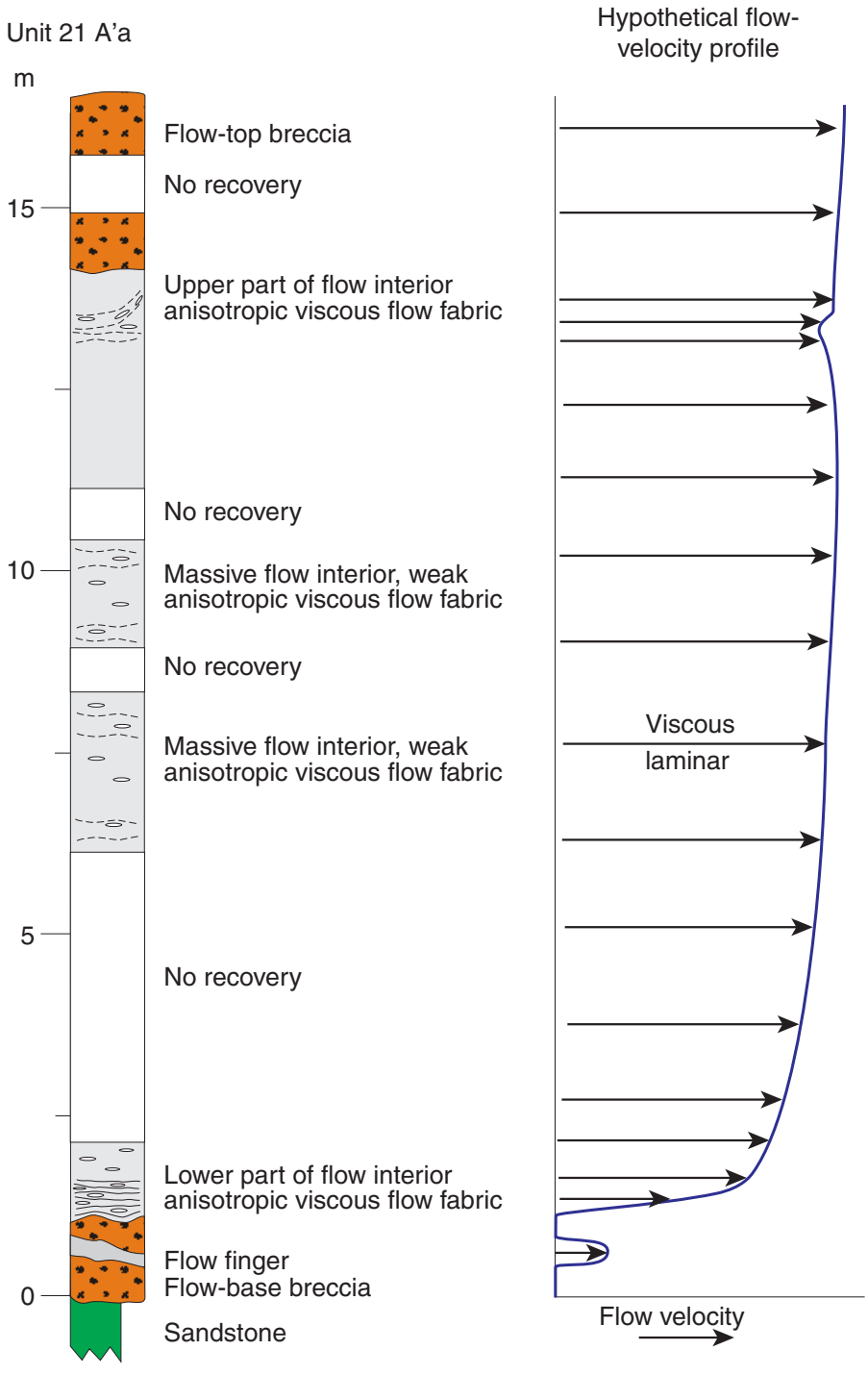

Figure F7. Photograph of lava flowing into the sea during the 1963–1967 Surtsey eruption in Iceland (photograph by Sigurdur Thorarinsson).

Figure F8. Schematic illustration depicting the main features of the lava emplacement environment at Site 1206 (not to scale).

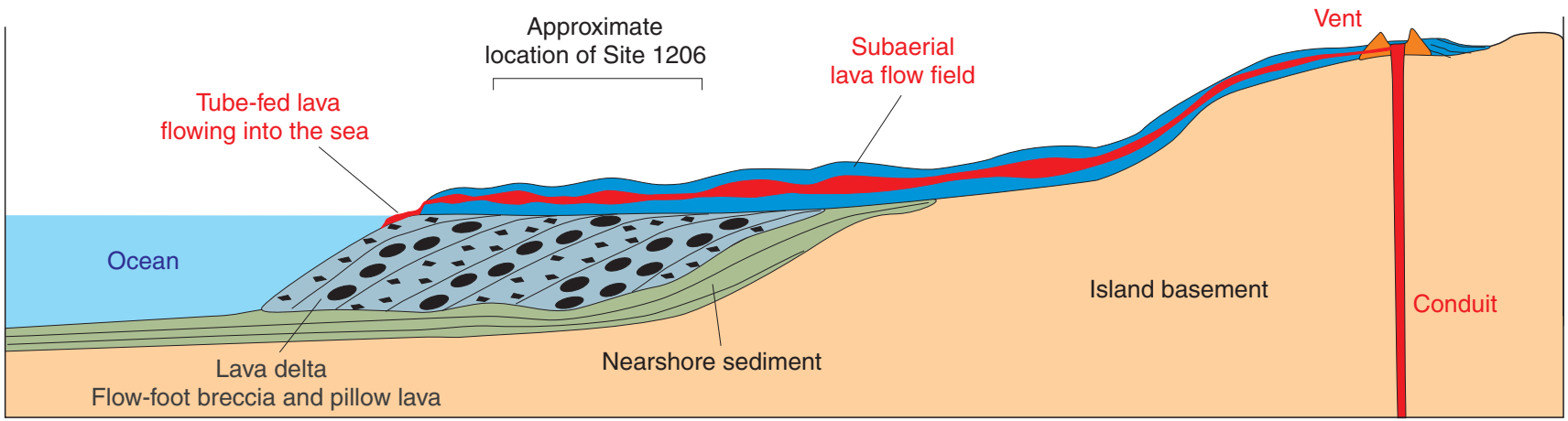

Figure F9. Photomicrograph of euhedral olivine altered to iddingsite in Unit 4 (Sample **197-1206A-8R-2 [Piece 1, 2–3 cm]**) (plane-polarized light; field of view = 0.625 mm; photomicrograph 1206A-317).

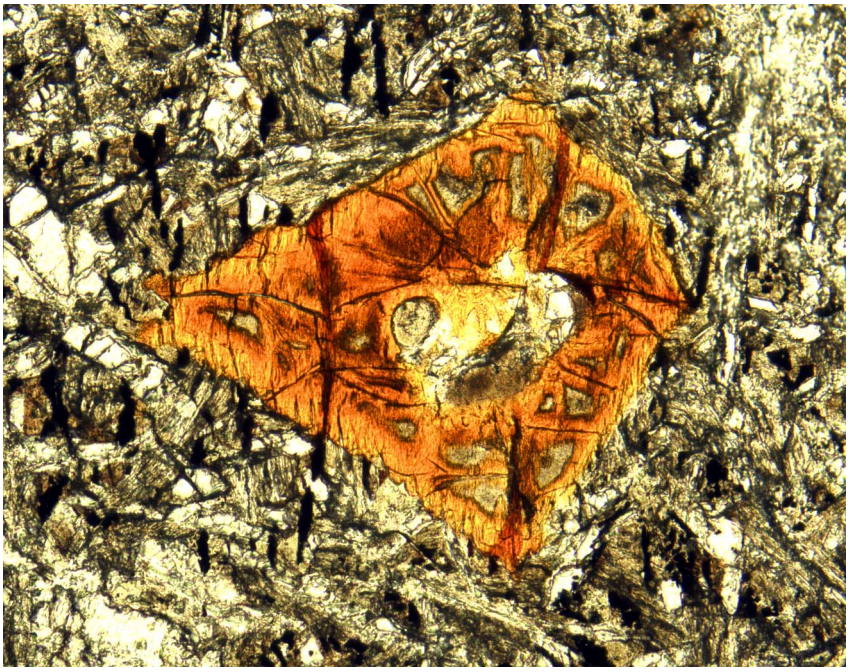

Figure F10. Photomicrograph of olivine partially altered to talc in Unit 1 (Sample **197-1206A-4R-3 [Piece 4A, 72–74 cm]**) (cross-polarized light; field of view = 5 mm; photomicrograph 1206A-301).

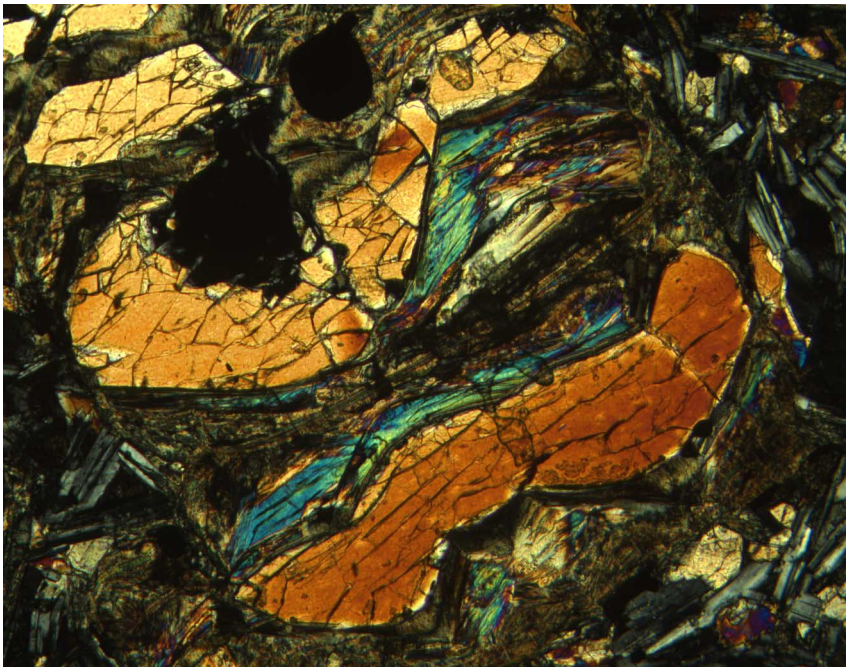

Figure F11. Photomicrograph of olivine partially altered to talc in Unit 1 (Sample **197-1206A-4R-3 [Piece 4A, 72–74 cm**) (plane-polarized light; field of view = 5 mm; photomicrograph 1206A-302).

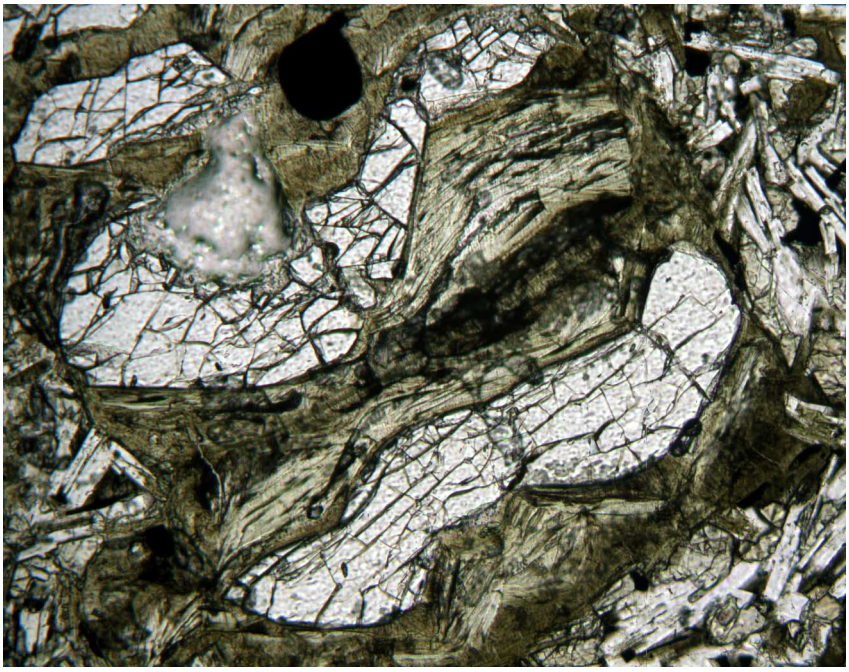

Figure F12. Photomicrograph of olivine altered to iddingsite in Unit 6 (Sample **197-1206A-16R-4 [Piece 8B, 80–82 cm]**) (plane-polarized light; field of view = 0.625 mm; photomicrograph 1206A-356).

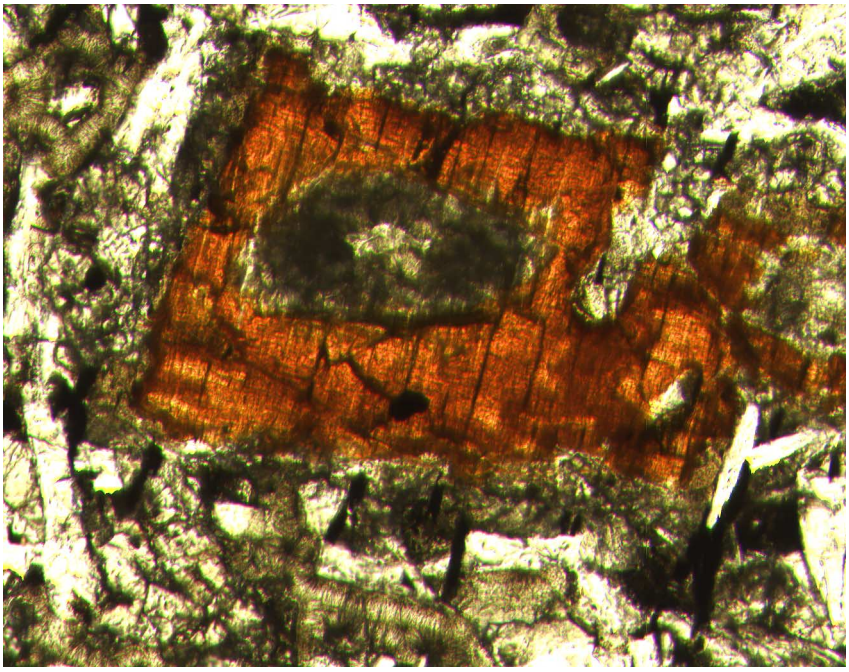

Figure F13. Photomicrograph showing unaltered euhedral olivine in aphanitic groundmass in Unit 6 (Sample **197-1206A-18R-1 [Piece 4, 49–51 cm]**) (cross-polarized light; field of view = 5 mm; photomicrograph 1206A-357).

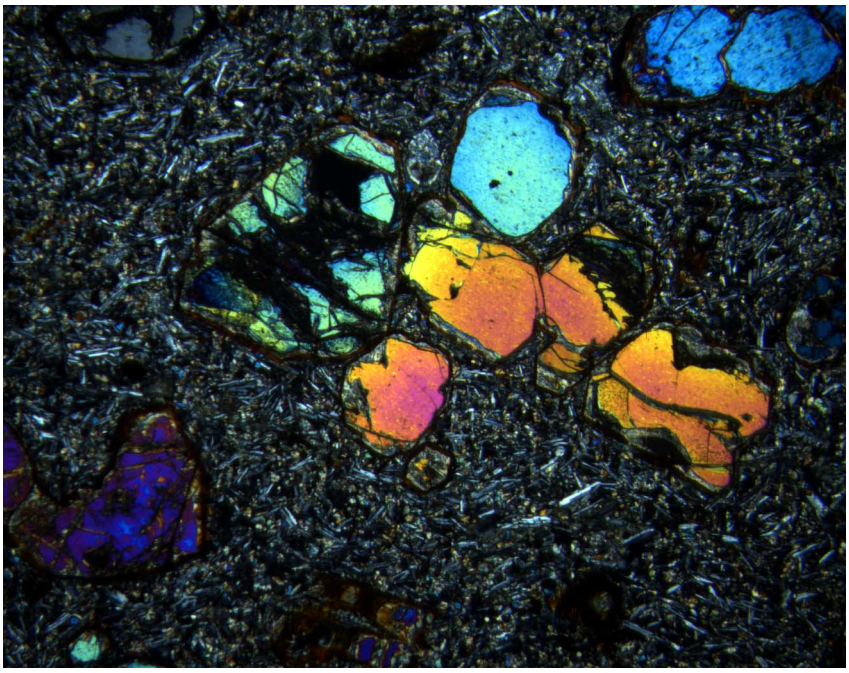

Figure F14. Photomicrograph of euhedral olivine with unaltered interior and rims altered to iddingsite and green clay in Unit 6 (Sample **197-1206A-18R-1 [Piece 4, 49–51 cm]**) (plane-polarized light; field of view = 5 mm; photomicrograph 1206A-358).

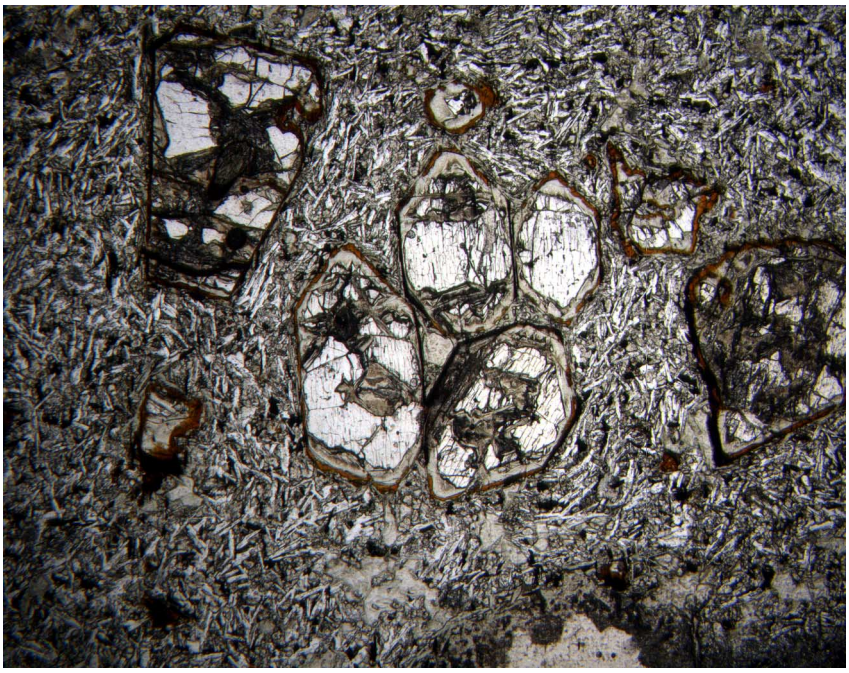

Figure F15. Photomicrograph of euhedral olivine with unaltered interior and rims altered to iddingsite and green clay in Unit 6 (Sample **197-1206A-18R-1 [Piece 4, 49–51 cm]**) (cross-polarized light; field of view = 5 mm; photomicrograph 1206A-359).

Figure F16. Photomicrograph of olivine phenocryst with Cr spinel inclusion in Unit 1 (Sample **197-1206A-4R-3 [Piece 4A, 72–74 cm]**) (cross-polarized light; field of view = 5 mm; photomicrograph 1206A-304).

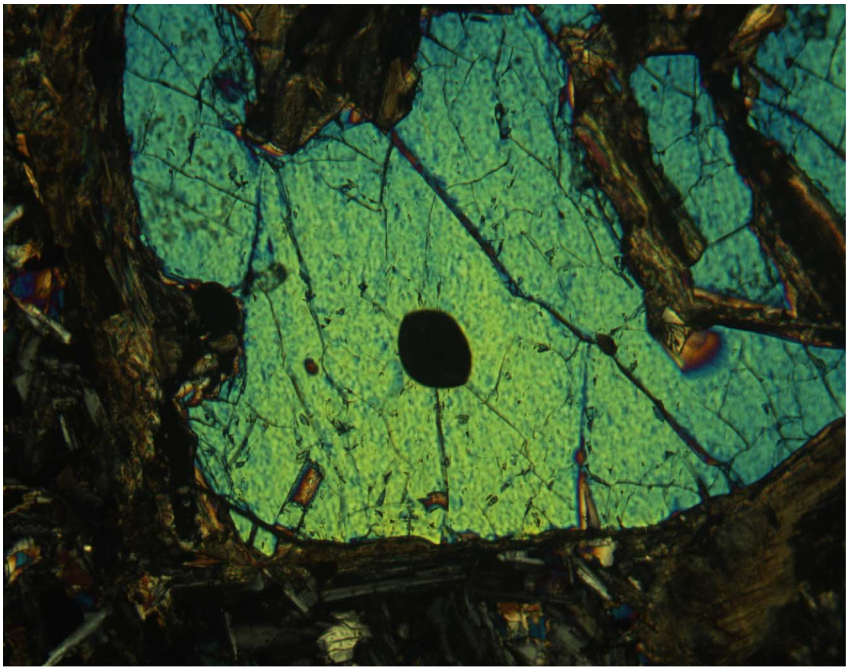

Figure F17. Photomicrograph of olivine phenocryst with Cr spinel inclusions (dark spots) in Unit 1 (Sample 197-1206A-4R-3 [Piece 4A, 72–74 cm]) (cross-polarized light; field of view = 1.25 mm; photomicrograph 1206A-295).

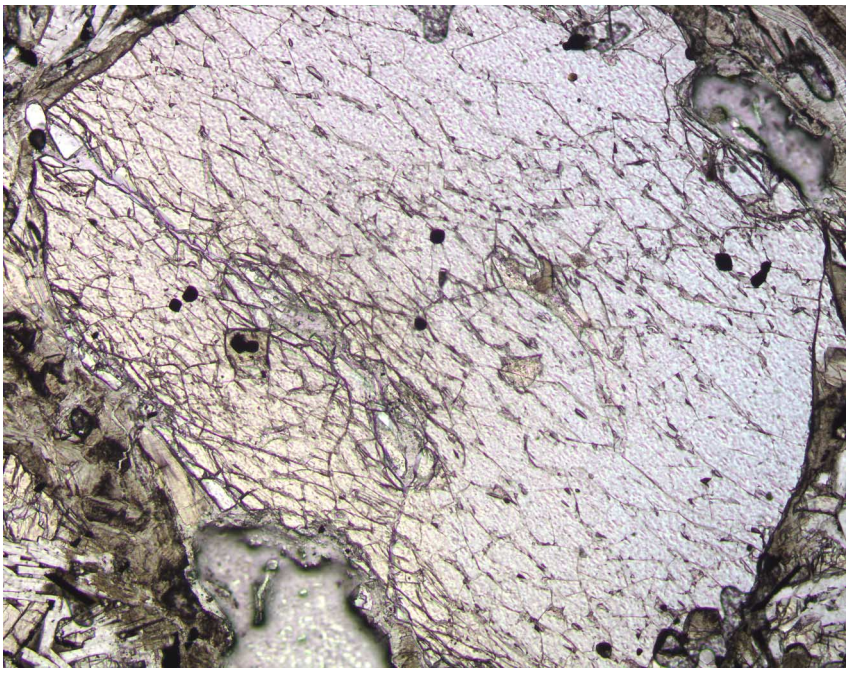

Figure F18. Photomicrograph of anhedral plagioclase showing strongly resorbed margins in Unit 5 (Sample **197-1206A-15R-1 [Piece 7A, 72–74 cm]**) (cross-polarized light; field of view = 0.625 mm; photomicrograph 1206A-311).

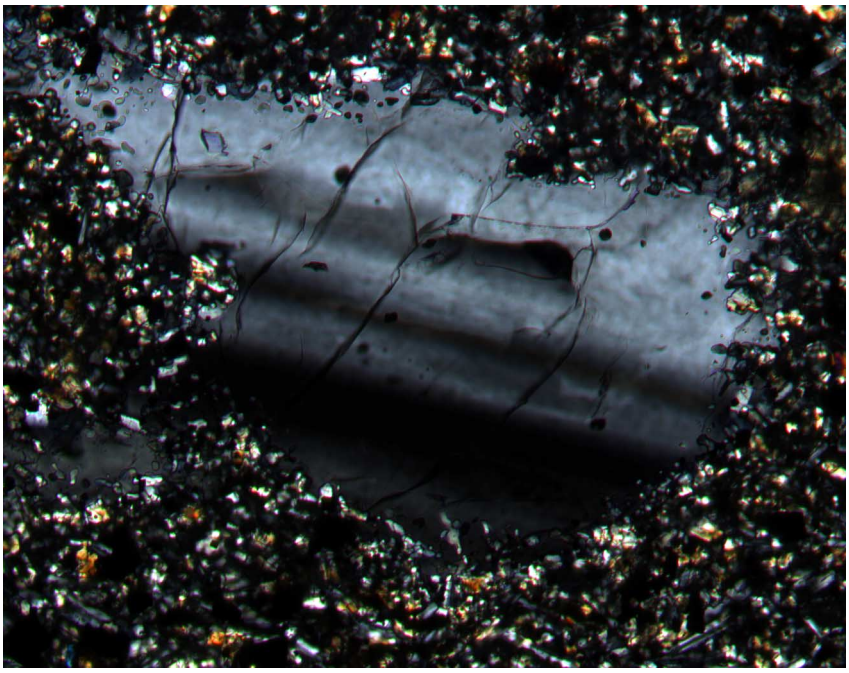

Figure F19. Photomicrograph of plagioclase-clinopyroxene glomerocryst in Unit 5 (Sample **197-1206A-15R-3 [Piece 15, 87–89 cm]**) (cross-polarized light; field of view = 5 mm; photomicrograph 1206A-312).

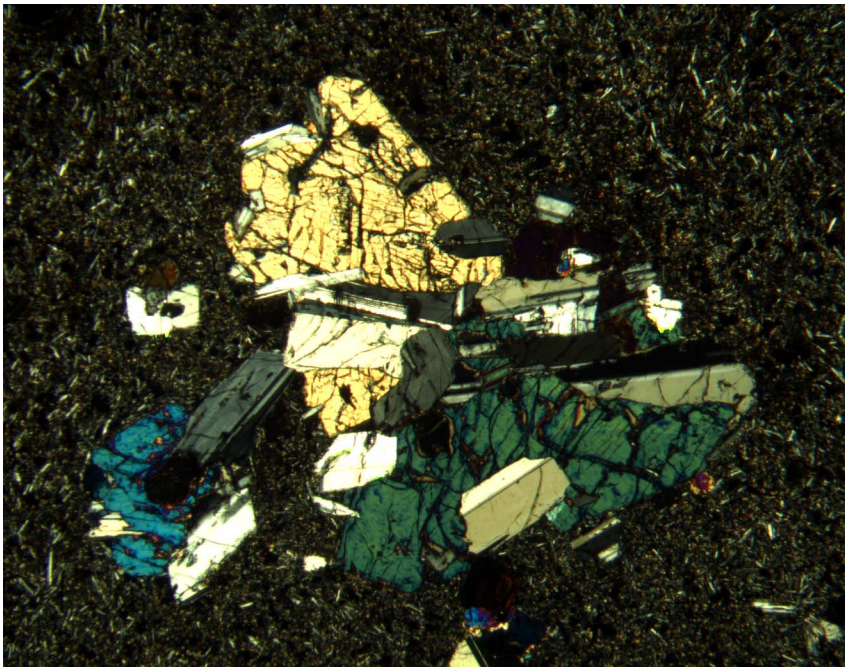

Figure F20. Photomicrograph of olivine-plagioclase-clinopyroxene glomerocryst in Unit 5 (Sample **197-1206A-15R-1 [Piece 7A, 72–74 cm]**) (cross-polarized light; field of view = 1.25 mm; photomicrograph 1206A-313).

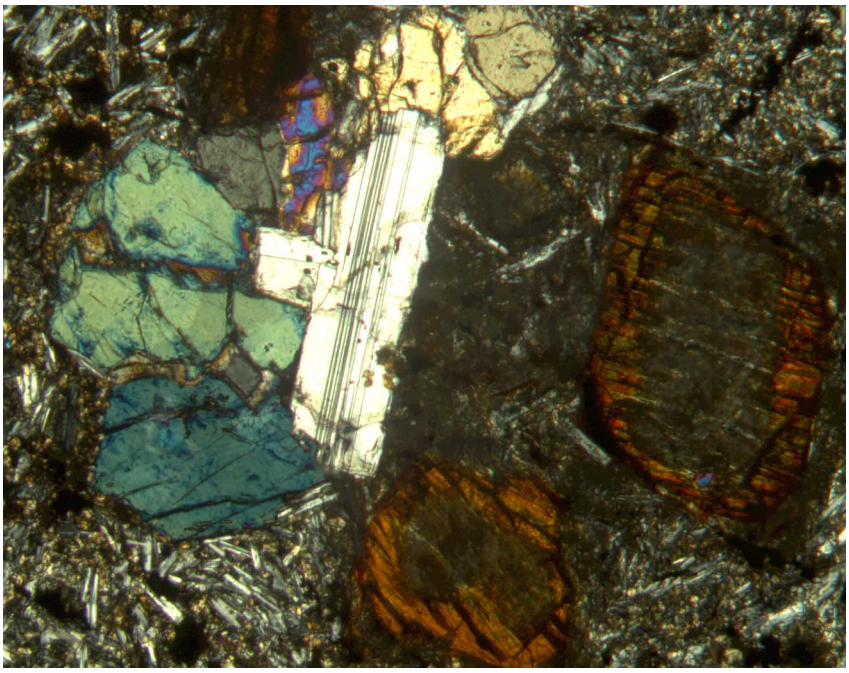

Figure F21. Photomicrograph of plagioclase-clinopyroxene glomerocrysts and olivine phenocryst in aphanitic groundmass in Unit 5 (Sample **197-1206A-15R-1 [Piece 7A, 72–74 cm]**) (cross-polarized light; field of view = 5 mm; photomicrograph 1206A-314).

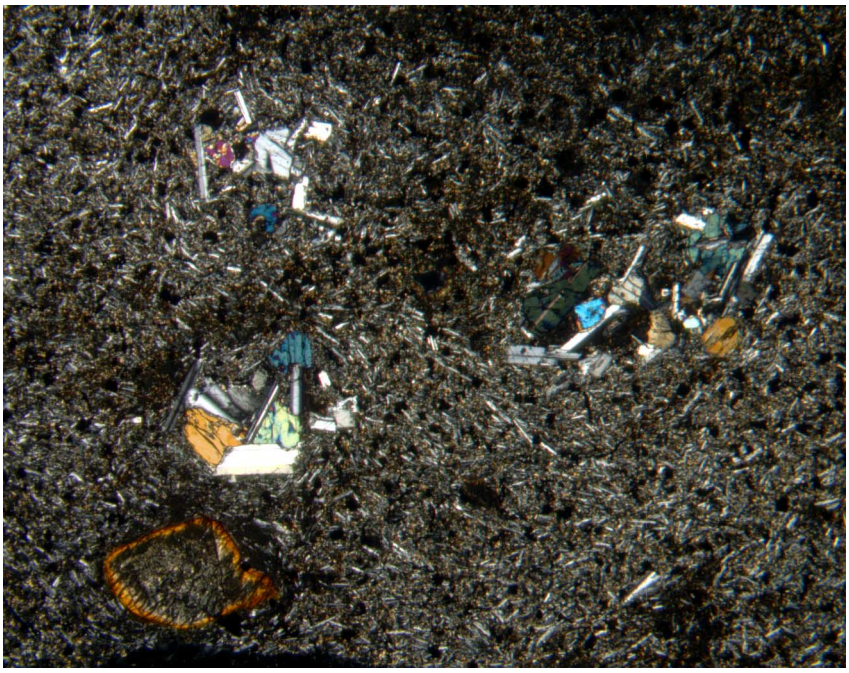

Figure F22. Photomicrograph of Cr spinel phenocryst (large dark spot) adjacent to olivine phenocryst (with Cr spinel inclusion) in Unit 17 (Sample **197-1206A-38R-1 [Piece 2B, 55–58 cm]**) (plane-polarized light; field of view = 1.25 mm; photomicrograph 1206A-349).

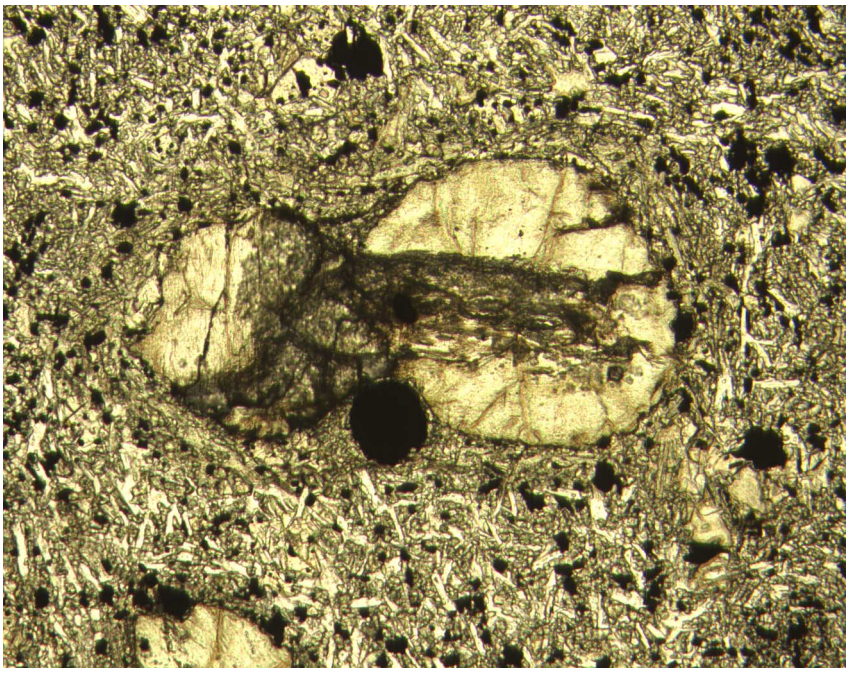

Figure F23. Photomicrograph of titanomagnetite (center) altering to maghemite along cleavage planes in Unit 5 (Sample **197-1206A-15R-3 [Piece 15, 87–89 cm]**) (reflected light; field of view = 0.625 mm; photomicrograph 1206A-322).

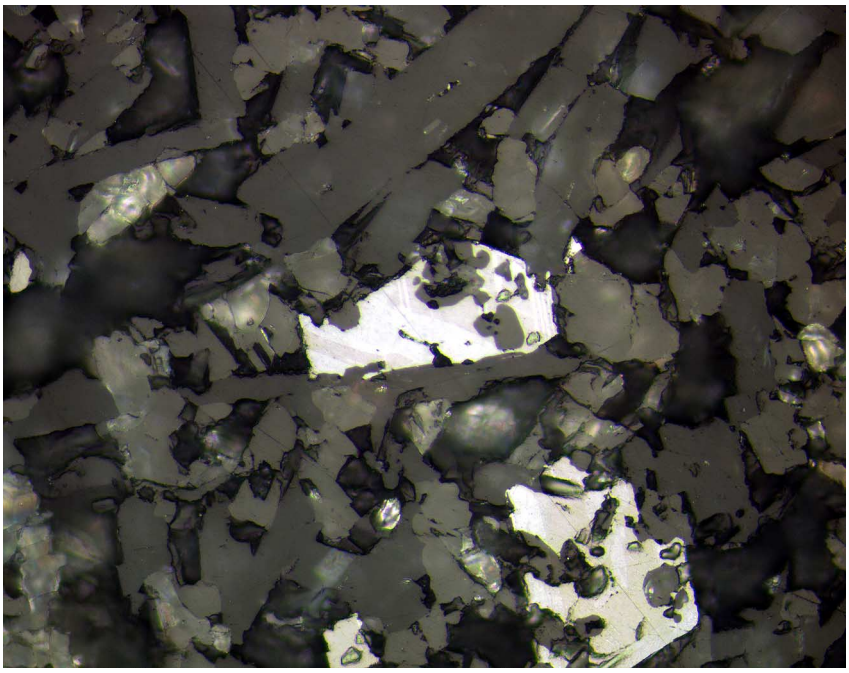

Figure F24. Photomicrograph of altered groundmass olivine (right of center) in Subunit 2c (Sample 197-1206A-7R-1 [Piece 21, 123–125 cm]) (cross-polarized light; field of view = 0.625 mm; photomicrograph 1206A-305).

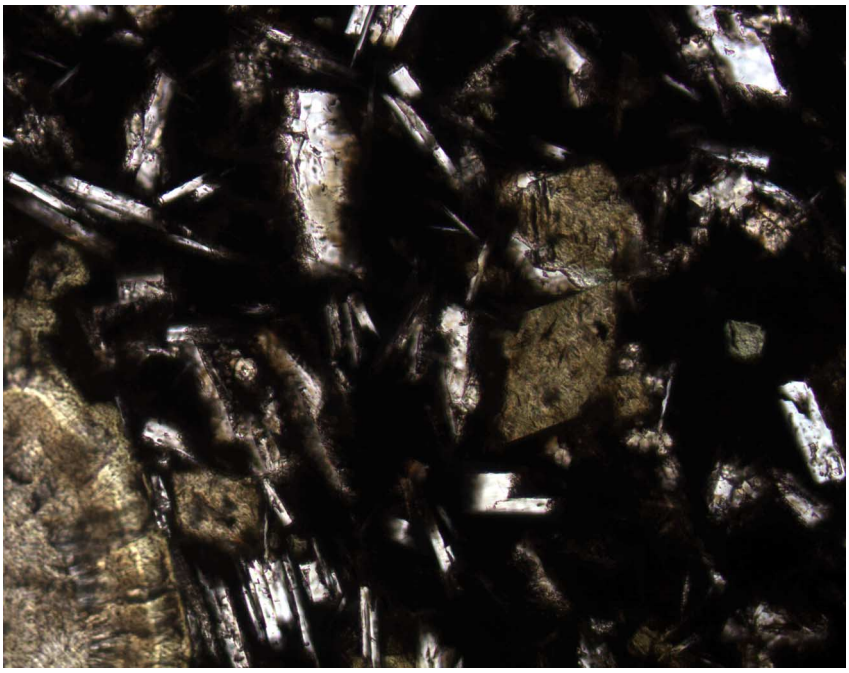

Figure F25. Photomicrograph of segregated material surrounding vesicles in Unit 4 (Sample 197-1206A-8R-1 [Piece 1, 2–3 cm]) (plane-polarized light; field of view = 5 mm; photomicrograph 1206A-316).

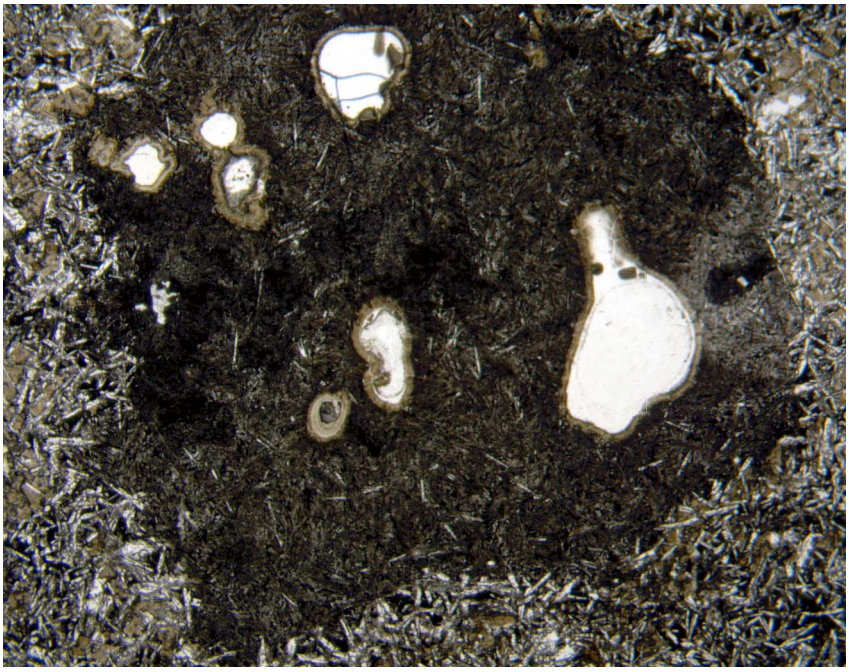

Figure F26. Photomicrographs showing skeletal octahedral and dendritic titanomagnetite morphologies (reflected light; field of view = 1.25 mm). **A.** Sample from Unit 1 with relict Cr spinel (lower, middle) (Sample 197-1206A-3R-2 [Piece 8, 94–96 cm]) (photomicrograph 1206A-291). **B.** Subunit 18b (Sample 197-1206A-41R-1 [Piece 5A, 22–24 cm]) (photomicrograph 1206A-366).

A

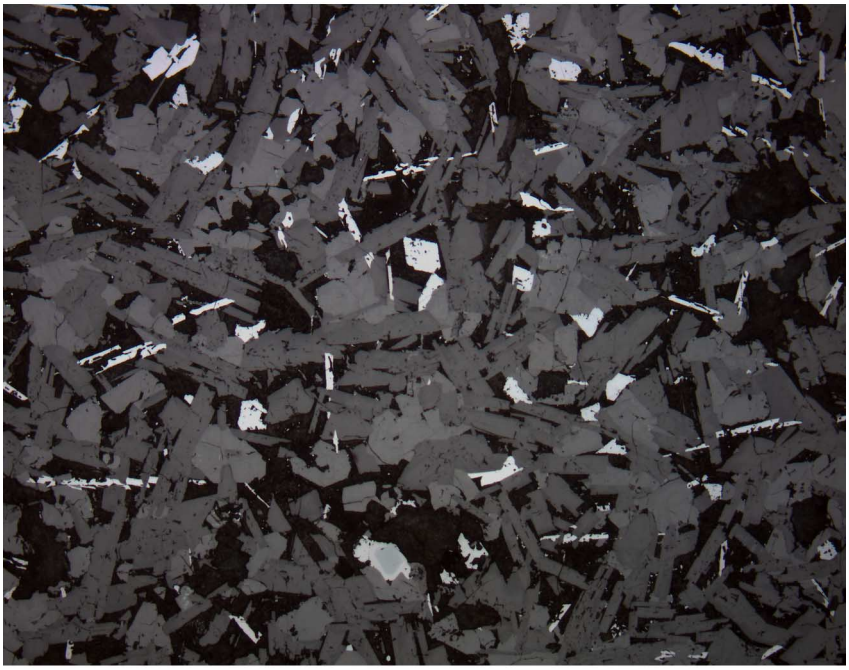

B

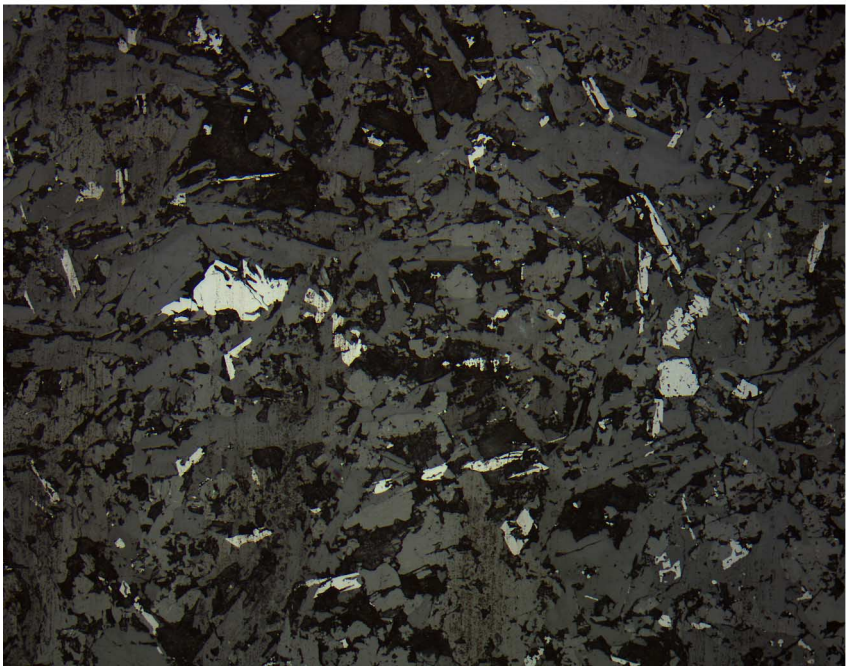

Figure F27. Photomicrographs of skeletal octahedral titanomagnetite morphologies (reflected light; field of view = 0.625 mm). **A.** Ilmenite oxidation lamellae developed in the larger crystals in Unit 5 (Sample 197-1206A-15R-1 [Piece 7A, 72–74 cm]) (photomicrograph 1206A-324). **B.** Unit 21 (Sample 197-1206A-42R-2 [Piece 4, 76–78 cm]) (photomicrograph 1206A-383).

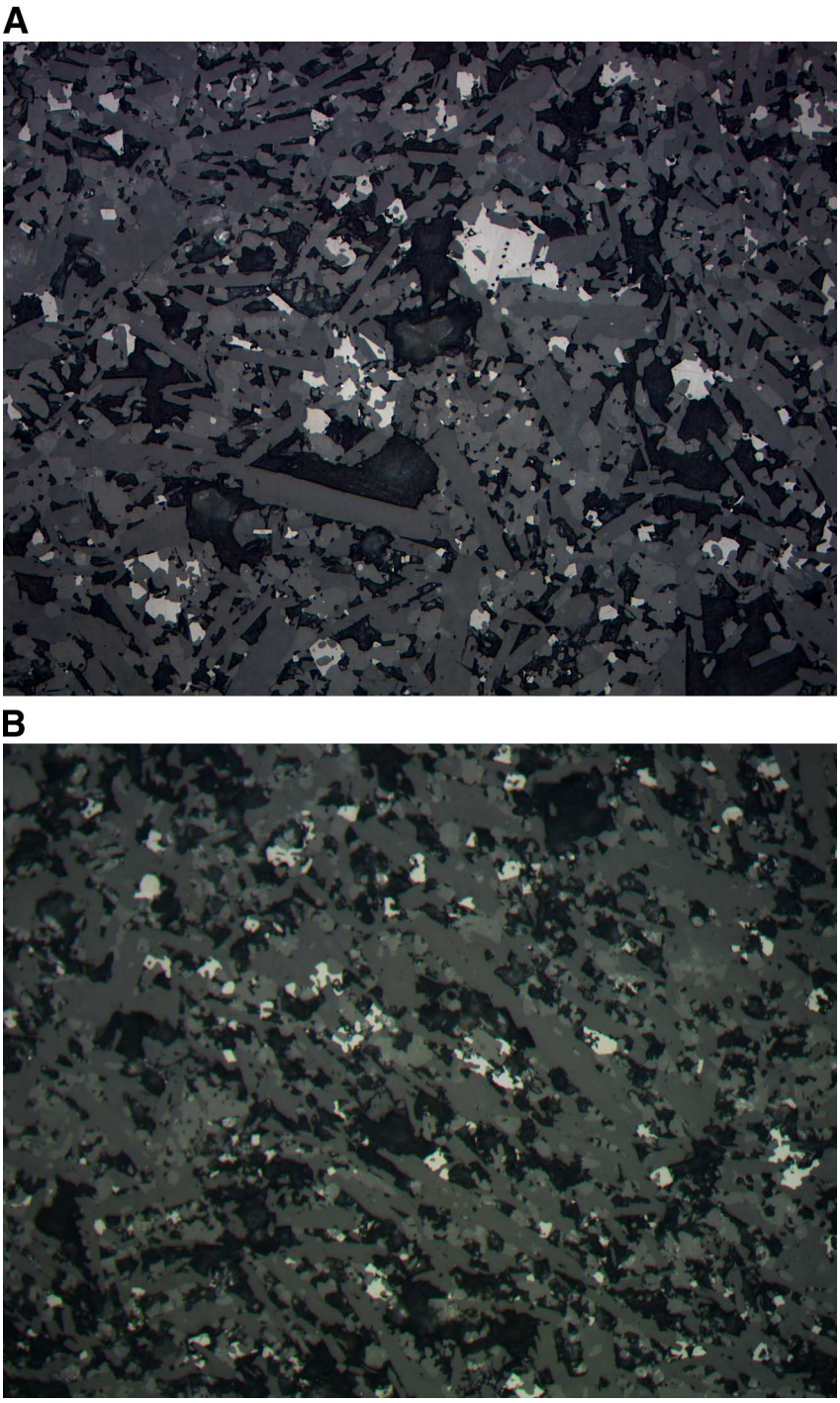

Figure F28. Photomicrographs showing ilmenite oxidation lamellae in titanomagnetite (reflected light; field of view = 0.25 mm). **A.** The triangular crystal contains discontinuous ilmenite oxidation lamellae, whereas the hexagonal form has maghemite developed along cleavage planes in Unit 1 (Sample **197-1206A-3R-2 [Piece 8, 94–96 cm]**) (photomicrograph 1206A-290). **B.** Unit 10 (Sample **197-1206A-24R-3 [Piece 2, 10–12 cm]**) (photomicrograph 1206-336).

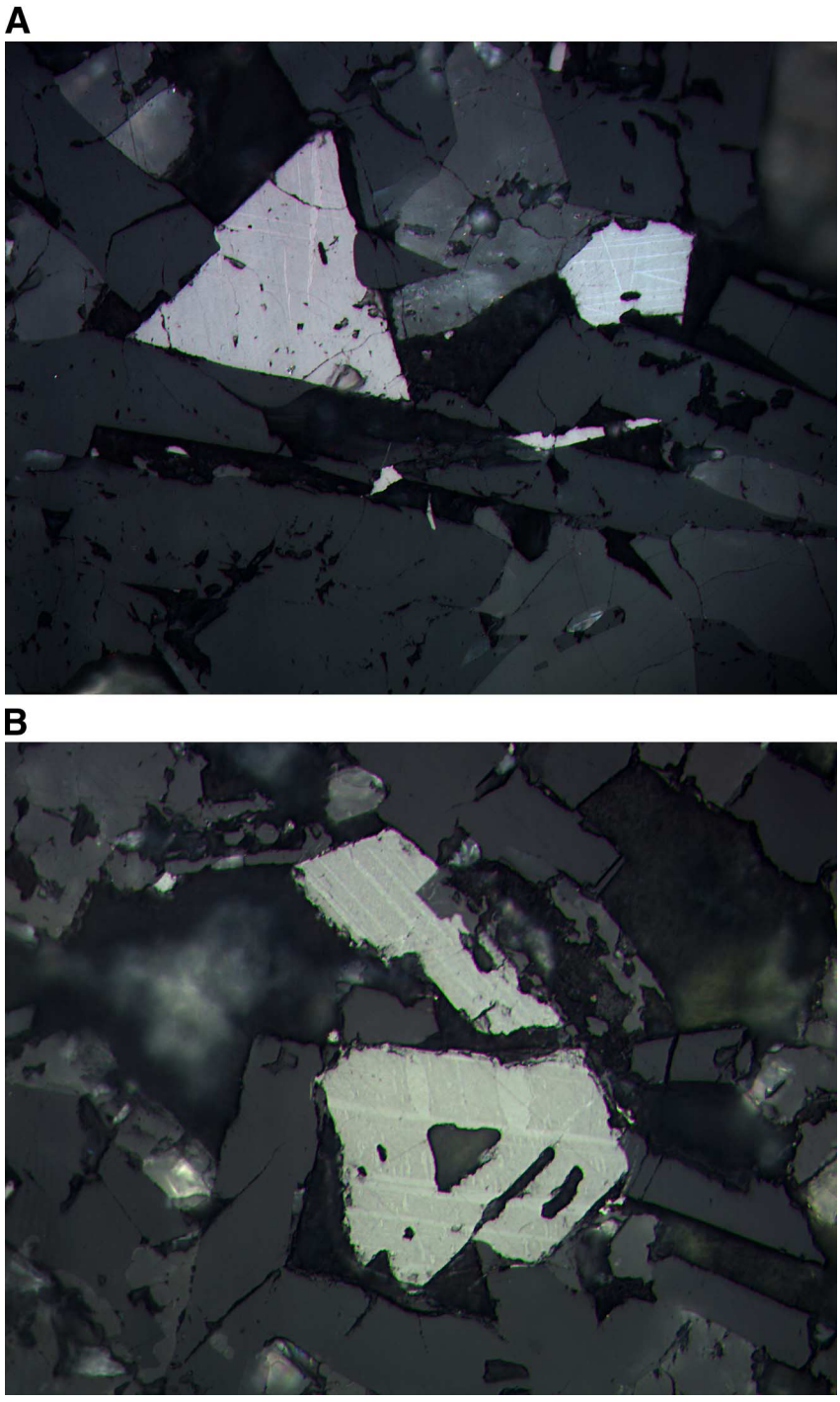

Figure F29. Photomicrographs showing the development of maghemite along cleavage planes and fractures (see also Fig. F28A, p. 55) (reflected light; field of view = 0.25 mm). **A.** Unit 10 (Sample 197-1206A-24R-3 [Piece 2, 10–12 cm]) (photomicrograph 1206A-335). **B.** Unit 5 (Sample 197-1206A-15R-3 [Piece 15, 87–89 cm]) (photomicrograph 1206A-326).

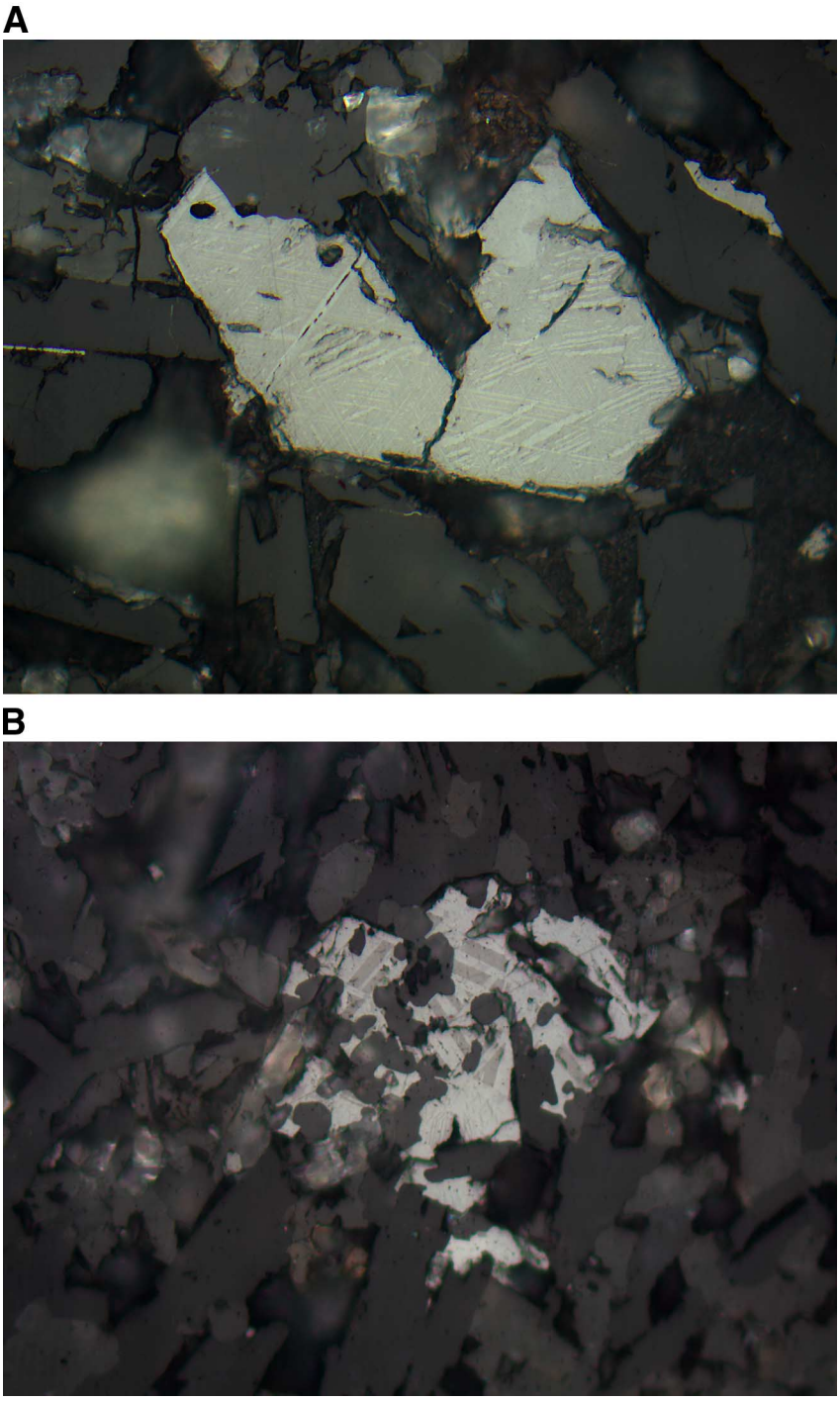

Figure F30. Photomicrographs showing the differential development of maghemite around groundmass titanomagnetite (reflected light). **A.** Unit 6 (Sample **197-1206A-18R-1 [Piece 4, 80–83 cm]**) (field of view = 0.625 mm; photomicrograph 1206A-375). **B.** Unit 5 (Sample **197-1206A-15R-3 [Piece 15, 87–89 cm]**) (field of view = 0.25 mm; photomicrograph 1206A-327).

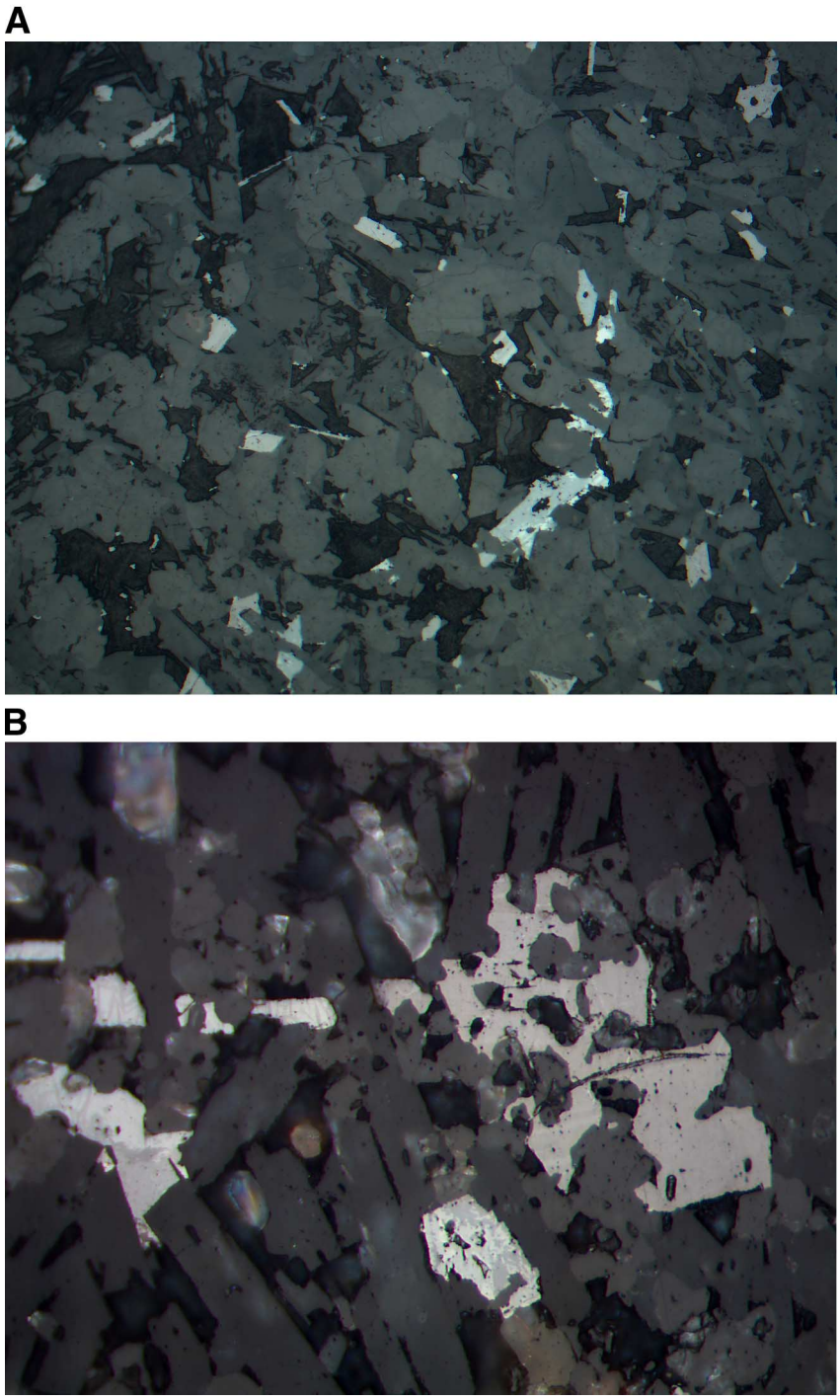

Figure F31. Photomicrographs showing Cr spinel inclusions (dark spots) in unaltered olivine phenocrysts in Unit 1 (Sample 197-1206A-4R-3 [Piece 4A, 72–74 cm]) (field of view = 1.25 mm). **A.** Plane-polarized light; photomicrograph 1206A-295. **B.** Reflected light; photomicrograph 1206A-296.

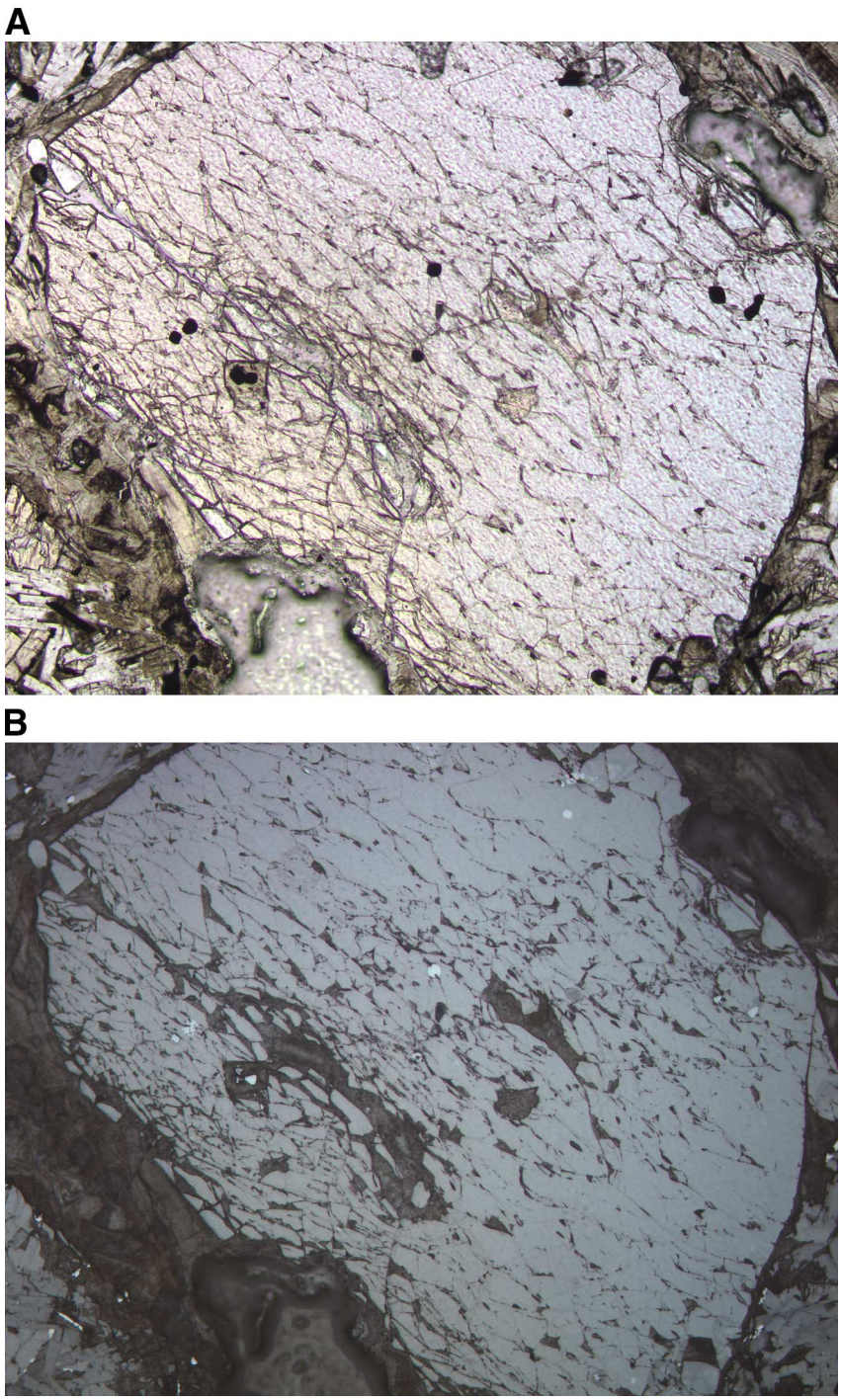

Figure F32. Photomicrographs showing Cr spinel inclusions in altered olivine phenocrysts compared to groundmass titanomagnetite (reflected light). **A.** Unit 1 (Sample **197-1206A-3R-2 [Piece 8, 94–96 cm]**) (field of view = 0.25 mm; photomicrograph 1206A-292). **B.** Subunit 18b (Sample **197-1206A-41R-1 [Piece 5A, 22–24 cm]**) (field of view = 0.625 mm; photomicrograph 1206A-365).

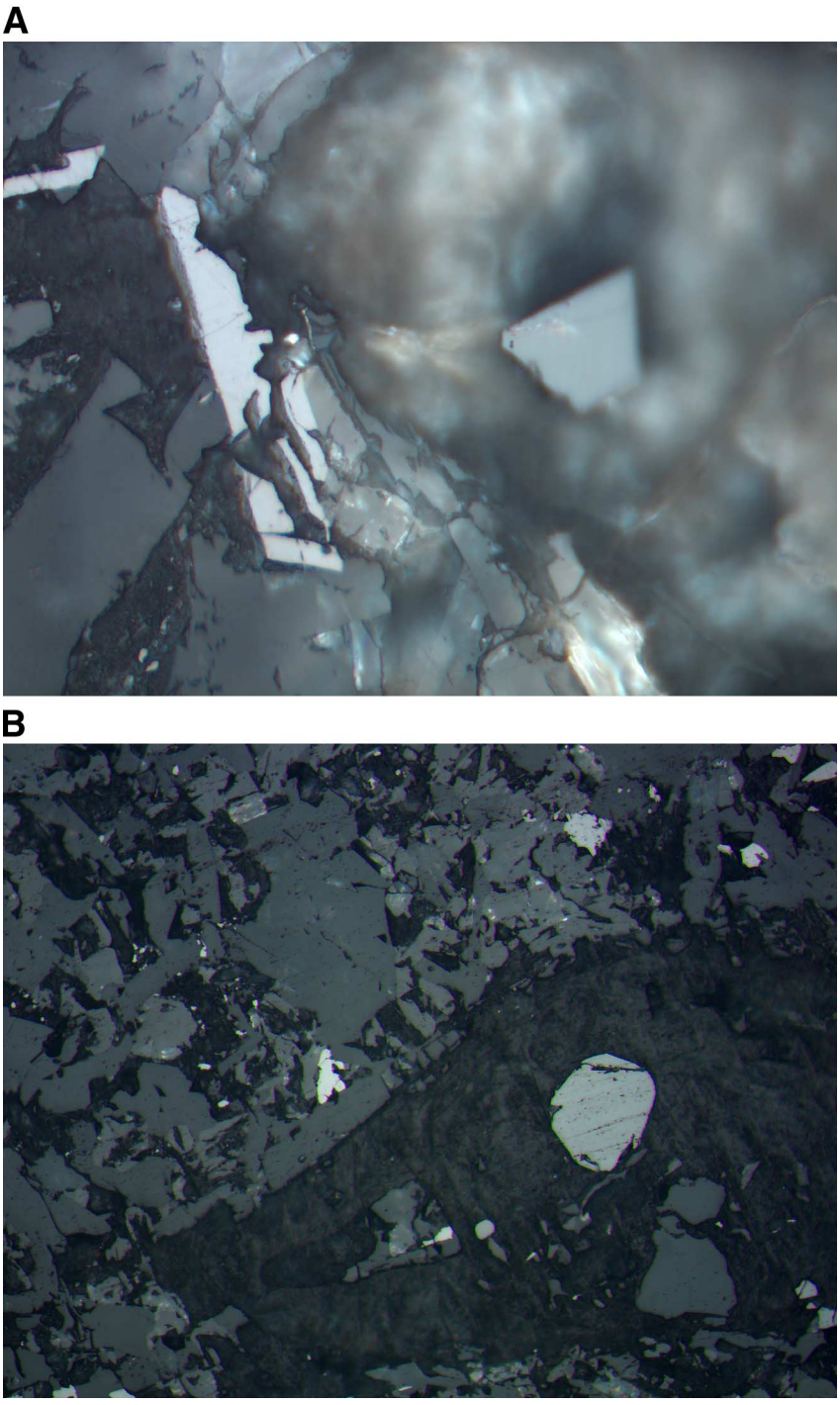

Figure F33. Photomicrographs of Cr spinel inclusions (light spots) in a partially altered olivine phenocryst in Unit 1 (Sample 197-1206A-4R-3 [Piece 4A, 72–74 cm]) (reflected light). **A.** The largest Cr spinel (center right) has no titanomagnetite overgrowths, unlike the smaller crystals in this olivine (field of view = 1.25 mm; photomicrograph 1206A-293). **B.** Close-up of the left side of A, where four Cr spinel inclusions have partially or totally been replaced by titanomagnetite (light gray) (field of view = 0.25 mm; photomicrograph 1206A-294).

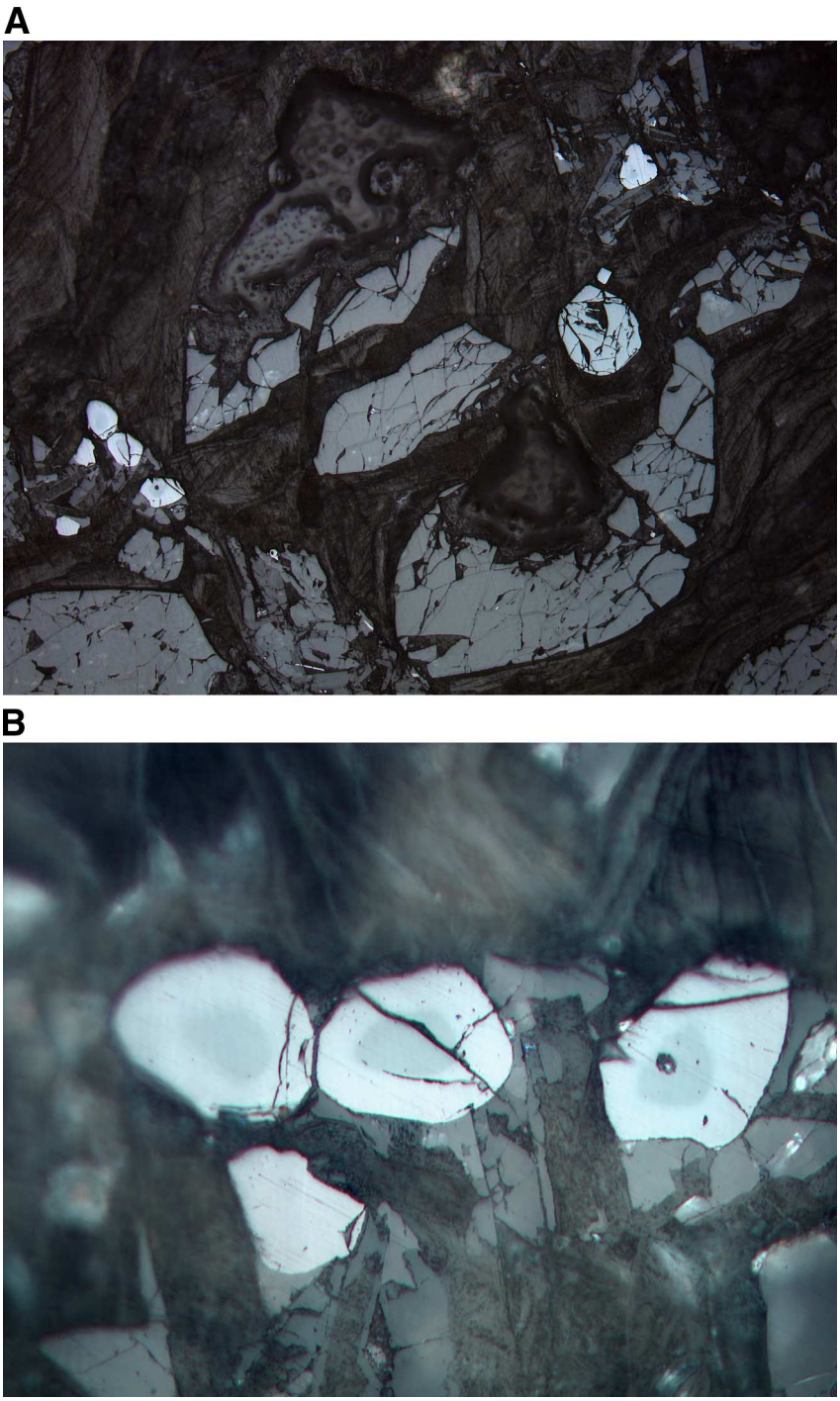

Figure F34. Photomicrographs of a discrete Cr spinel phenocryst in Unit 6 (Sample 197-1206A-18R-1 [Piece 4, 80–83 cm]) (reflected light). **A.** Euhedral morphology of the discrete Cr spinel phenocrysts (field of view = 1.25 mm; photomicrograph 1206A-379). **B.** Close-up of the view shown in A to emphasize the titanomagnetite overgrowth on the Cr spinel phenocryst, which also contains ilmenite oxidation lamellae (i.e., extreme right of the picture) (field of view = 0.625 mm; photomicrograph 1206A-380).

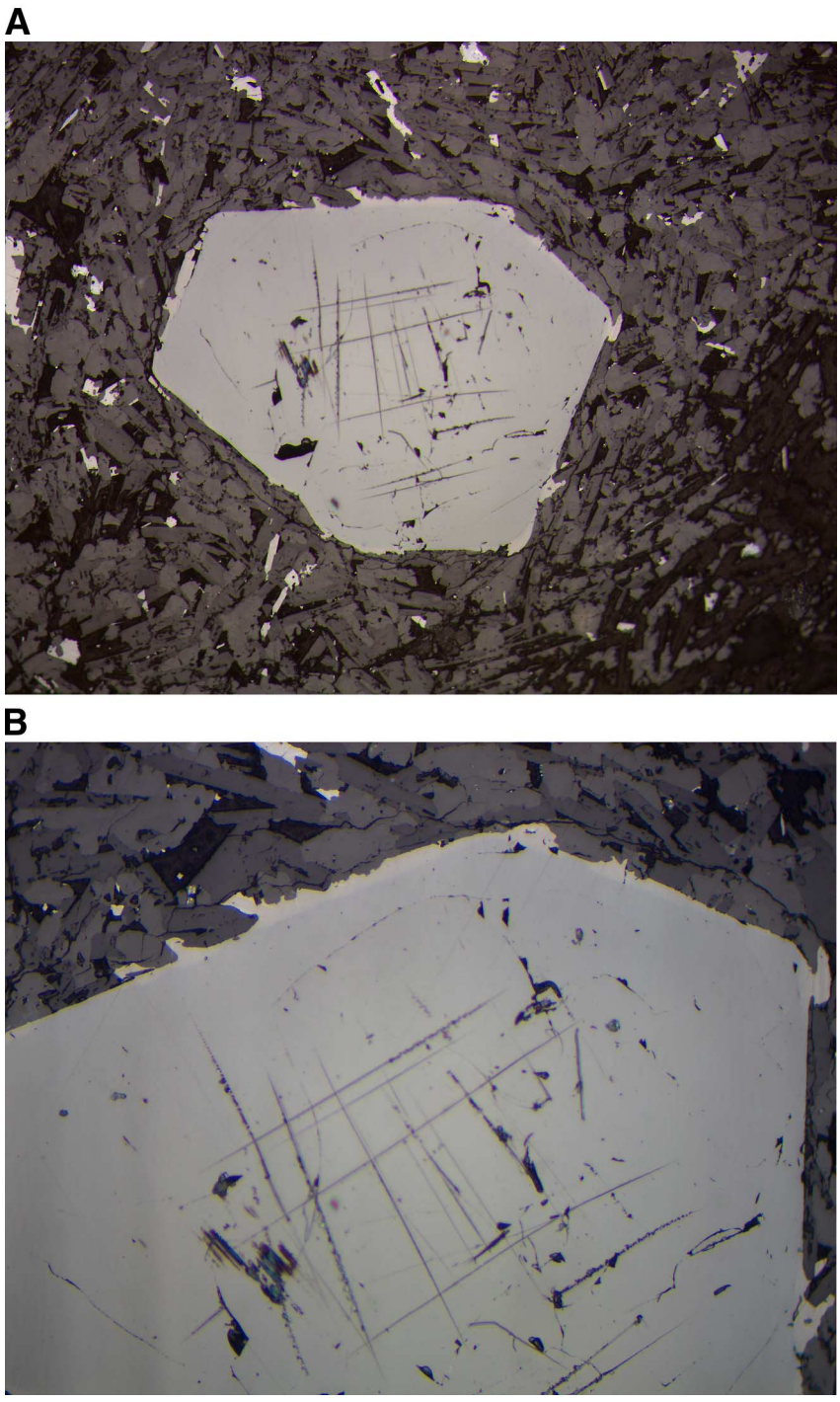

Figure F35. Photomicrographs showing the titanomagnetite overgrowths on Cr spinel crystals from Unit 6 with ilmenite oxidation lamellae and maghemite development along fractures and cleavage planes (reflected light). **A.** Sample **197-1206A-18R-1 (Piece 4, 49–51 cm)** (field of view = 0.25 mm; photomicrograph 1206A-331). **B.** Sample **197-1206A-18R-1 (Piece 4, 80–83 cm)** (field of view = 0.625 mm; photomicrograph 1206A-378).

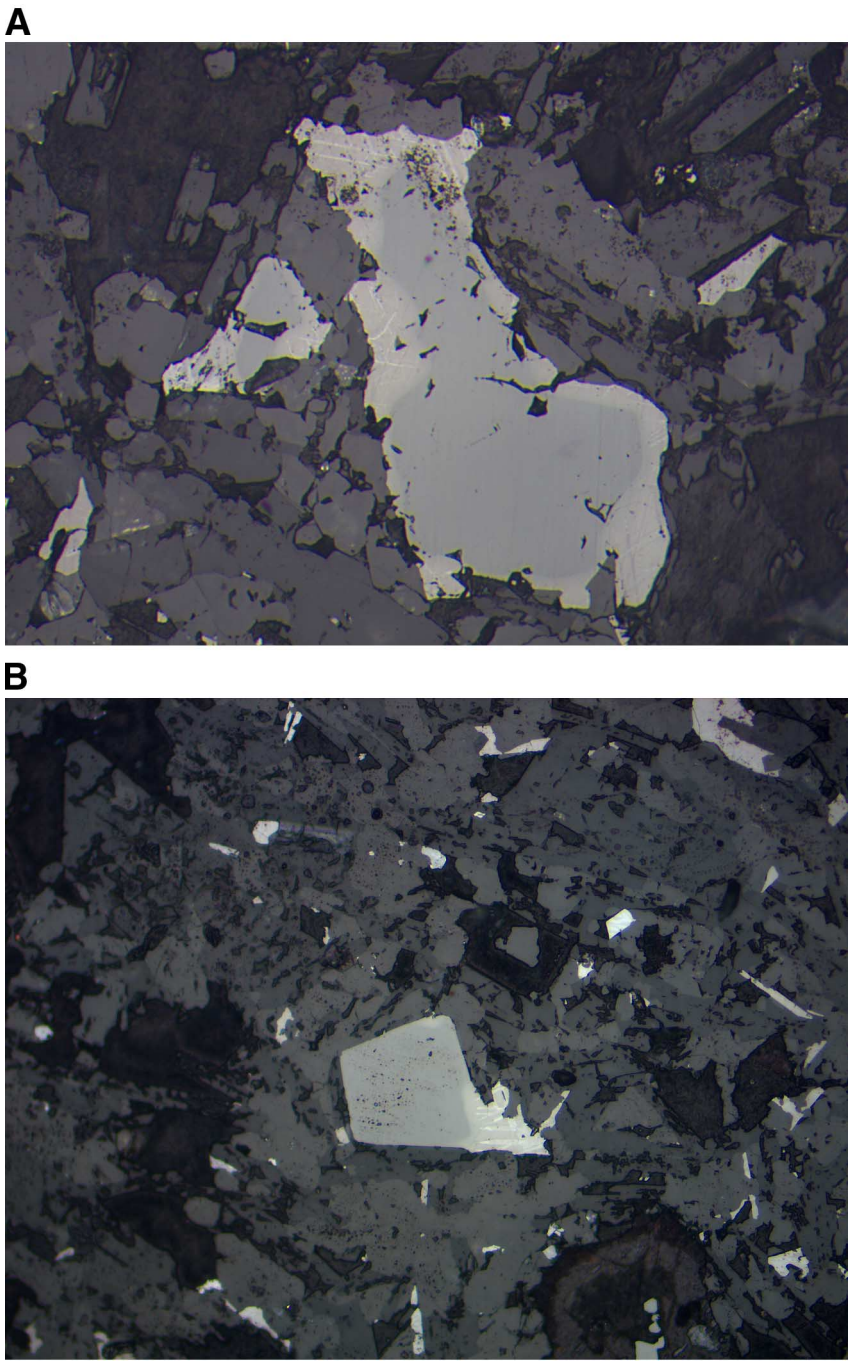

Figure F36. Photomicrographs showing the morphology of olivine phenocrysts and Cr spinel inclusions (plane-polarized light; field of view = 5 mm). **A.** Olivines with an alteration rim of iddingsite but with unaltered centers in Unit 6. Opaque Cr spinel inclusions are present in the phenocryst at the center of the photomicrograph (Sample **197-1206A-18R-1 [Piece 4, 49–51 cm]**) (photomicrograph 1206A-328). **B.** Olivine phenocrysts with an alteration rim of serpentine but with unaltered centers in Unit 17. Discrete, round, relict Cr spinel phenocrysts are also present (Sample **197-1206A-38R-1 [Piece 2B, 55–58 cm]**) (photomicrograph 1206A-384).

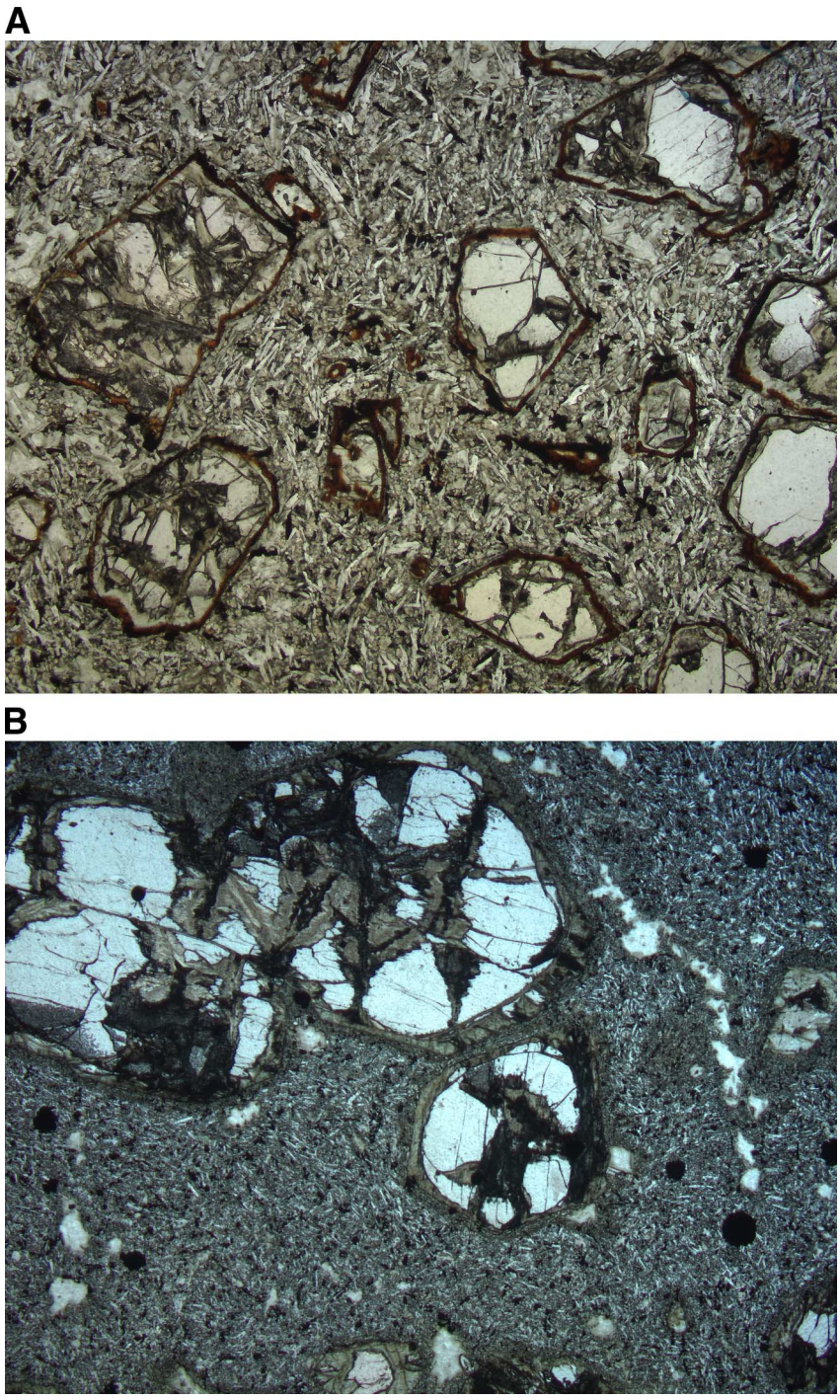

Figure F37. Photomicrographs showing the morphology and composition of the discrete, round Cr spinel phenocrysts of Unit 17 (Sample 197-1206A-38R-1 [Piece 2B, 55–58 cm]) (reflected light; field of view = 0.625 mm). **A.** Extensive development of titanomagnetite on a relict Cr spinel (photomicrograph 1206A-362). **B.** Another example of extensive development of titanomagnetite on a relict Cr spinel (photomicrograph 1206A-362). (Continued on next page.)

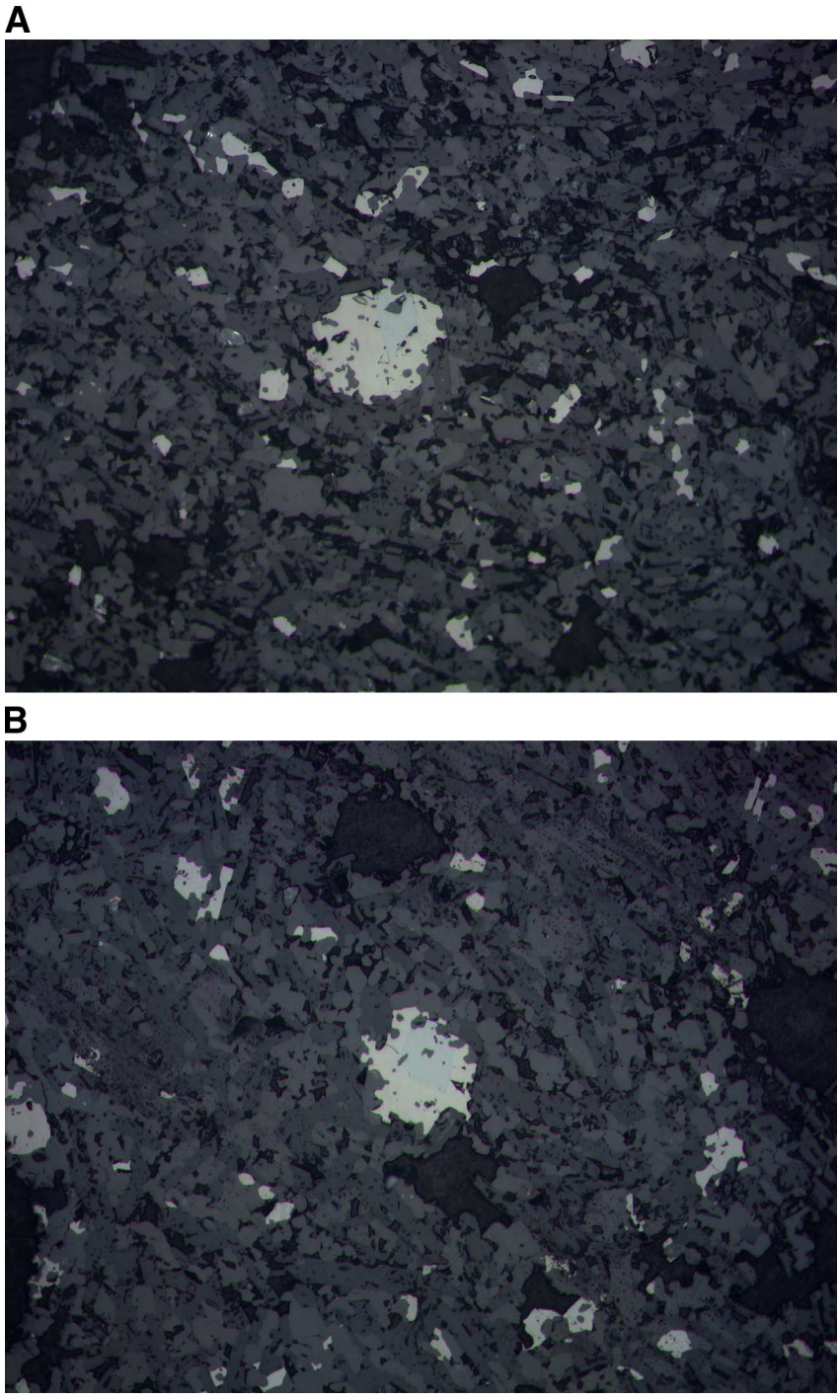

Figure F37 (continued). C, D. Two generations of titanomagnetite. The larger masses have resulted from the complete replacement of discrete Cr spinel phenocrysts by titanomagnetite, which has subsequently developed ilmenite oxidation lamellae. The smaller crystals are typical groundmass titanomagnetite: (C) photomicrographs 1206A-363; (D) photomicrograph 1206A-361.

C

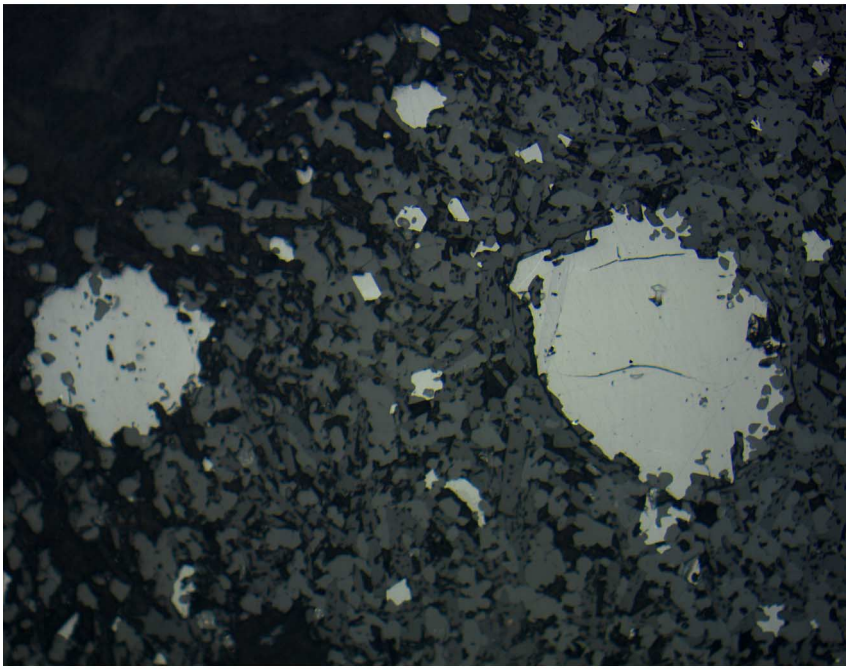

D

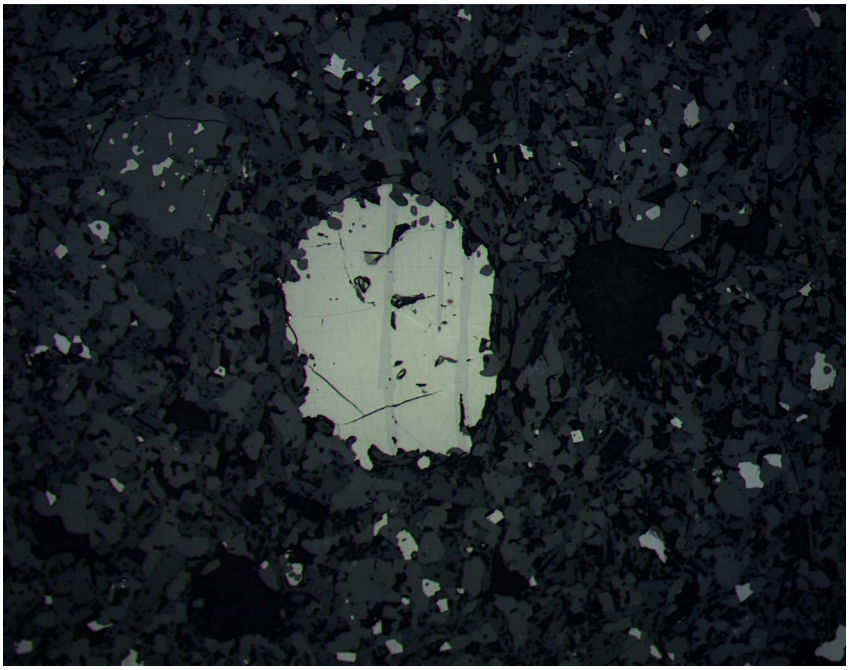

Figure F38. Photomicrograph of titanomagnetite growing around a relict Cr spinel crystal from Unit 5 (Sample **197-1206A-15R-1 [Piece 7A, 72–74 cm]**) (reflected light; field of view = 0.25 mm; photomicrograph 1206A-323).

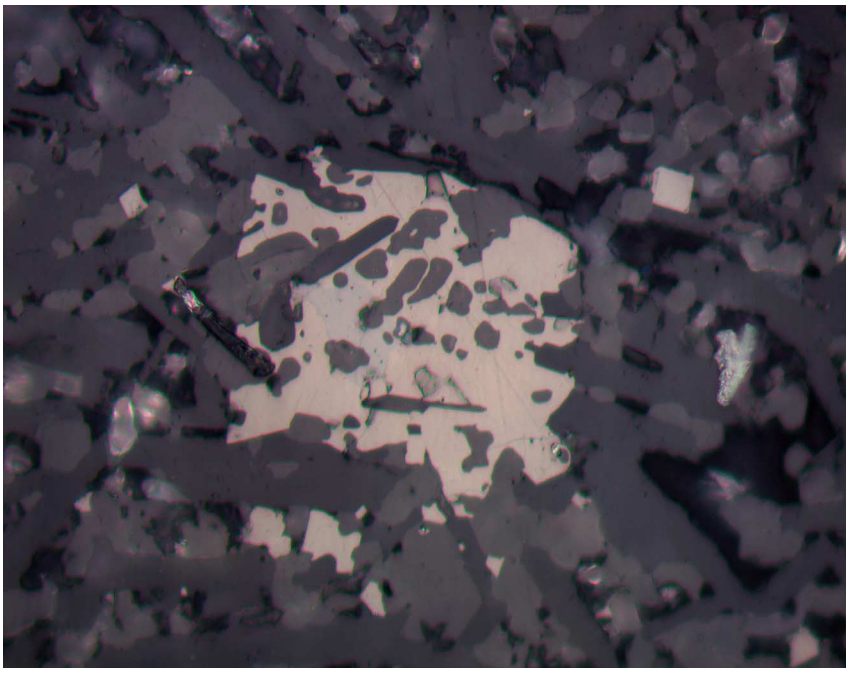

Figure F39. Photomicrographs showing the presence of Cr spinel inclusions (dark equant crystals) in an altered olivine phenocryst with an iddingsite rim in Unit 6 (Sample **197-1206A-16R-5 [Piece 8, 66–67 cm]**) (field of view = 0.625 mm) **A.** Plane-polarized light; photomicrograph 1206A-372. **B.** Reflected light; photomicrograph 1206A-371.

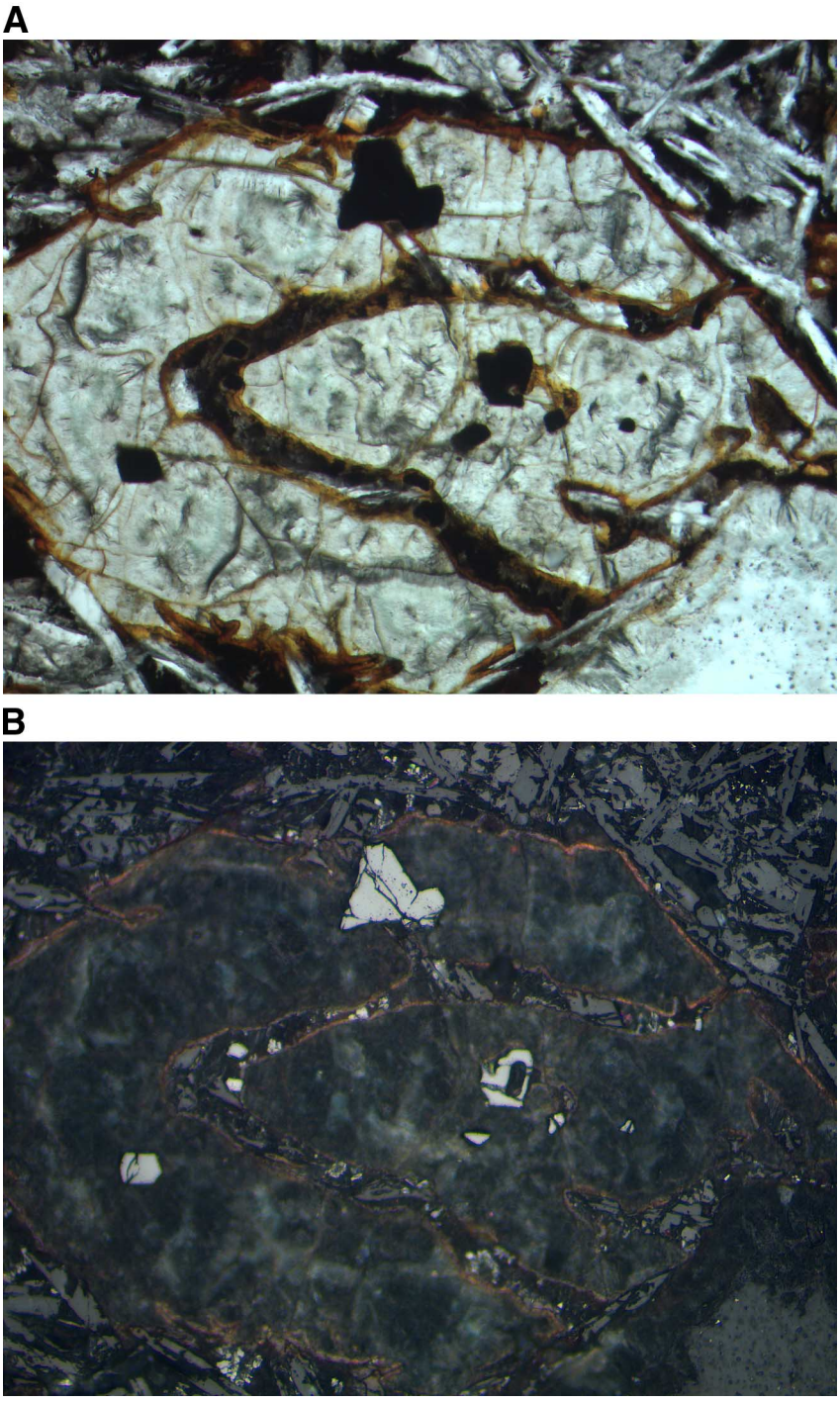

Figure F40. Photomicrograph of a plagioclase-clinopyroxene glomerocryst in Unit 5 containing chromite inclusions (small dark gray inclusions at center right and the diamond-shaped inclusion in the upper left). These do not have the characteristic blue-gray color of Cr spinel (Sample **197-1206A-15R-3 [Piece 15, 87–89 cm]**) (reflected light; field of view = 1.25 mm; photomicrograph 1206A-325).

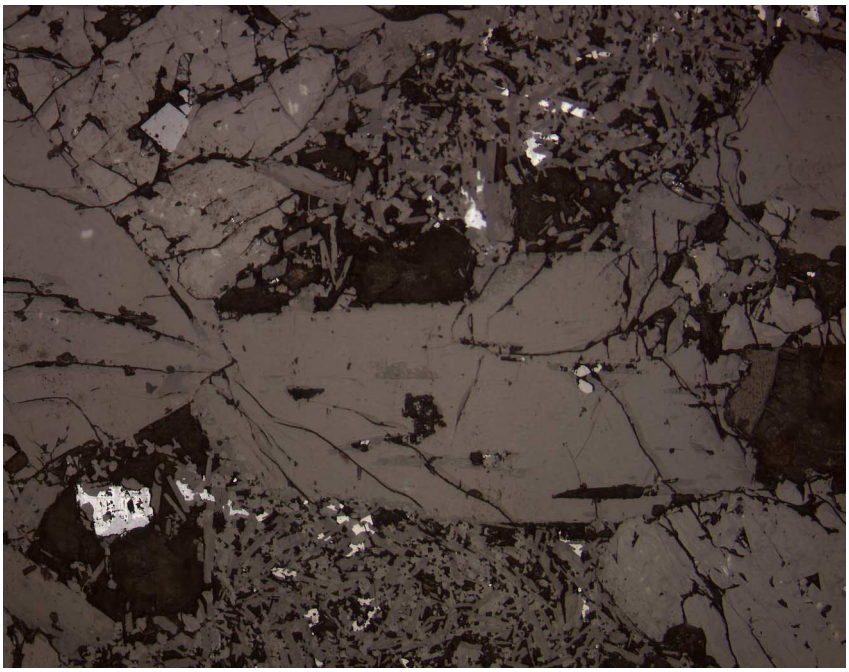

Figure F41. Total alkali content ($Na_2O + K_2O$) vs. SiO_2 classification plot for basaltic lava flows from Koko Seamount. Shown for comparison in this and subsequent figures are data from Nintoku and Suiko Seamounts (for data see **"Physical Volcanology and Igneous Petrology,"** p. 8, in the "Site 1205" chapter) (Jackson et al., 1980; M. Regelous et al., unpubl. data). The solid diagonal line is the alkalic-tholeiitic dividing line for Hawaiian basalt (Macdonald and Katsura, 1964). Only three samples from Site 1206 plot in the alkalic basalt field, a sample from Unit 4 and the samples from Units 8 and 18.

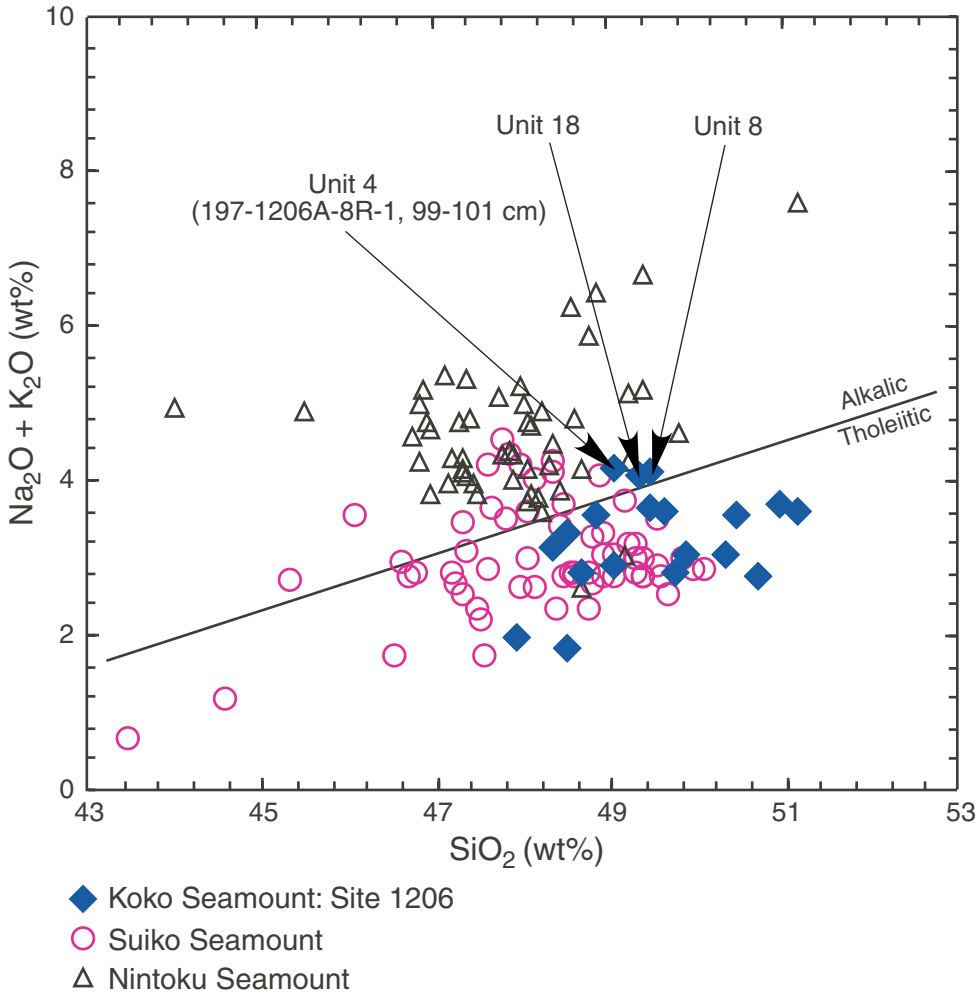

Figure F42. Abundances of Na_2O, K_2O, TiO_2, CaO, Al_2O_3, and Zr vs. MgO content for lavas from Koko, Nintoku, and Suiko Seamounts. All trends show an inverse correlation except for CaO in Nintoku Seamount lavas with <5 wt% MgO. Note that some lavas from Suiko Seamount contain up to 30 wt% MgO.

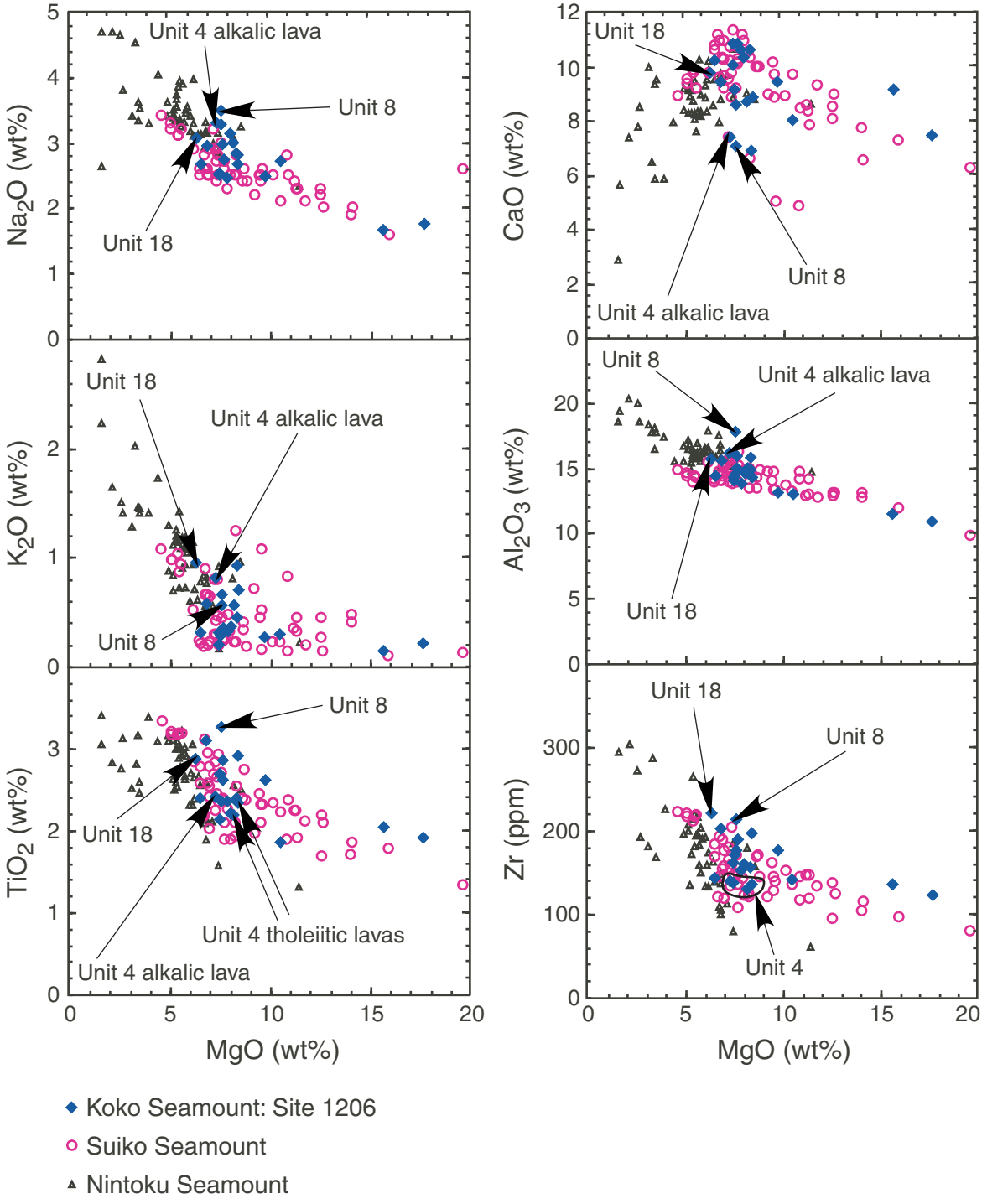

Figure F43. Abundance of Sc vs. MgO comparing data for lavas from Koko, Nintoku, and Suiko Seamounts.

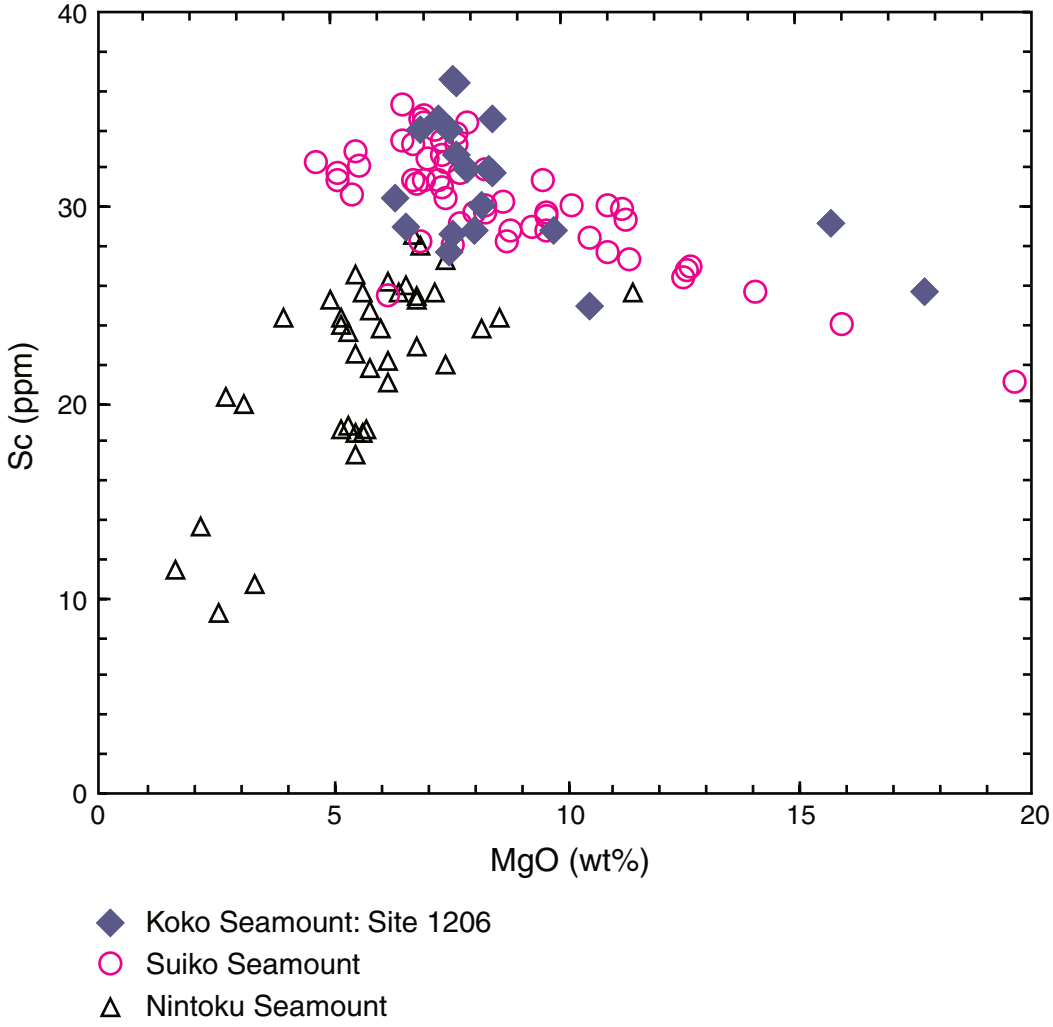

Figure F44. Abundance of Ba, Sr, and Ti vs. Zr comparing data for lavas from Koko, Nintoku, and Suiko Seamounts. The five Nintoku samples offset to high Zr from the Ti vs. Zr trend are hawaiites (see **"Physical Volcanology and Igneous Petrology,"** p. 8, in the "Site 1205" chapter).

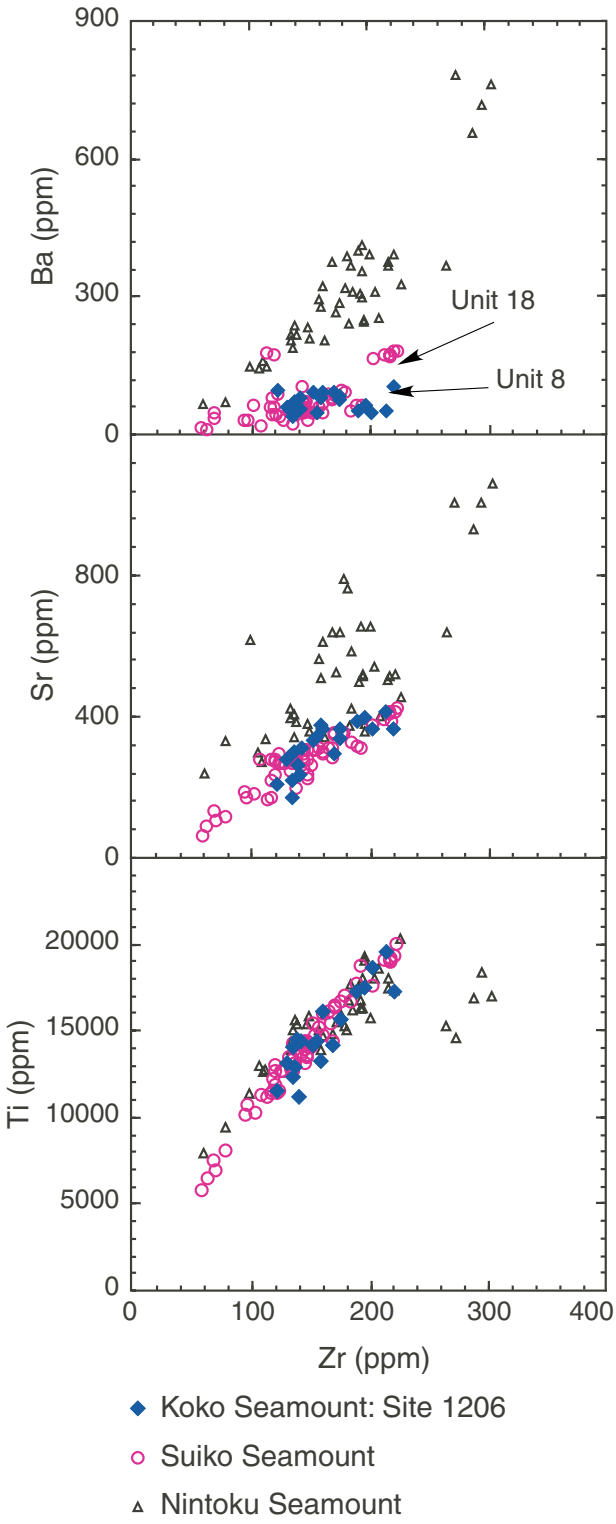

Figure F45. Alkalinity vs. depth in the igneous basement for lavas from Koko, Nintoku, and Suiko Seamounts. Alkalinity is a measure of the deviation from the alkali-tholeiite dividing line in Figure F41, p. 69; negative values indicate tholeiitic lavas. Most of the lava from Nintoku Seamount is alkalic basalt, whereas most of the lava from Koko Seamount is tholeiitic basalt. At Suiko Seamount only the uppermost three lava units are inferred to be alkalic basalt; the alkalic lavas lower in the hole are tholeiitic basalt that gained K_2O during postmagmatic alteration (Jackson et al., 1980).

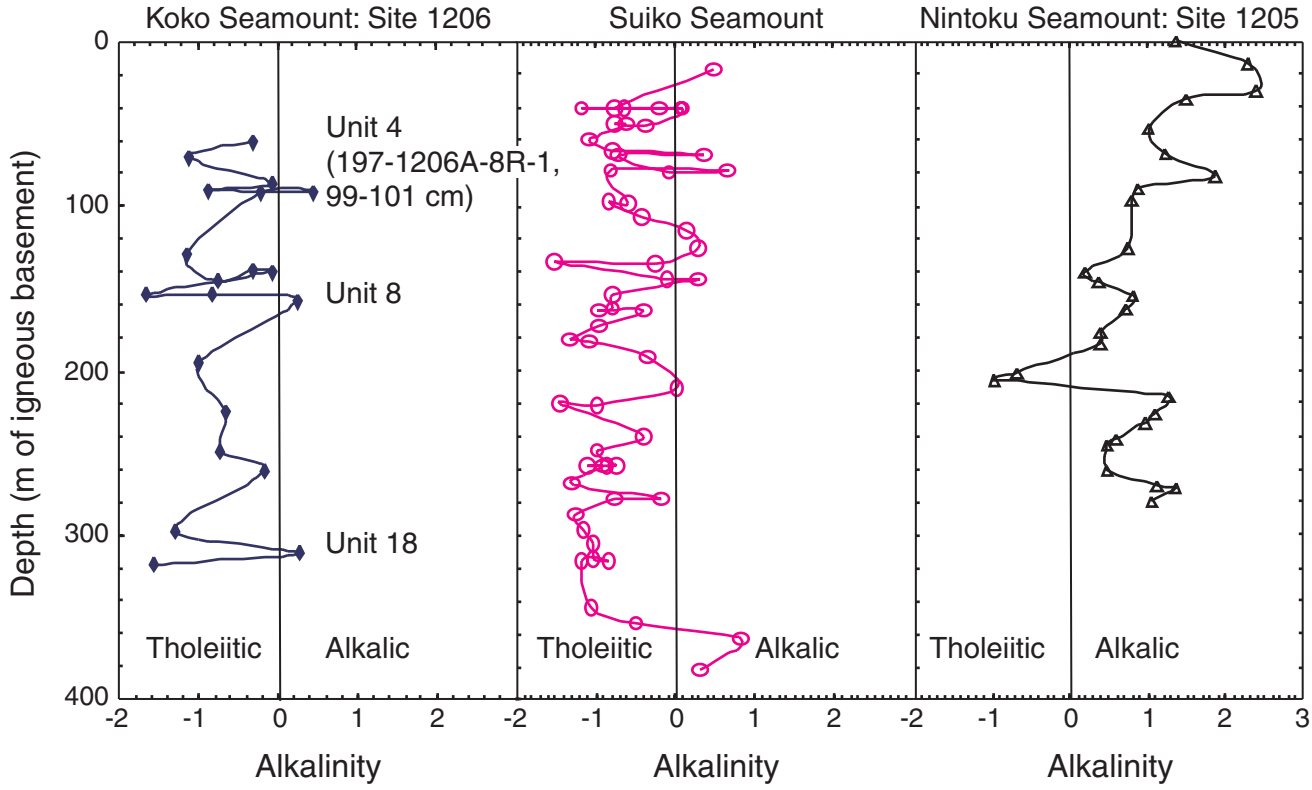

Figure F46. Abundance of TiO_2 and Zr vs. MgO content for eruption Units I, II, IV, and VII. The lines with arrows are olivine control lines for an olivine composition of 70% forsterite.

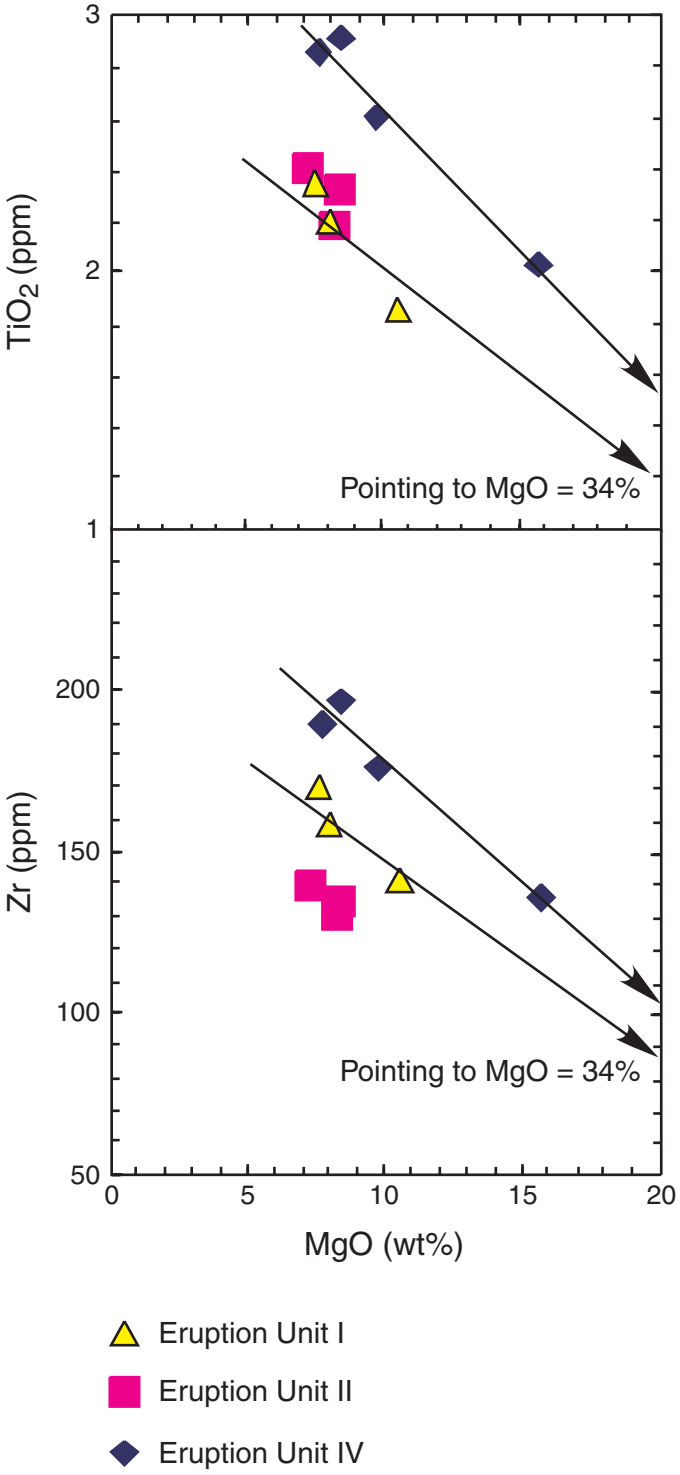

Figure F47. Composite figure showing the alteration degree, mineral assemblages, vesicle occurrence, and vesicle and vein fillings for Hole 1206A. Also shown is the core recovery downhole. Green = sedimentary units, yellow = volcaniclastic units, red = soil horizons, blue = lava flow units. TD = total depth.

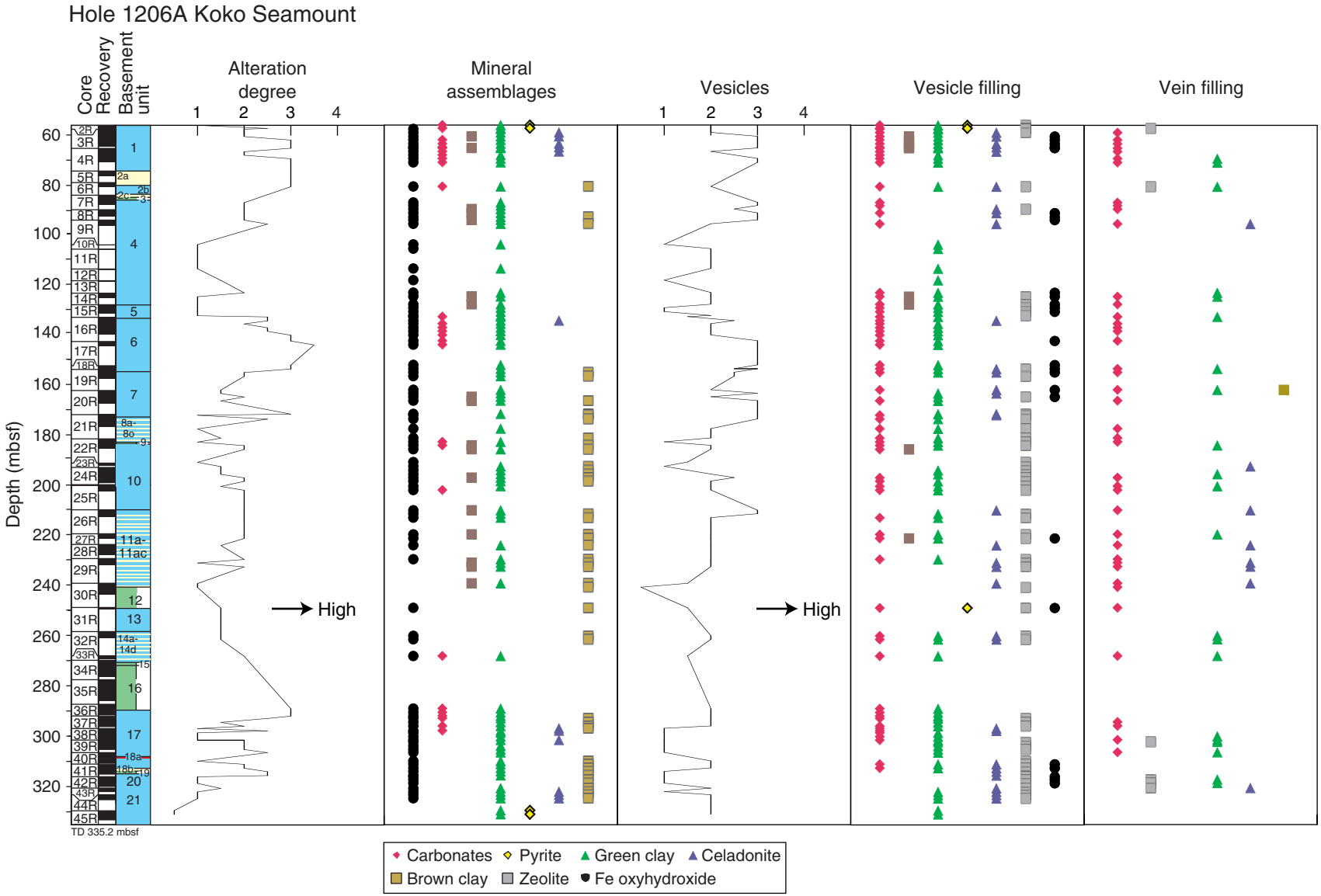

Figure F48. Photograph of a vesicle filled with brown clay (brown-orange colors) and saponite (pale green) (interval 197-1206A-3R-3, 119–138 cm).

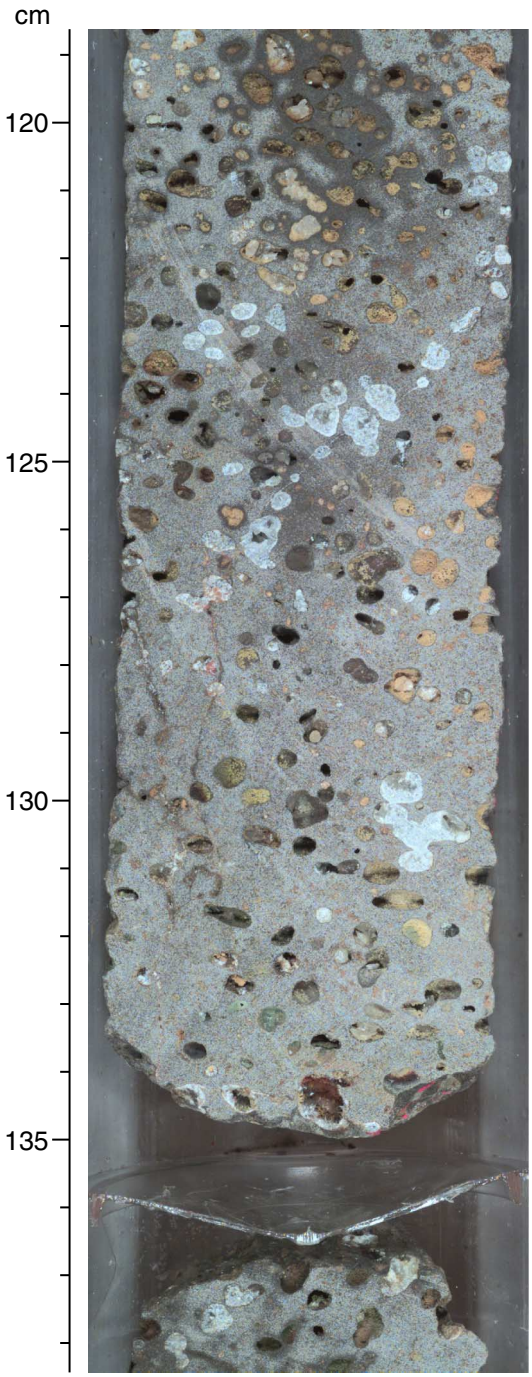

Figure F49. Photograph of a vesicle filled with brown clay (brown-orange), saponite (pale green), celadonite (blue-green), and carbonate (white) (interval 197-1206A-16R-4, 7–26 cm).

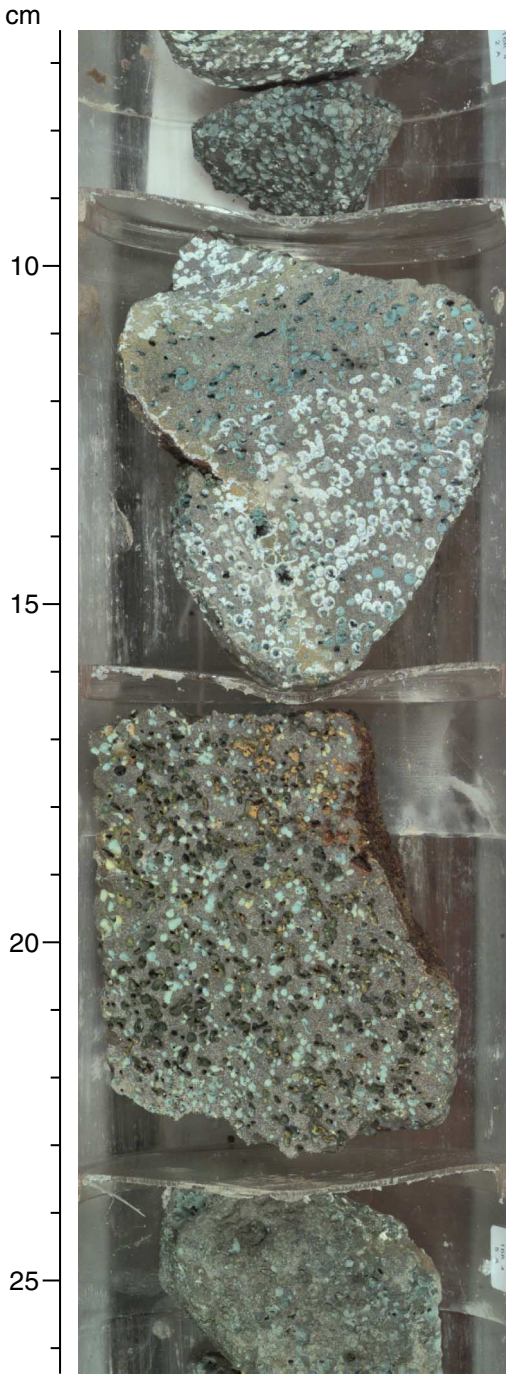

Figure F50. Variations of LOI (loss on ignition), K_2O, Cu/Zr, Co/Zr, and Zn/Zr with depth in the Hole 1206A sequence. Also shown is the core recovery downhole. Green = sedimentary units, yellow = volcaniclastic units, red = soil horizons, blue = lava flow units. TD = total depth.

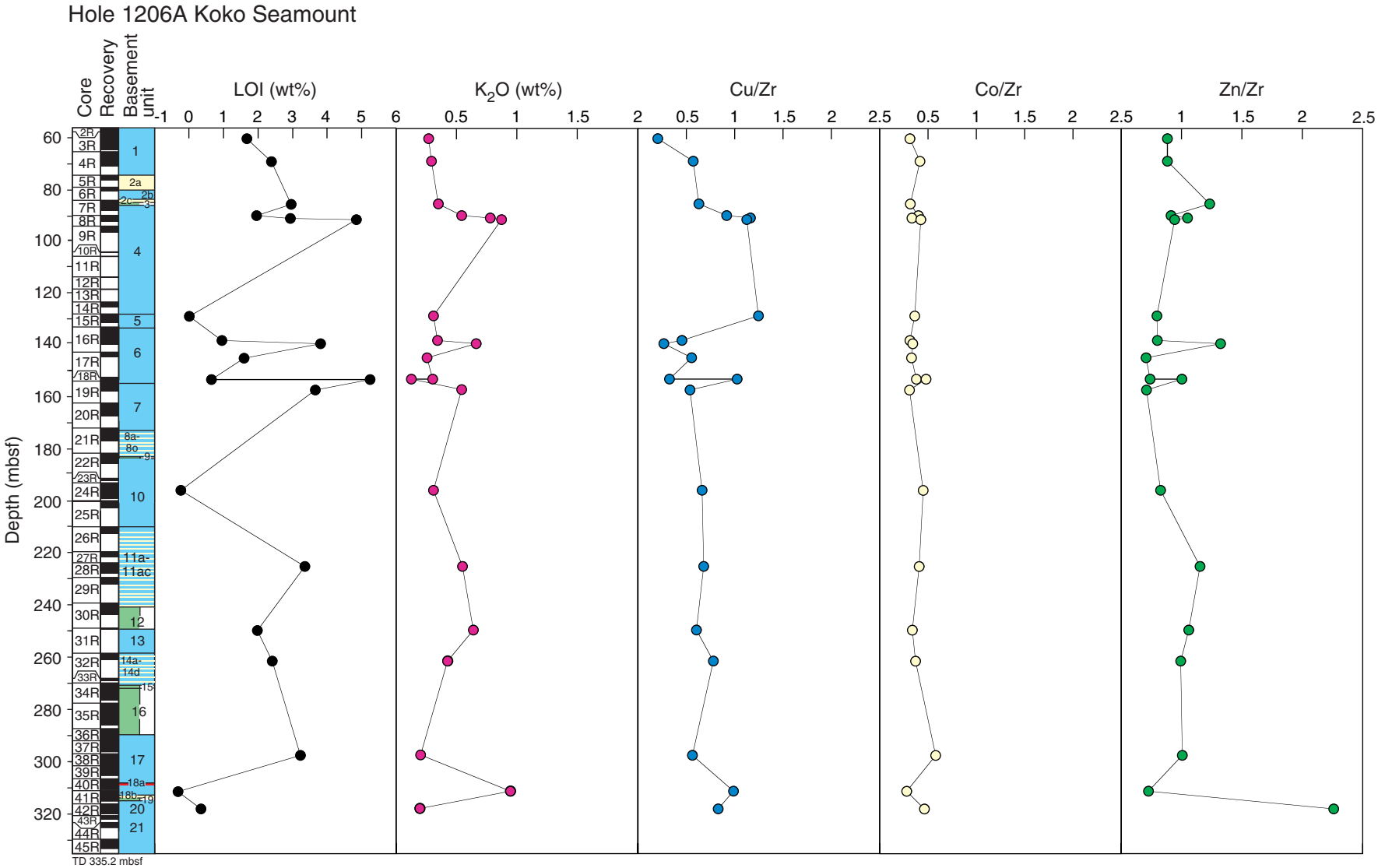

Figure F51. Low-field volume-normalized (bulk) magnetic susceptibility, Koenigsberger ratio, median destructive field (MDF), and the ratio of the vector difference between steps of progressive AF demagnetization (ΔRM) = $[(RM_0 - RM_5)/(RM_{20} - RM_{50})]$ vs. depth for Hole 1206A samples. $RM_0 - RM_5$ = the vector difference between the untreated NRM and NRM after demagnetization at 5 mT, $RM_{20} - RM_{50}$ = the difference between the NRM after 20-mT treatment and NRM after 50-mT treatment. Open circles = lava flow samples, solid circles = volcaniclastic samples. TD = total depth.

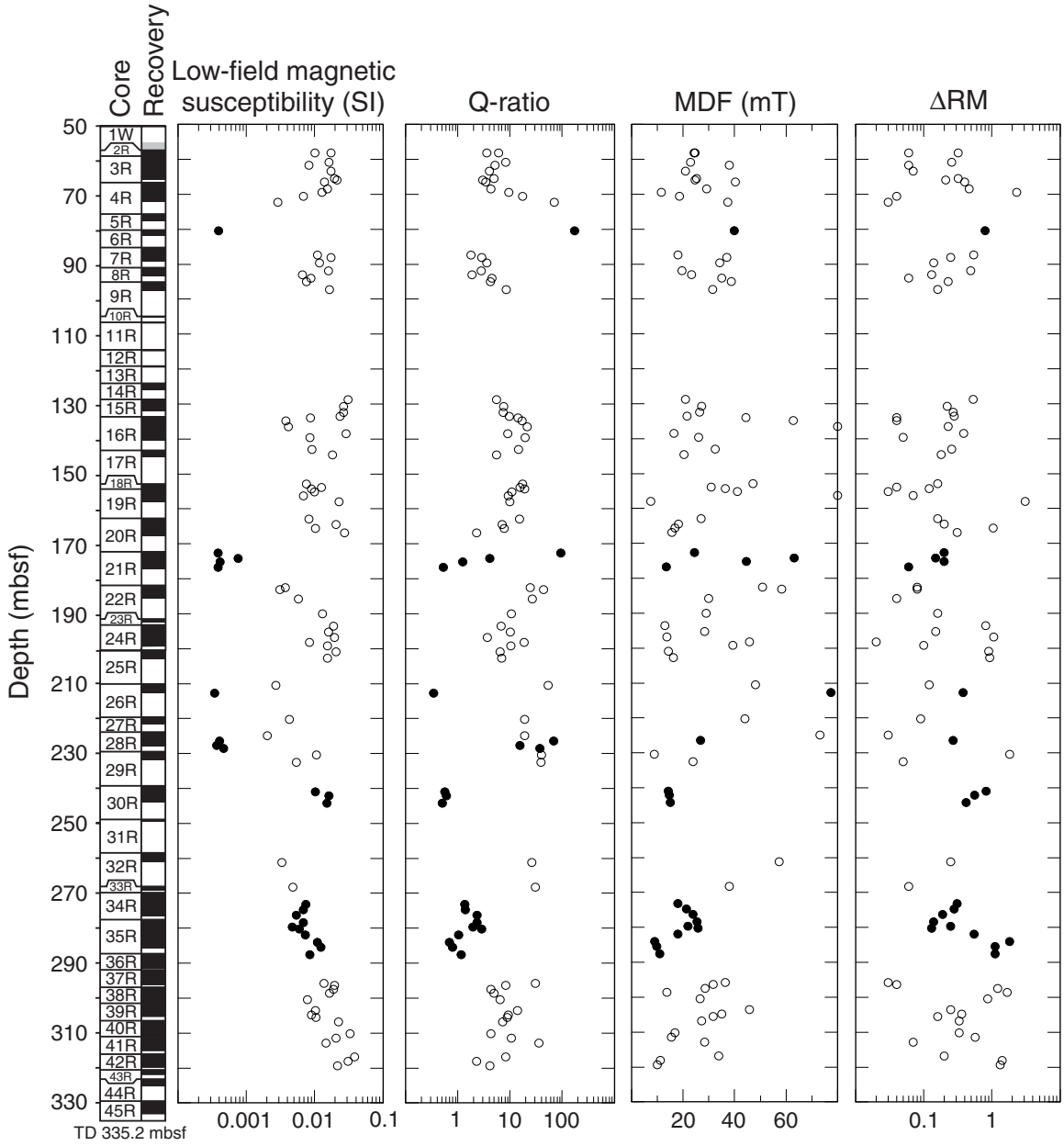

Figure F52. Examples of Lowrie-Fuller tests (Lowrie and Fuller, 1971) conducted on Site 1206 lava flows: Samples (**A**) 197-1206A-3R-2, 99–101 cm, (**B**) 4R-5, 55–57 cm, (**C**) 9R-2, 29–31 cm, (**D**) 16R-5, 75–77 cm, (**E**) 22R-1, 117–119 cm, (**F**) 28R-1, 97–99 cm. ARM = anhysteretic remanent magnetization, SIRM = saturation isothermal remanent magnetization, AF = alternating field.

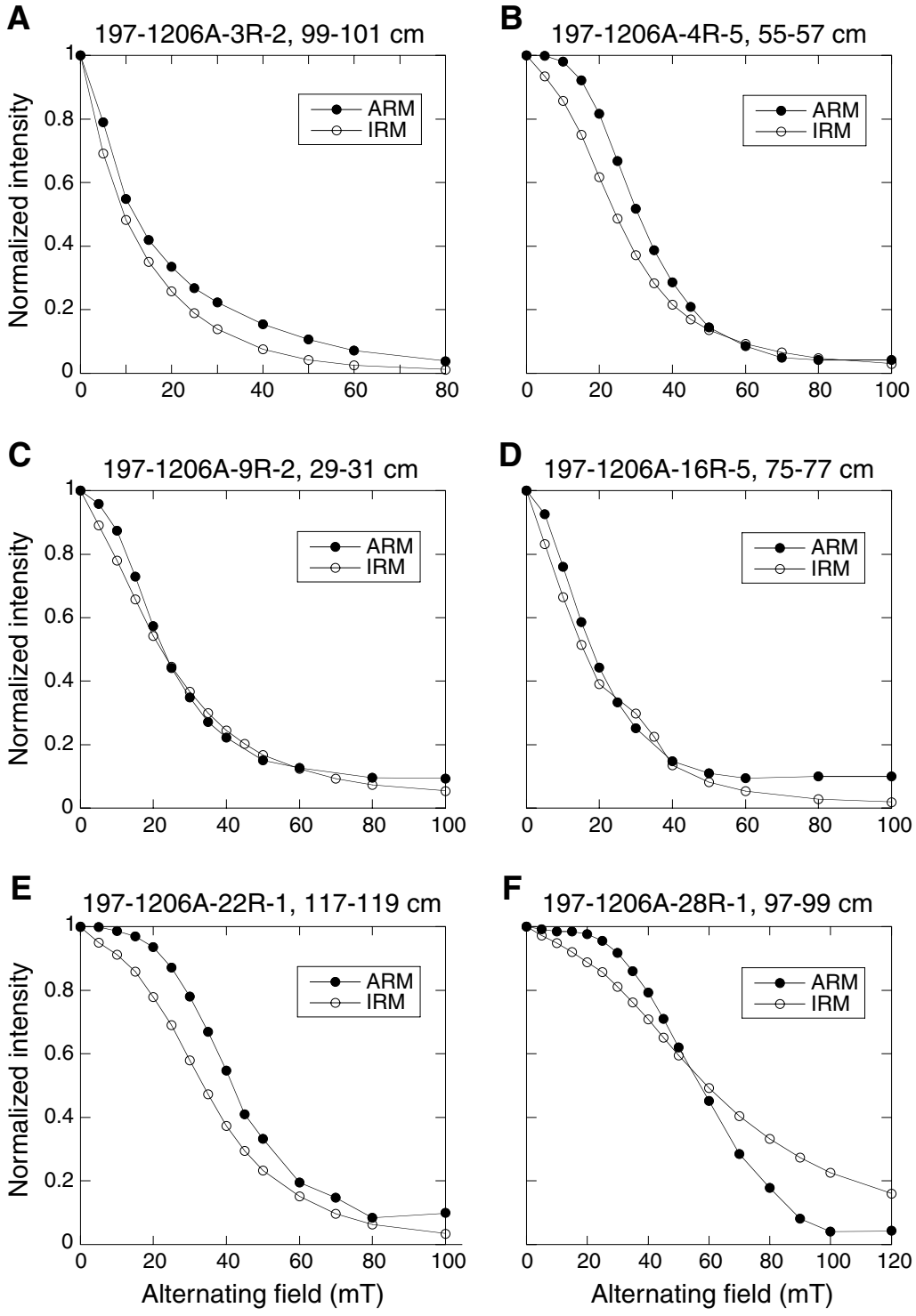

Figure F53. Examples of isothermal remanent magnetization (IRM) acquisition and demagnetization (backfield IRM) (see **"Lowrie-Fuller Tests and Coercivity of Remanence Measurements,"** p. 19) used to calculate coercivity of remanence from Hole 1206A lava samples: (**A**) 197-1206A-3R-2, 99–101 cm, (**B**) 4R-5, 55–57 cm, (**C**) 9R-2, 29–31 cm, (**D**) 16R-5, 75–77 cm, (**E**) 22R-1, 117–119 cm, and (**F**) 28R-1, 97–99 cm.

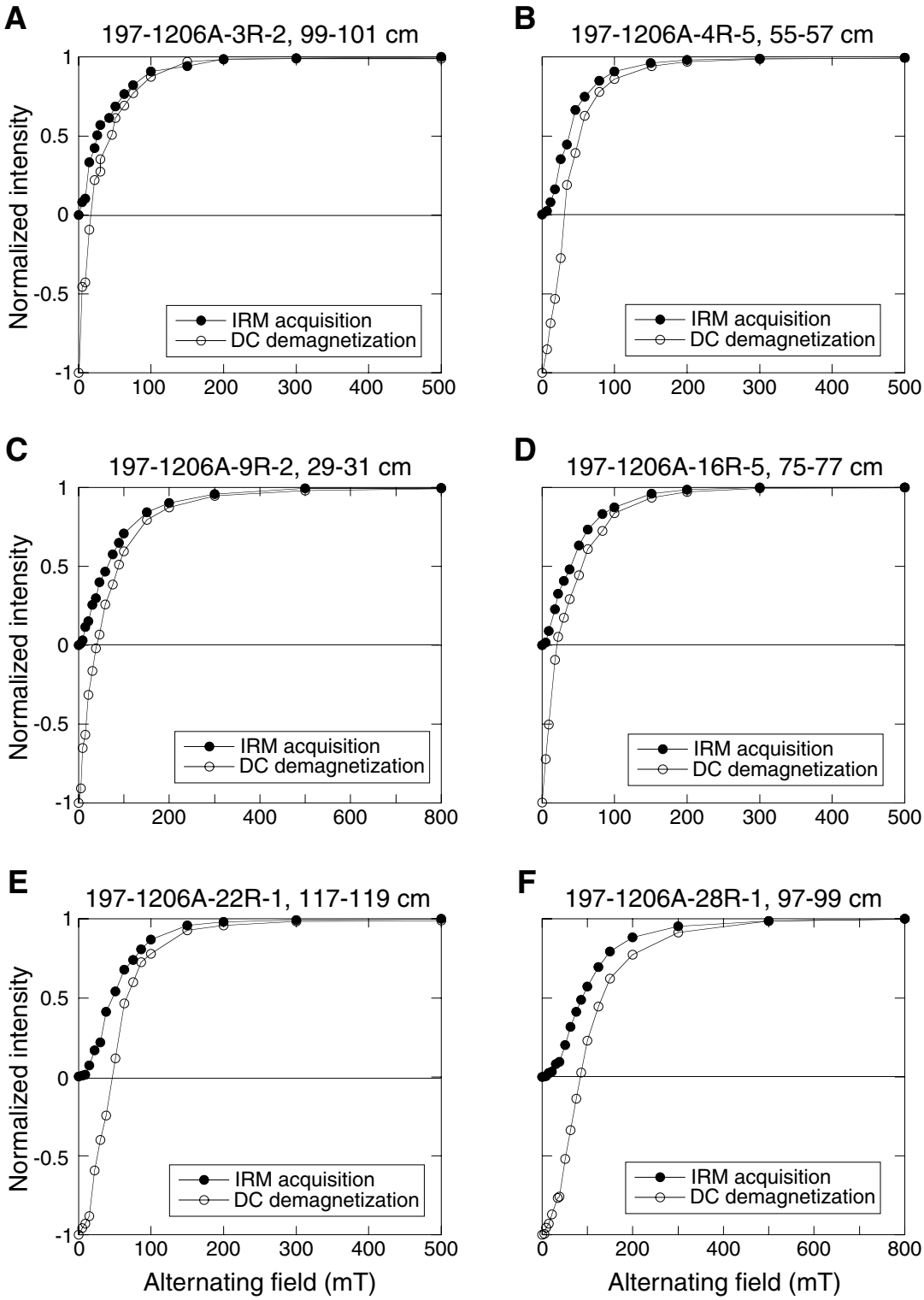

Figure F54. Normalized NRM decay spectra (A, C) and Lowrie-Fuller tests (B, D) (Lowrie and Fuller, 1971) conducted on these samples that suggest single-domain behavior. **A, B.** Sample 197-1206A-4R-5, 55–57 cm. **C, D.** Sample 197-1206A-22R-1, 117–119 cm.

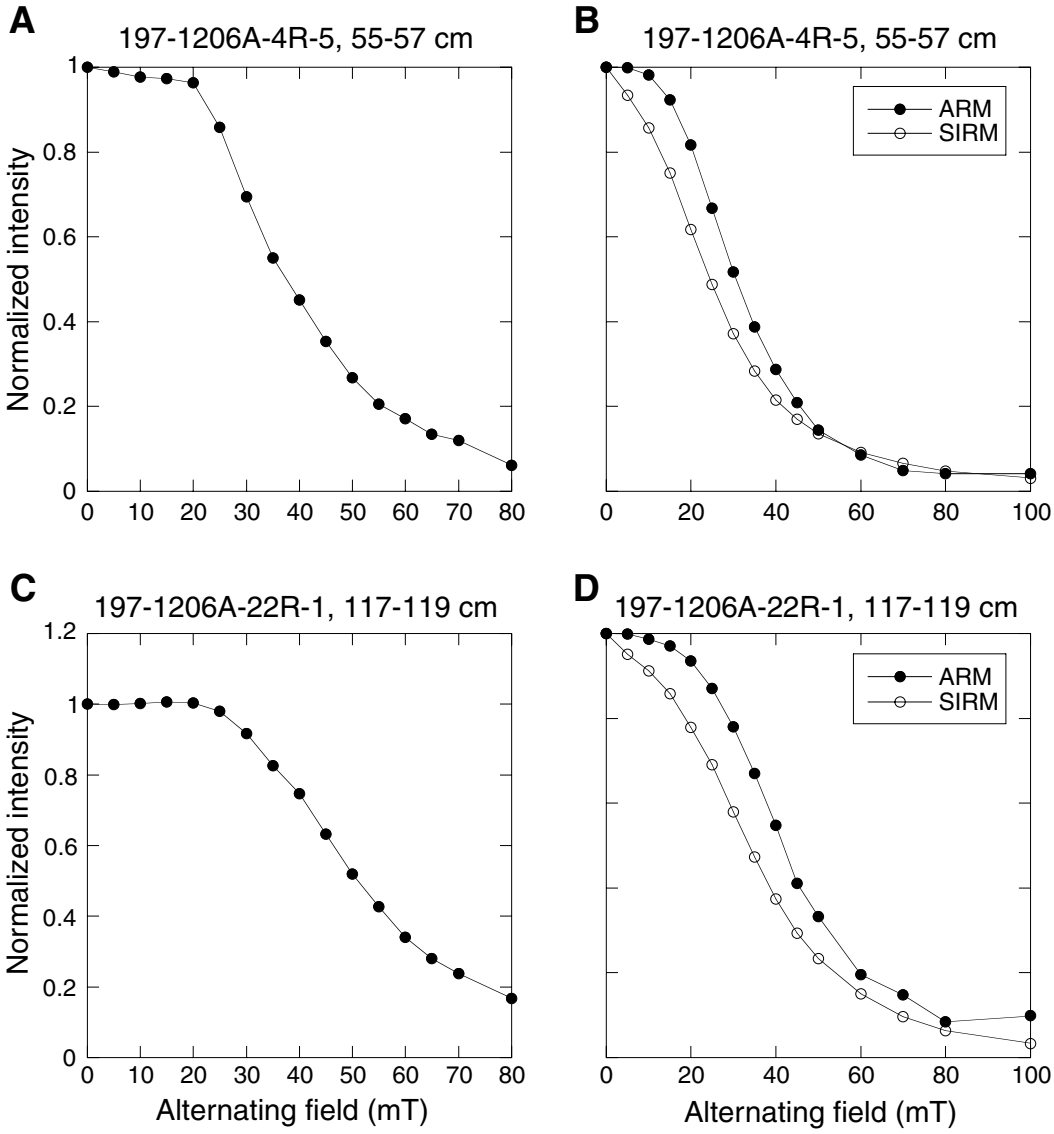

Figure F55. A. $\Delta RM = (RM_0 - RM_5)/(RM_{20} - RM_{50})$ (log scale) vs. compressional wave velocity (V_P). **B.** ΔRM (log scale) vs. inclination of soft component. ΔRM = ratio of the vector difference between steps of progressive AF demagnetization, $RM_0 - RM_5$ = the vector difference between the untreated NRM and NRM after demagnetization at 5 mT, $RM_{20} - RM_{50}$ = the difference between the NRM after 20-mT treatment and NRM after 50-mT treatment. Open circles = lava flow samples, solid circles = volcaniclastic samples.

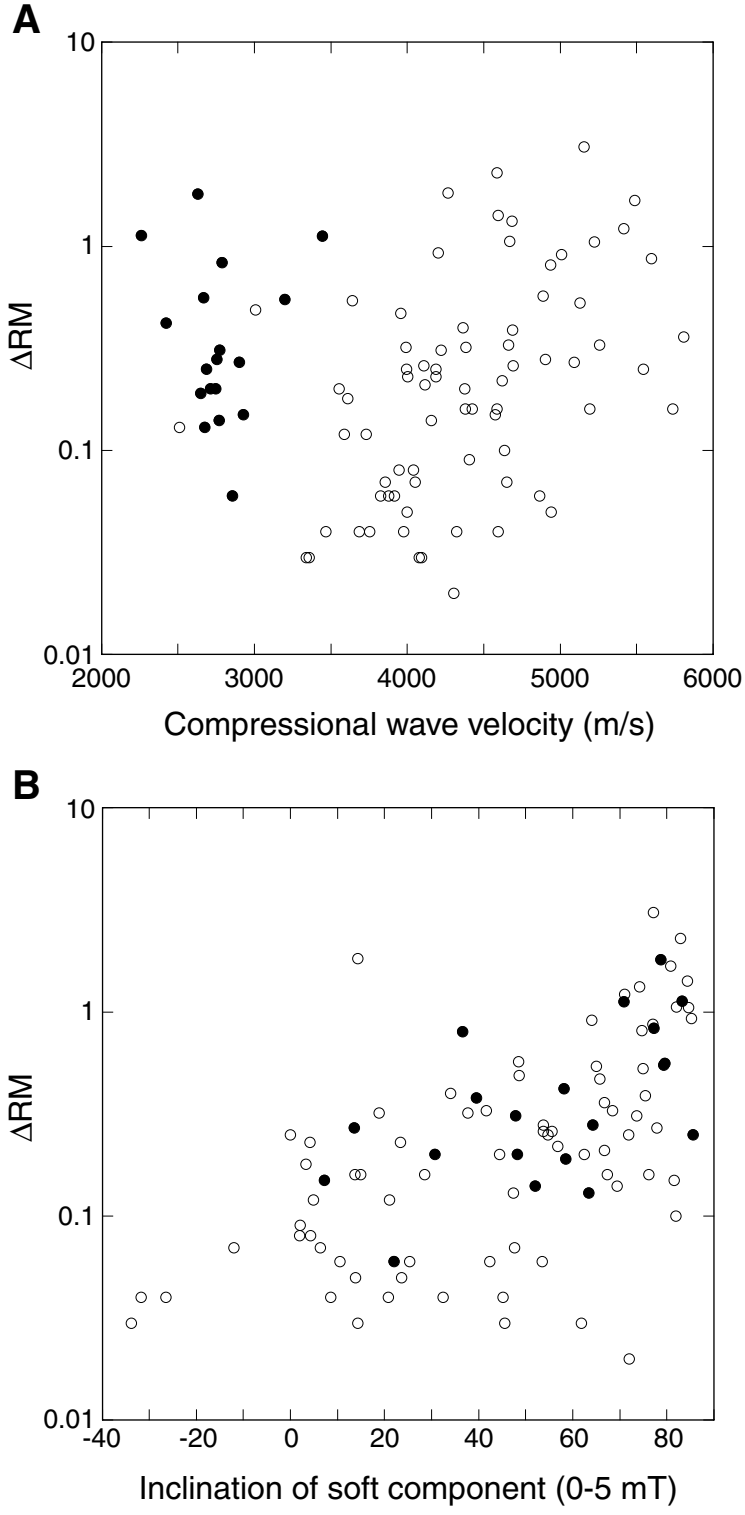

Figure F56. Examples orthogonal vector plots showing well-defined, stable magnetic behavior recorded by volcaniclastic sediments: Samples (**A**) 197-1206A-21R-3, 47–49 cm, (**B**) 30R-1, 37–39 cm, (**C**) 34R-3, 68–70 cm, (**D**) 34R-5, 76–78 cm, and (**E**) 35R-3, 45–47 cm. Open symbols = inclination values, solid symbols = declination values.

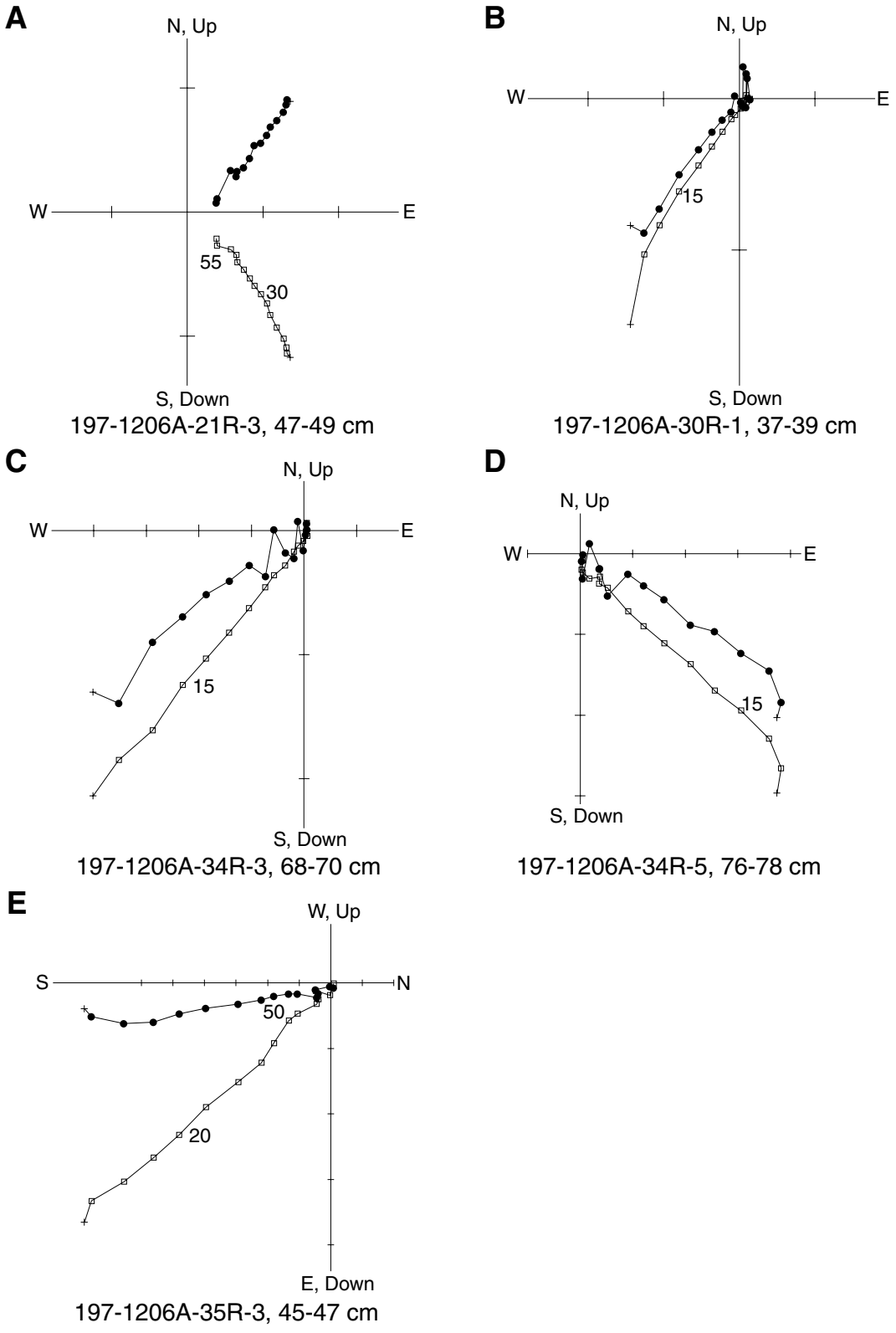

Figure F57. Example orthogonal vector plots showing well-defined, stable magnetic behavior recorded by Hole 1206A lavas: Samples (**A**) 197-1206A-3R-4, 59–61 cm, (**B**) 7R-4, 64–66 cm, (**C**) 16R-1, 33–35 cm, (**D**) 18R-2, 17–19 cm, (**E**) 20R-2, 85–87 cm, and (**F**) 23R-1, 109–111 cm. Open symbols = inclination values, solid symbols = declination values.

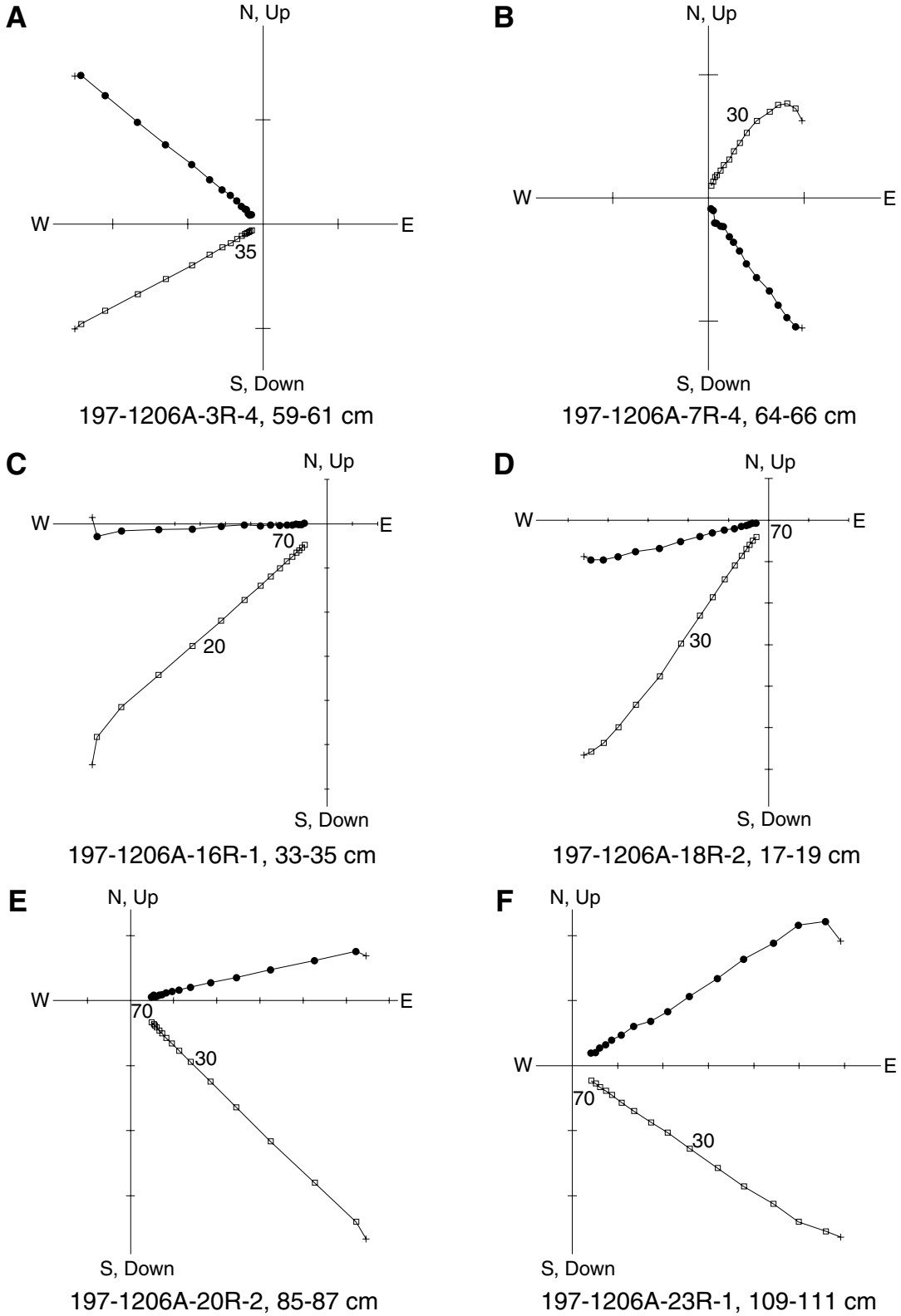

Figure F58. Example orthogonal vector plots showing well-defined magnetic components recorded by Hole 1206A lava flow samples that are not completely demagnetized by the alternating-field treatment applied: Samples (**A**) 197-1206A-3R-2, 99–101 cm, (**B**) 4R-1, 43–45 cm, (**C**) 9R-1, 29–31 cm, (**D**) 15R-3, 118–120, (**E**) 19R-1, 55–57, and (**F**) 22R-2, 28–30 cm. Open symbols = inclination values, solid symbols = declination values.

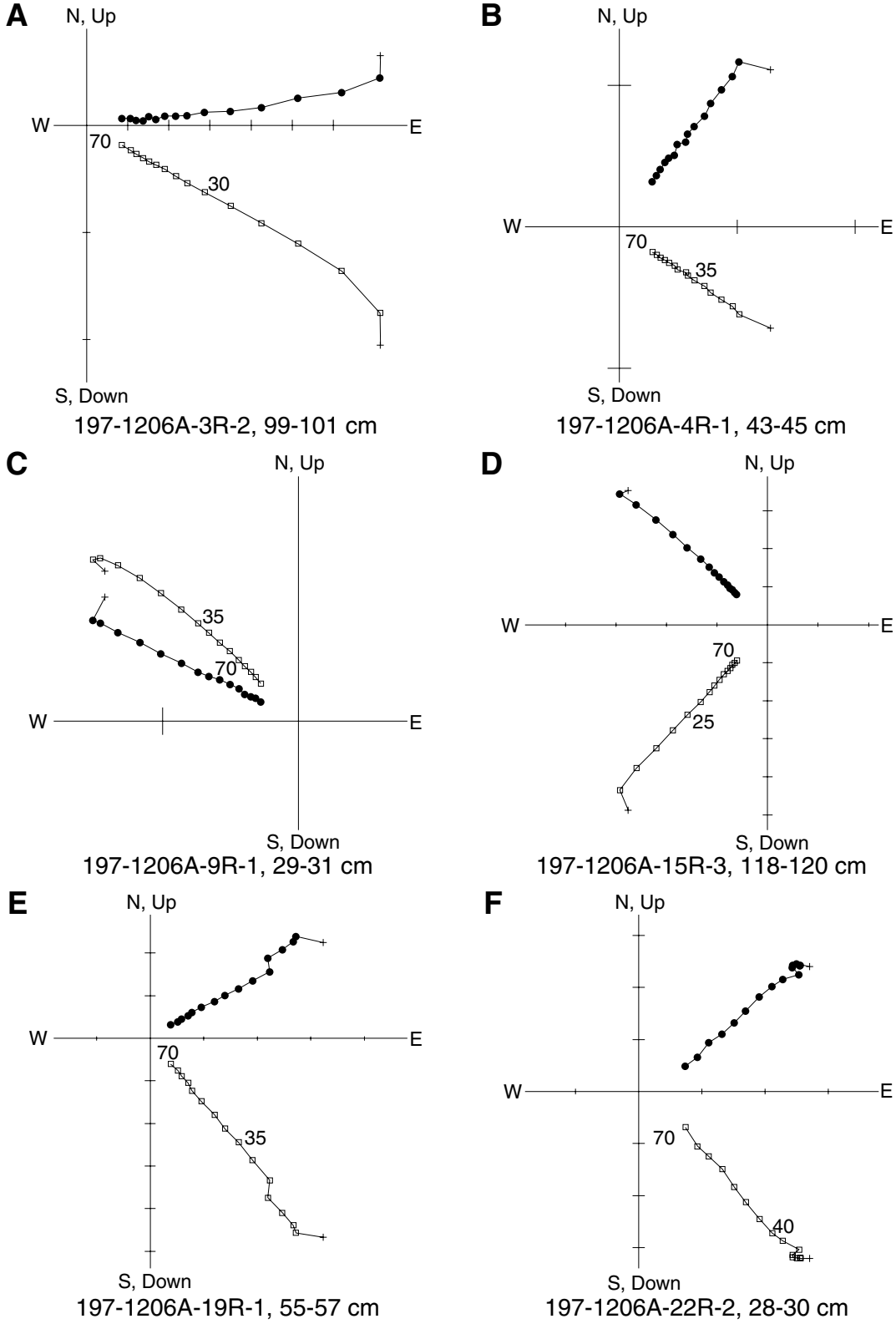

Figure F59. Example orthogonal vector plots showing nonideal behavior as recorded by Hole 1206A lavas: Samples (**A**) 197-1206A-4R-2, 100–102 cm, (**B**) 7R-3, 39–41 cm, (**C**) 16R-3, 55–57 cm, and (**D**) 26R-1, 32–34 cm. Open symbols = inclination values, solid symbols = declination values.

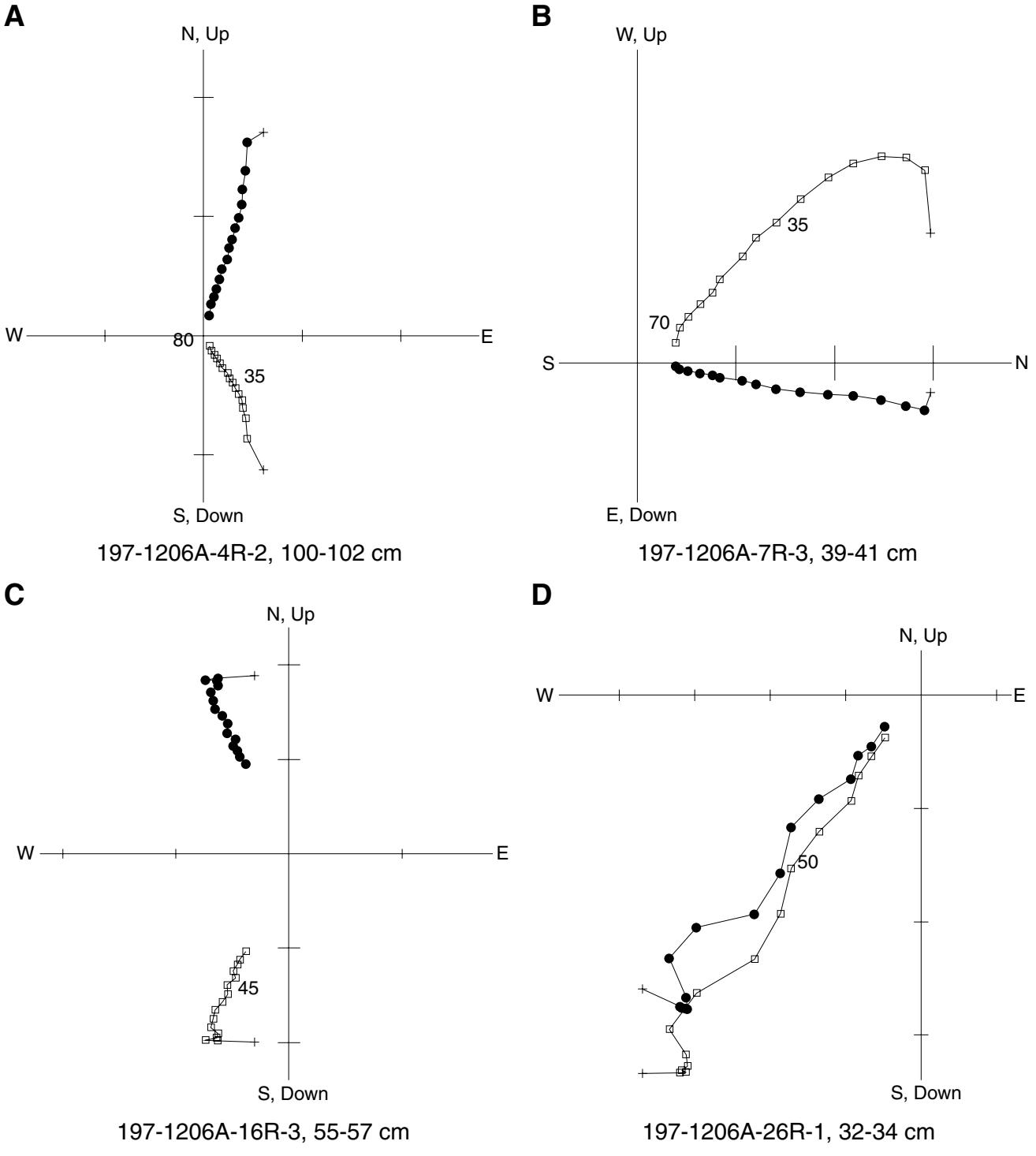

Figure F60. Histogram of inclination values derived from principal component analyses of lava flows recovered at Site 1206 compared to a synthetic Fisher distribution (Fisher, 1953) having the same precision parameter (*k*) as the experimental data.

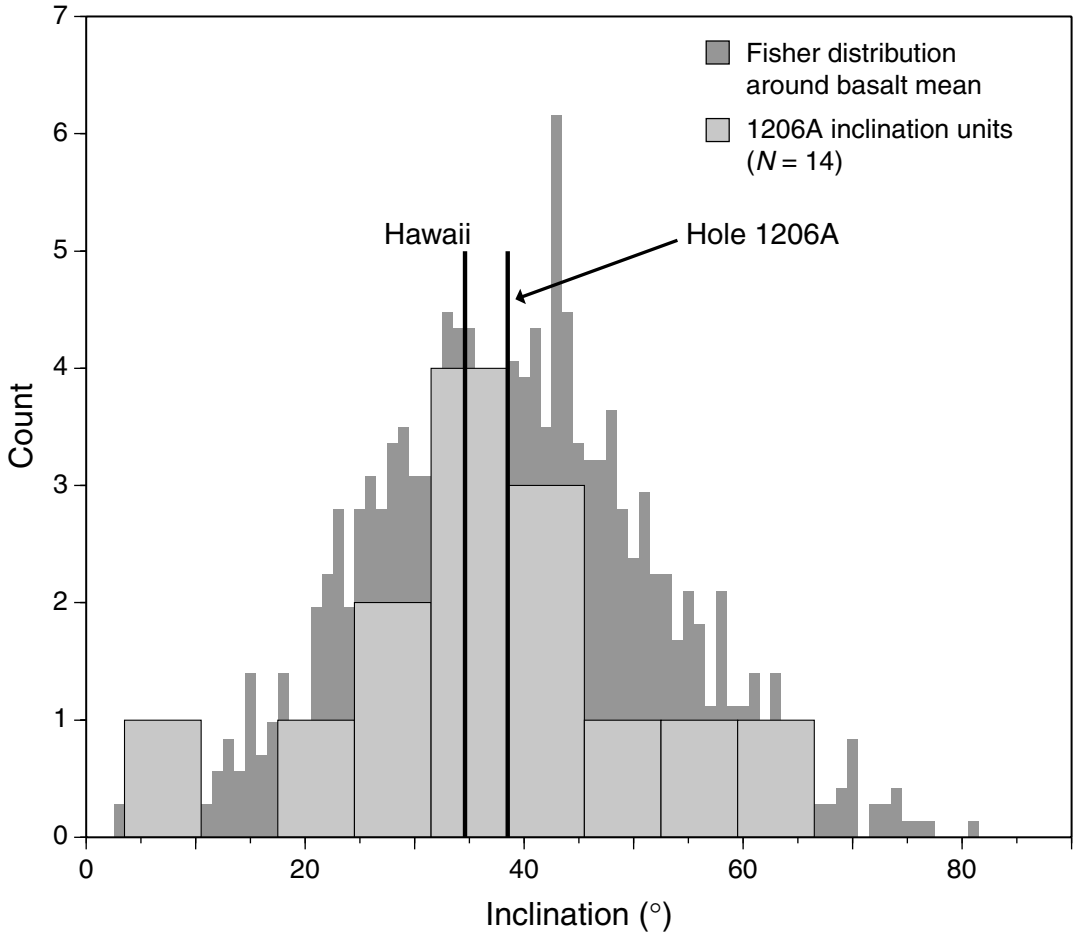

Figure F61. Summary of physical properties measurements. **A**. Natural gamma ray. **B**. Bulk density. **C**. Grain density. **D**. Porosity.

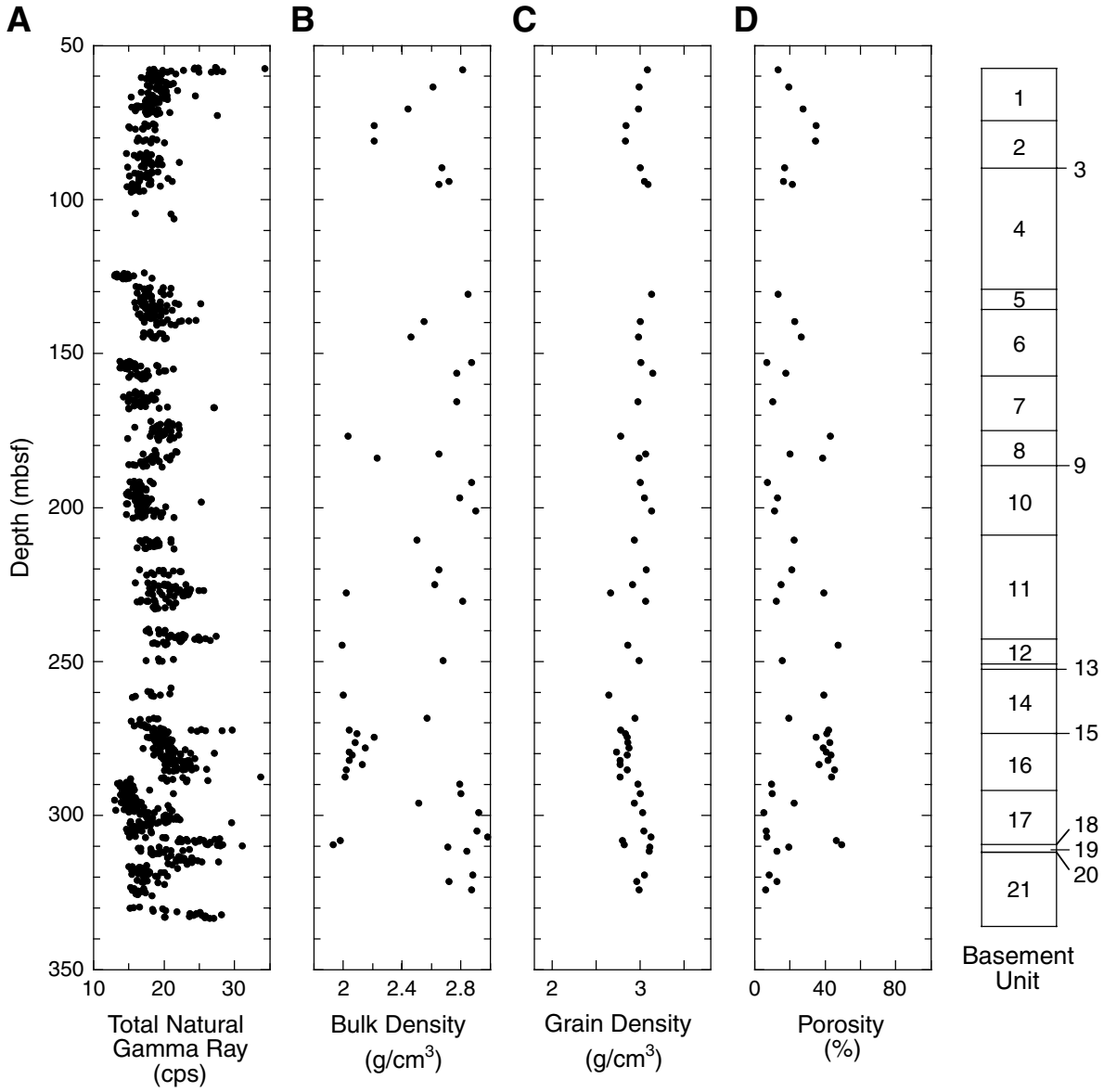

Figure F62. Thermal conductivity measurements vs. depth.

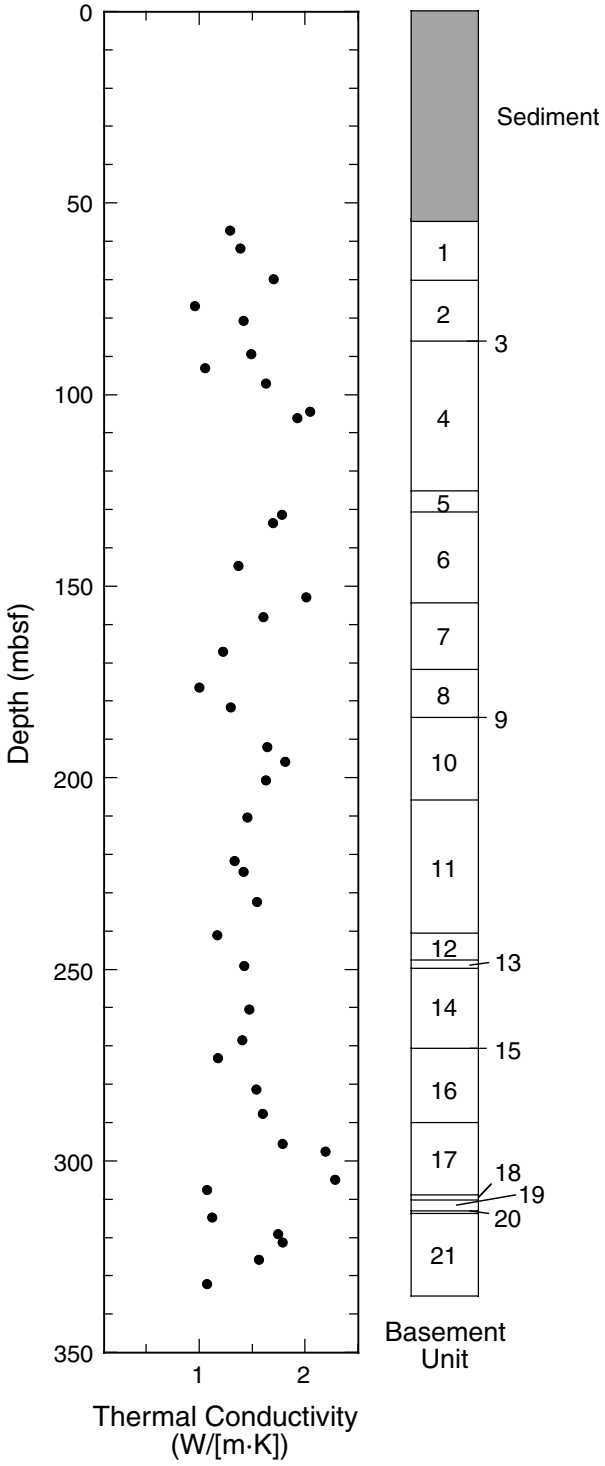

Figure F63. Compressional wave velocity.

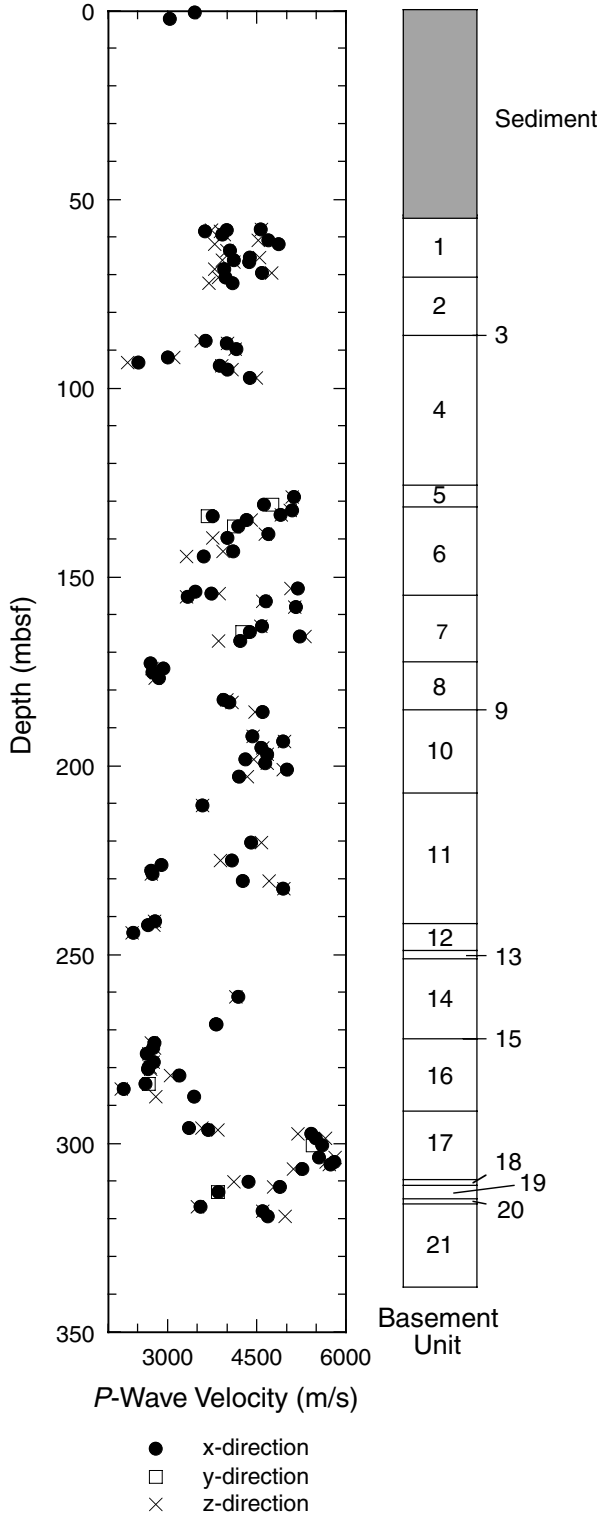

Figure F64. Bulk density vs. *P*-wave velocity.

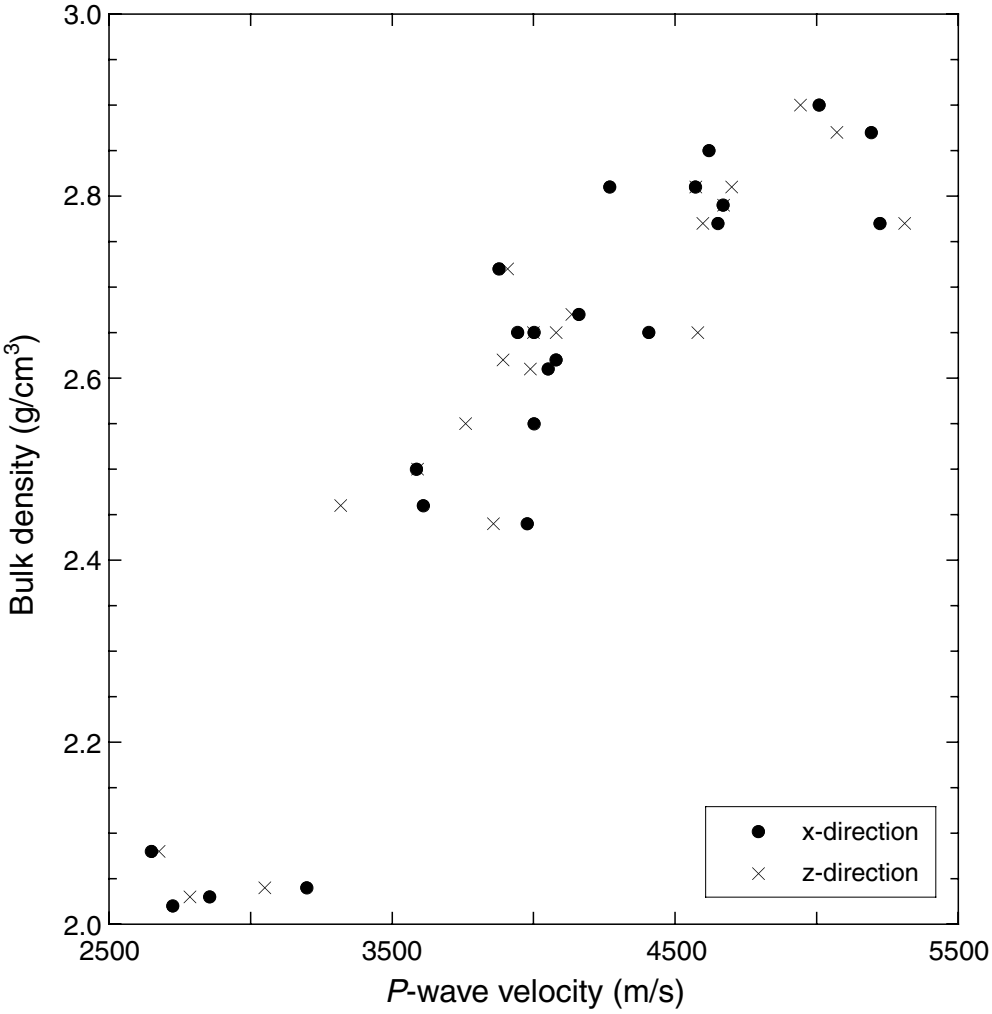

Figure F65. Ship track for Leg 197, Site 1206 seismic reflection survey and *SP Lee* 8-76 survey. Tick marks show half-hour time intervals for the Leg 197 survey, and 1-hr time intervals for the *SP Lee* survey.

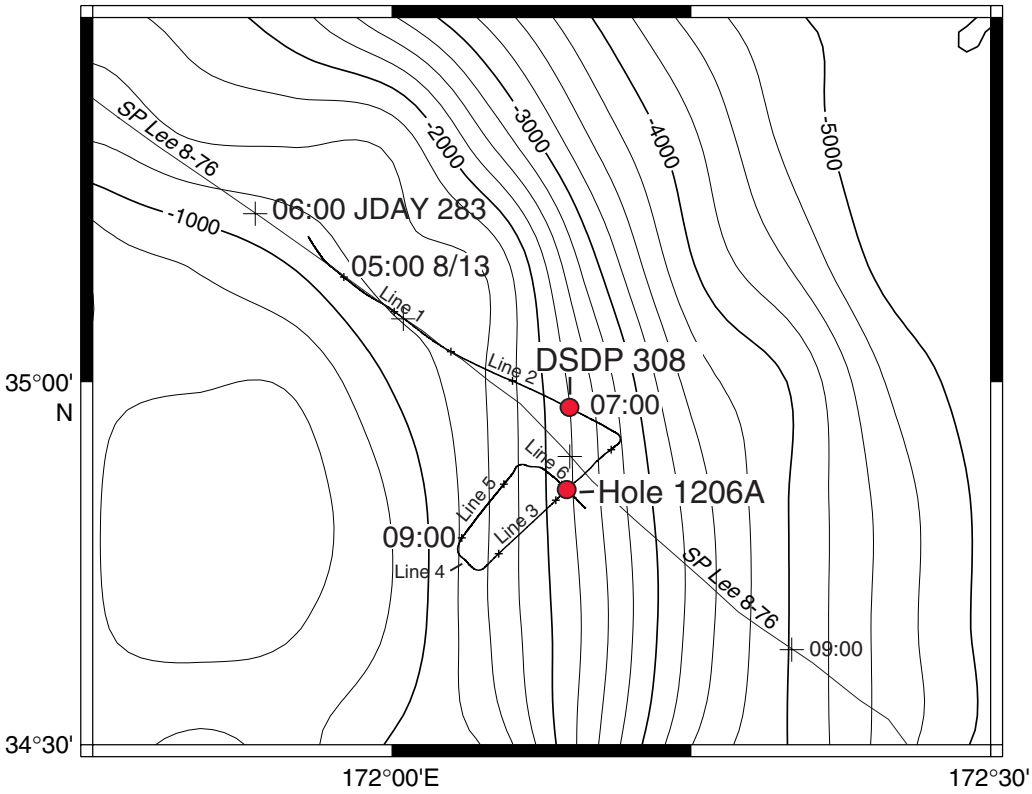

Figure F66. Survey Line 3, 2.5-km-long finite-difference migrated time section. Data are bandpass filtered between 55 and 150 Hz. Hole 1206A is at about shotpoint 3023. Trace-to-trace distance = ~13 m, vertical exaggeration at the seafloor = ~4.25:1, bottom of Hole 1206A = ~2.25 s two-way traveltime. Arrows point to possible boundaries between lava flow sequences.

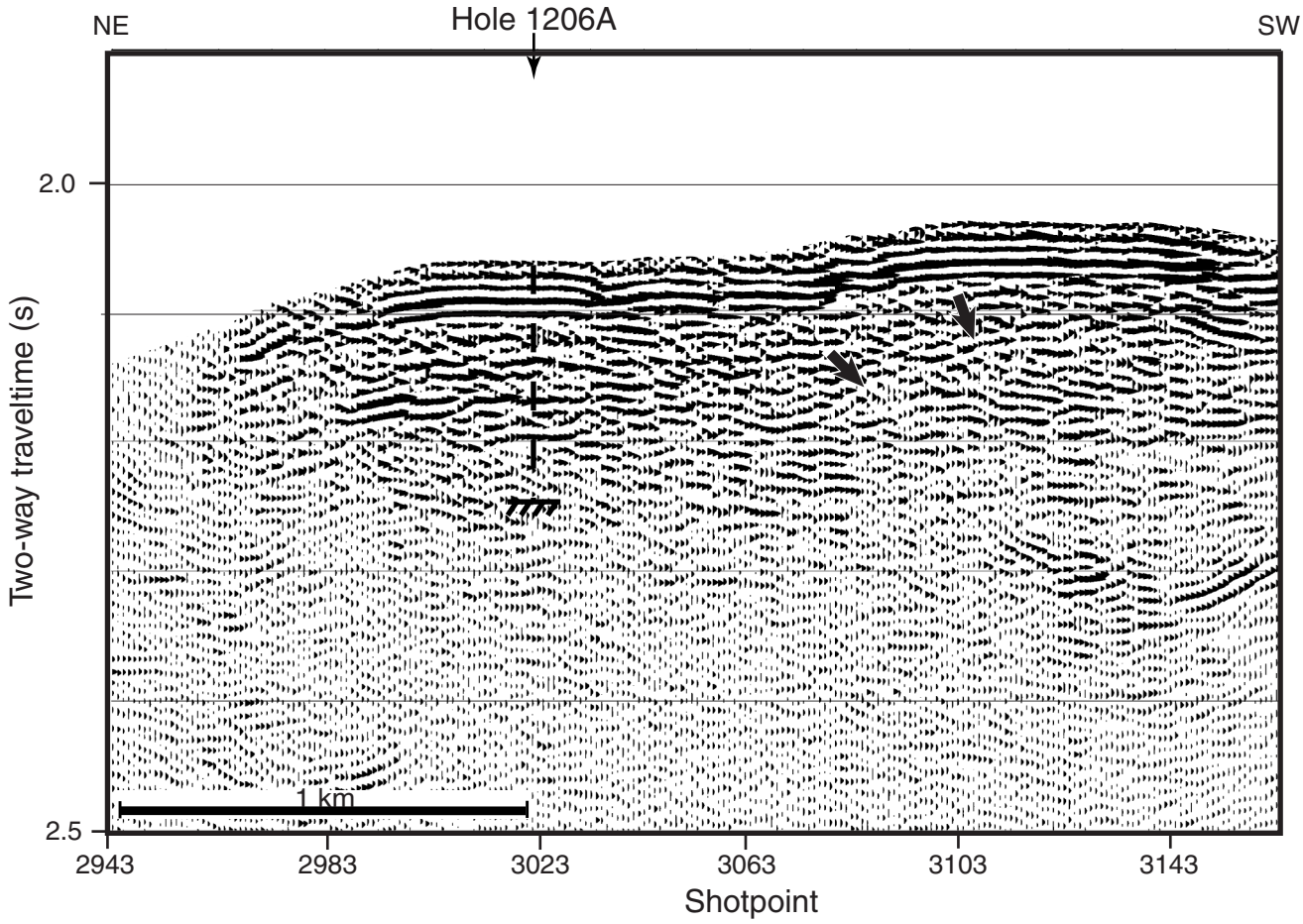

Figure F67. Survey Line 6, 2.5-km-long finite-difference migrated time section. Data are bandpass filtered between 45 and 120 Hz. Hole 1206A is at approximately shotpoint 4947. Trace-to-trace distance = ~13 m, vertical exaggeration at the seafloor = ~4.25:1, bottom of Hole 1206A = ~2.25 s two-way traveltime.

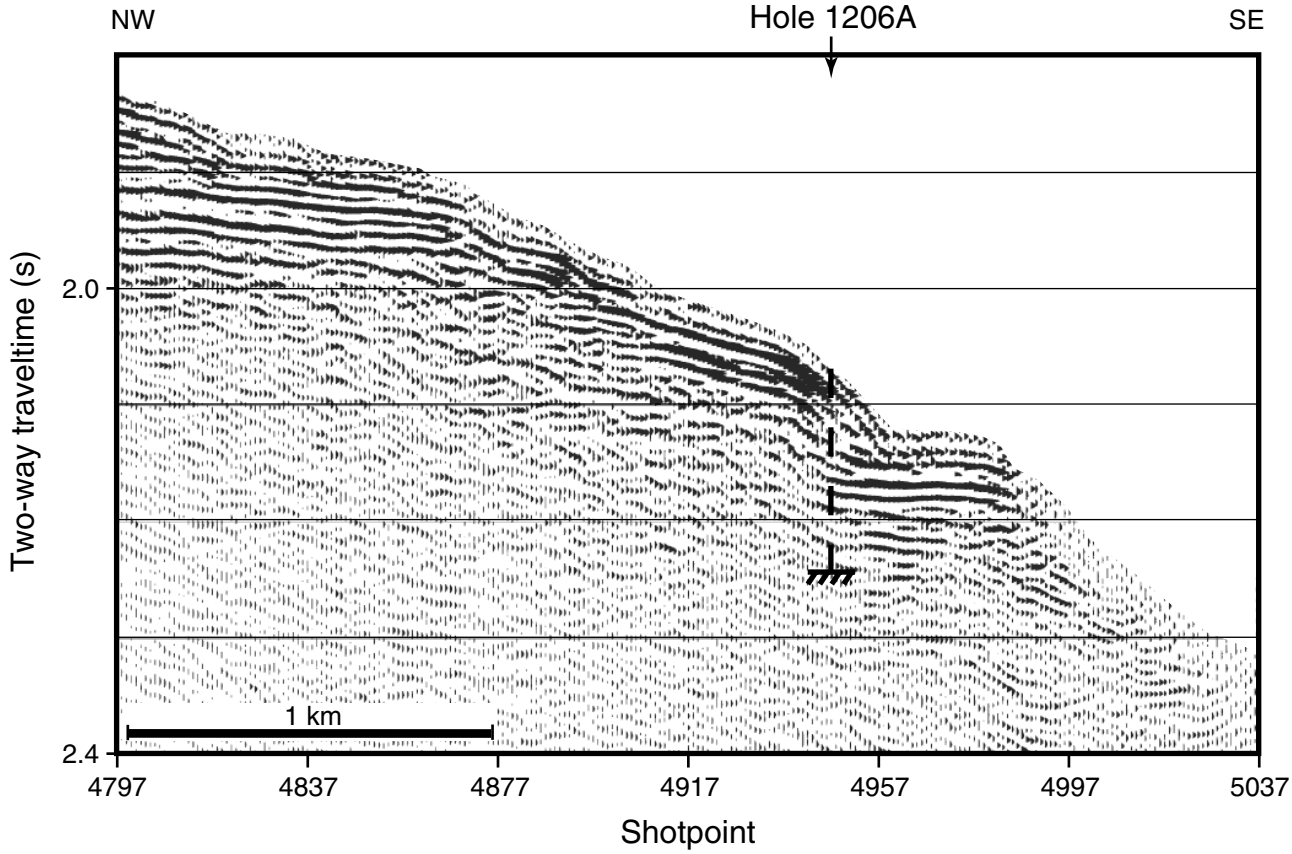

Table T1. Coring summary, Site 1206.

Latitude: 34°55.5485′N
Longitude: 172°8.7536′E
Time on site (hr): 169.25 (2115 hr, 13 Aug–2230 hr, 20 Aug 2001)
Seafloor (drill pipe measurement from rig floor, mbrf): 1557.0
Distance between rig floor and sea level (m): 11.3
Water depth (drill pipe measurement from sea level, m): 1545.7
Total depth (drill pipe measurement from rig floor, mbrf): 1892.2
Total penetration (meters below seafloor, mbsf): 335.2
Total length of cored section (m): 278.2
Total length of drilled intervals (m): 57.0
Total core recovered (m): 141.43
Core recovery (%): 50.8
Total number of cores: 44
Total number of drilled intervals: 1

Core	Date (Aug 2001)	Ship time (local)	Depth (mbsf) Top	Depth (mbsf) Bottom	Length (m) Cored	Length (m) Recovered	Recovery (%)	Comments
197-1206A-								
1W	Wash core		0.0	57.0		2.30	NA	AHC 28–38 m
2R	14	0730	57.0	58.5	1.5	1.62	108.0	AHC
3R	14	1020	58.5	66.1	7.6	6.75	88.8	AHC
4R	14	1555	66.1	75.1	9.0	5.54	61.6	AHC
5R	14	1720	75.1	79.8	4.7	1.89	40.2	AHC
6R	14	2145	79.8	84.7	4.9	1.42	29.0	AHC
7R	15	0045	84.7	90.4	5.7	3.88	68.1	AHC
8R	15	0220	90.4	94.7	4.3	2.60	60.5	AHC
9R	15	0735	94.7	104.4	9.7	2.24	23.1	AHC
10R	15	1100	104.4	106.1	1.7	0.25	14.7	AHC
11R	15	1340	106.1	114.0	7.9	0.12	1.5	AHC
12R	15	1525	114.0	118.7	4.7	0.02	0.4	AHC
13R	15	1800	118.7	123.6	4.9	0.04	0.8	AHC
14R	15	2015	123.6	128.2	4.6	2.02	43.9	AHC; rocks were the material stuck in the bit and the outer core barrel; the pieces are not in order and not oriented
15R	16	1520	128.2	133.2	5.0	3.62	72.4	AHC; round trip to change bit after Core 14R
16R	16	1805	133.2	142.8	9.6	6.56	68.3	AHC
17R	16	2150	142.8	152.4	9.6	1.94	20.2	AHC
18R	16	2330	152.4	153.8	1.4	1.46	104.3	AHC
19R	17	0210	153.8	162.2	8.4	3.87	46.1	AHC
20R	17	0445	162.2	171.8	9.6	5.22	54.4	AHC
21R	17	0730	171.8	181.4	9.6	4.98	51.9	AHC
22R	17	1055	181.4	191.0	9.6	3.86	40.2	AHC
23R	17	1310	191.0	192.7	1.7	1.13	66.5	AHC
24R	17	1650	192.7	200.6	7.9	6.20	78.5	AHC
25R	17	2015	200.6	210.2	9.6	2.42	25.2	AHC
26R	17	2240	210.2	219.8	9.6	2.73	28.4	AHC
27R	18	0115	219.8	224.0	4.2	1.82	43.3	AHC
28R	18	0335	224.0	229.6	5.6	4.04	72.1	AHC
29R	18	0730	229.6	239.3	9.7	2.48	25.6	AHC
30R	18	1020	239.3	248.9	9.6	4.59	47.8	AHC
31R	18	1415	248.9	258.5	9.6	0.71	7.4	AHC
32R	18	1800	258.5	268.1	9.6	2.50	26.0	AHC
33R	18	1950	268.1	269.9	1.8	1.14	63.3	AHC
34R	18	2300	269.9	277.7	7.8	6.68	85.6	AHC
35R	19	0150	277.7	287.3	9.6	8.17	85.1	AHC
36R	19	0445	287.3	291.9	4.6	4.40	95.7	AHC
37R	19	0750	291.9	296.9	5.0	4.53	90.6	AHC
38R	19	1050	296.9	301.5	4.6	4.81	104.6	AHC
39R	19	1350	301.5	306.5	5.0	3.97	79.4	AHC
40R	19	1545	306.5	311.1	4.6	4.34	94.4	AHC
41R	19	1800	311.1	316.1	5.0	4.12	82.4	AHC
42R	19	2115	316.1	320.6	4.5	3.72	82.7	AHC; start Tensor tool at 2038 hr; on bottom at 2054 hr; up at 2059 hr
43R	19	2330	320.6	323.2	2.6	1.50	57.7	AHC; start Tensor tool at 2225 hr; on bottom at 2254 hr; up at 2259 hr
44R	20	1000	323.2	329.5	6.3	2.13	33.8	AHC
45R	20	1300	329.5	335.2	5.7	3.40	59.7	AHC
				Cored totals:	278.2	141.43	50.8	
				Drilled totals:	57.0			
				Total:	335.2			

Note: AHC = active heave compensation, NA = not applicable.

Table T2. Summary of the occurrence and characteristics of sedimentary intercalations found within the basalts in the basement Cores 197-1206A-2R to 27R and 40R. (**See table notes.** Continued on next page.)

Core, section, piece, interval (cm)	Depth (mbsf)	Contact	Color	Type	Components	Matrix	Rock name	Interbedded lithologies	Interpretation
197-1206A-									
2R-1 (Piece 1, 0–6)	57.00–57.06	Sharp	N6/	Matrix supported	Miliolid foraminifers	Spar calcite, sulfides (pyrite and/or calcopyrite?)	Calcilutite	Sandstone with bioclast at top (42–43 cm) sand to gravel-sized pebbles	Back reef/bank facies
2R-1 (Piece 3, 42–52)	57.42–57.52	Sharp undulated	N6/	Matrix supported	Miliolid foraminifers, bivalves, gastropods (total = 25%); dark particles (5%–10%)	Calcite, sulfides; barren	Calcilutite	Sandstone with bioclasts at top (42–43 cm) sand to gravel-sized pebbles	Back reef/bank facies to subaerial
4R-1 (Piece 1, 0–5)	66.10–66.15	None	5Y 5/1	—	Sand-sized grains	Microcrystalline/ spar calcite	2-cm subround pebble	—	Not related to the core depth?
4R-1 (Piece 1, 0–5)	66.10–66.15	None	2.5Y 7/1	Cone-shaped macrofossil	Calcareous microfossils (miliolids) and clay particles in adhering material	Silt sized	Fossil	—	Not related to the core depth?
4R-1 (Piece 1, 0–5)	66.10–66.15	None	2.5Y 7/1	Matrix supported	Miliolids	Microcrystalline	3-cm subround pebble	—	Not related to the core depth?
7R-2 (Piece 24, 102–108)	87.22–87.28	Sharp	10YR 8/2 to 7/5B	Matrix supported	Miliolids, bivalves	Carbonates	Limestone with bioclasts and microfossils	—	Back reef/bank facies
7R-2 (Piece 25A, 108–115)	87.28–87.35	Sharp to gradational along the interface	10YR 8/2 to 7/5B	Matrix supported	Miliolids, bivalves, and corals	Spar calcite	Limestone with bioclasts and microfossils	—	Back reef/bank facies
8R-1 (Piece 10, 39–42)	90.79–90.82	Sharp	Gray (2.5Y 5/1)	Matrix supported	Sand-sized rounded volcanic grains	Carbonate-rich cement	Calcilutite	Sandstone	Back reef/beach?
8R-1 (Piece 23, 94–97)	91.34–91.37	Sharp	Light bluish gray (8/5BG)	Matrix to grain supported	$CaCO_3$-rich silt-clay and rounded to subangular grains	Carbonate-rich cement	Finely laminated limestone (95–97 cm)	Fine-grained sandstone (93–95 cm)	Low-energy setting
8R-1 (Piece 26, 104–111)	91.44–91.51	Sharp	Gray (5Y 5/1)	Matrix to grain supported	Miliolids (<5%)	Silty-clay	Siltstone and grainstone	Limestone and calcilutite	Beach deposit?
8R-1 (Piece 29, 120–123)	91.60–91.63	Sharp	Gray (5Y 5/1)	Grain supported	Fossil barren	Spar calcite	Grainstone	Limestone and calcilutite	Beach deposit?
8R-1 (Piece 30, 123–128)	91.63–91.68	Sharp	Gray (5Y 5/1)	Clay supported	$CaCO_3$-rich silt-clay	Silty-clay	Siltstone	Limestone	Beach deposit?
24R-4 (Piece 8, 54–57)	197.67–197.70	Sharp	5Y 5/1 to 10YR 6/1	Matrix supported*	Inorganic calcite (~5%–80%), organic calcite (~5%–50%), pyrite (5%–10%), Fe oxides (~2%–10%), clay (~20%–30%), gypsum (~5%–10%), and feldspar (~Tr–7%)†; miliolids (~40%–60%), rounded lithics (10%), and 20%–30% spar calcite‡	(1) Lime mud; (2) spar calcite	(1) Sandy claystone	(2) Six ~0.4-mm laminations of coarse to medium calcarenite (biosparite**)	Back reef/bank facies to low energy setting
27R-1 (Piece 10, 82–98)	220.62–220.78	Sharp	Greenish gray (5GY 5/1) to dark greenish gray (6/1)		Silt, clay, and miliolid foraminifers (15%)	Calcareous silty-clay	Silty-claystone with microfossils	Lava flow	Back reef/bank facies
27R-1 (Piece 12, 108–112)	220.88–220.92	Gradational	5GY 6/1	Lime mud matrix supported	Miliolids and cylindrical spicula (~15%–30%)	$CaCO_3$-rich clay	Limestone with bioclasts and microfossils (= biomicrite)	Lava flow	Back reef/bank facies

Table T2 (continued).

Core, section, piece, interval (cm)	Depth (mbsf)	Contact	Color	Type	Components	Matrix	Rock name	Interbedded lithologies	Interpretation
27R-1 (Piece 13, 112–117)	220.92–220.97	Sharp	5GY 6/1, and black (2.5/)	Lime mud matrix supported	Silt-sized particles, miliolids (~20%), and volcanic ash-rich grainstone	$CaCO_3$-rich silty clay	Microfossil-rich limestone (= bicrite)	Fine volcaniclastic grainstone	Back reef/bank facies
40R-1, 101–111	307.51–307.61	Gradational	Dark reddish brown (10R 3/4)	Red silty-clay + basalt	Fe oxide–rich, clay mineral, clay, and opaque minerals; basalt	Fe oxide–rich clay	Red claystone	—	Subaerial/weathered flow top
40R-2, 0–150	307.61–309.11	Gradational	Dusky brown (5YR 2/2) to very dusky red (10R 2/2)	Red silty-clay + basalt	Fe oxide–rich, clay mineral, clay, and opaque minerals; basalt	Fe oxide–rich clay	Red claystone	—	Subaerial/weathered flow top
40R-3, 0–77	309.11–309.88	Gradational/ sharp	Dark brown (10YR 2/2)	Red silty-clay + basalt	Fe oxide–rich, clay mineral, clay, and opaque minerals; basalt	Fe oxide–rich clay	Red claystone	—	Subaerial/weathered flow top

Notes: * = the two materials of the thinly layered limestone piece are referred to as sandy claystone and lamination of biosparite. † = semiquantitative percent composition determined from smear slide observation of the lime mud part (N = 4), ‡ = stereoscope microscope observation of the submillimeter layers within Piece 8. ** = Folk's (1962) classification of carbonate textures. — = undefined.

Table T3. Distribution and lithology of basement units, Site 1206. (See table notes. Continued on next page.)

Core, section	Depth (mbsf) Top	Depth (mbsf) Bottom	Unit/ Subunit	Eruption unit*	Unit name	Thickness (m) Curated	Thickness (m) Calculated	Position of unit boundaries in core	Lava type (inferred)	Lobes/ subunits (number)	Notes
197-1206A-											
1W	0.00	57.00	SEI		Fossiliferous vitric-lithic sandstone and breccia	2.31	57.00	The base of Sedimentary Unit 1 is inferred to be at 57.0 mbsf.	Resedimented volcaniclastics rich on unaltered lapilli tephra clast		Sandstone matrix-supported lapilli breccia consisting of basalt lava lithic and unaltered tephra fragments.
2R-1 to 4R-5	57.00	75.10	1	I	Sparsely to moderately olivine-phyric basalt	14.67	16.40	The top of Unit 1 is taken to be at 57.0 mbsf. The Unit 1/2 boundary is inferred to be at 73.4 mbsf (midway between Sections 4R-5 and 5R-1).	Compound pahoehoe	13	Highly vesicular lava with three-fold division and smooth glassy pahoehoe surfaces.
5R-1 to 6R-1	75.10	87.21	2a–2c	I	Hyaloclastite olivine-basalt breccia	6.78	13.81	The top of Unit 2 is at 73.4 mbsf. The Unit 2/3 boundary is in Section 7R-2 (87.21 mbsf).	Flow-foot breccia to Unit 1	1	Hyaloclastite breccia formed by disintegration of lava by quenched fragmentation upon contact with water intercalated with small pillowlike lobes. This unit represents a classic lava delta sequence.
7R-2	87.21	87.33	3		Coralline limestone	0.12	0.12	Thin limestone interbed. The Unit 3/4 boundary is in Section 7R-2 (87.33 mbsf).			Benthic foraminifers—nearshore environment.
7R-2 to 14R-2	87.33	126.65	4	II	Sparsely to highly olivine-phyric basalt	11.57	39.32	The Unit 4/5 boundary is inferred to be at 126.65 mbsf (midway between Sections 14R-2 and 15R-1). Paleomagnetic reversal across Core 8R to 9R??	Compound pahoehoe	>12	Highly vesicular lava with three-fold division and smooth glassy pahoehoe surfaces. It is possible that there is more than one eruption unit in this interval.
15R-1 to 16R-1	126.65	133.72	5	III	Moderately olivine-plagioclase-phyric basalt	4.14	7.07	The Unit 5–6 contact is defined by a flow boundary (thin flow base breccia) at Section 16R-1, 52 cm.	A'a lava?	1	Strongly flow-foliated lava with thin basal breccia.
16R-1 to 19R-1	133.72	155.00	6	IV	Moderately to highly olivine-phyric basalt	12.42	21.28	The Unit 6–7 contact is defined by a distinct change in igneous lithology across lobe margins at Section 19R-1, 120 cm.	Compound pahoehoe	>14	Highly vesicular lava with three-fold division and smooth glassy pahoehoe surfaces. This interval most likely consists of two eruption units.
19R-1 to 21R-1	155.00	172.00	7	V	Aphyric to moderately olivine-phyric basalt	9.32	17.00	The Unit 7–8 contact is defined by a distinct change in volcanic lithology at Section 21R-1, 20 cm.	Compound pahoehoe	5	Highly vesicular lava with three-fold division and smooth glassy pahoehoe surfaces.
21R-1 to 22R-3	172.00	184.73	8a–8o	V	Hyaloclastite olivine basalt breccia and moderately olivine-phyric basalt	10.06	12.73	The primary depositional contact between Units 8 and 9 is at Section 22R-3, 33 cm.	Flow-foot breccia to Unit 7, composed of hyaloclastite breccia and intercalated pillow lava horizons	15	Classic lava delta sequence. Hyaloclastite breccia formed by disintegration of lava by quenched fragmentation upon contact with water and pillows by lava advancing directly into the sea.
22R-3	184.73	185.42	9		Volcaniclastic and sedimentary interbed	0.69	0.69	The primary contact between Units 9 and 10 is at Section 22R-3, 103 cm.	Bedded lithic-vitric sandstone and gravelstone overlying limestone		Coarse-grained nature, cross-bedding, and presence of fossil shell fragments and benthic foraminifers indicate a high-energy nearshore environment. The low maturity of the clast population is indicative of high sedimentation rates.

Table T3 (continued).

Core, section	Depth (mbsf) Top	Depth (mbsf) Bottom	Unit/ Subunit	Eruption unit*	Unit name	Thickness (m) Curated	Thickness (m) Calculated	Position of unit boundaries in core	Lava type (inferred)	Lobes/ subunits (number)	Notes
22R-3 to 25R-2	185.42	206.15	10	VI	Aphyric to sparsely olivine-phyric basalt	12.91	20.73	The Unit 10/11 boundary is inferred to be at 206.15 mbsf (midway between Sections 25R-2 and 26R-1).	Compound pahoehoe	5	Highly vesicular lava with three-fold division and smooth glassy pahoehoe surfaces.
26R-1 to 30R-2	206.15	240.93	11a–11ae	VI	Hyaloclastite basalt breccia and aphyric to sparsely olivine-phyric basalt	15.85	34.78	The primary depositional contact between Units 11 and 12 is at Section 30R-2, 23 cm.	Flow-foot breccia to Unit 10, composed of hyaloclastite breccia and intercalated pillow lava horizons	31	Classic lava delta sequence. Hyaloclastite breccia formed by disintegration of lava by quenched fragmentation upon contact with water and pillows by lava advancing directly into the sea.
30R-2 to 31R-1	240.93	249.00	12		Calcareous lithic-vitric sandstone	3.81	8.07	The Unit 12/13 boundary is placed at Section 31R-1 (Piece 2, 10 cm); detrital limestone on lava.	Sedimentary interbed		Epiclastic sandstone overlying a thin detrital limestone interval. Nearshore depositional environment.
31R-1	249.00	253.70	13	VII	Aphyric to sparsely olivine-phyric basalt	1.07	1.07	The Unit 13/14 boundary is inferred to be at 253.7 mbsf (midway between Sections 31R-1 and 32R-1).	Not possible to determine due to poor recovery		
32R-1 to 34R-2	253.70	271.41	14a–14e	VII	Hyaloclastite basalt breccia and sparsely olivine-phyric basalt	15.85	21.34	The primary depositional contact between Units 14 and 15 is at Section 34R-2, 6 cm.	Flow-foot breccia to Unit 13, composed of hyaloclastite breccia and intercalated pillow lava horizons	5	Classic lava delta sequence. Hyaloclastite breccia formed by disintegration of lava by quenched fragmentation upon contact with water and pillows by lava advancing directly into the sea.
34R-2	271.41	272.45	15		Calcareous grainstone	0.98	1.04	The Unit 15/16 boundary is at Section 34R-2, 104 cm; conformable depositional contact.	Sedimentary interbed		Epiclastic sandstone overlying a thin detrital limestone interval.
34R-2 to 36R-2	272.45	289.01	16		Volcaniclastic grainstone	14.48	16.56	The Unit 16/17 boundary is placed at the top of Section 36R-3.	Sedimentary interbed		Epiclastic sandstone. Nearshore depositional environment.
36R-3 to 40R-1	289.01	307.54	17a–17b	VIII	Highly olivine-phyric basalt	18.58	18.53	The primary depositional contact between Units 14 and 15 is at Section 40R-3, 104 cm.	A'a	2	Picrite basalt.
40R-1 to 40R-3	307.54	309.88	18a		Red-brown weathered flow top with moderately olivine-phyric basalt clasts	2.33	2.34	The Unit 18a/18b boundary is inferred to be at the top of Section 40R-4.	Deeply weathered flow-top rubble		Deeply weathered flow top containing relict and slightly altered spinose and jagged clinker clasts of aphanitic sparsely olivine-phyric basalt.
40R-4 to 41R-2	309.88	313.00	18b	IX	Aphyric basalt	3.06	3.12	The primary contact between Units 18b and 19 is at Section 41R-2, 43 cm.	A'a	1	Aphyric basalt containing microphenocrysts?
41R-2 to 41R-3	313.00	315.04	19		Volcaniclastic basalt breccia	2.04	2.04	The primary contact between Units 19 and 20 is at Section 41R-3, 100 cm.	A'a		Epiclastic breccia (i.e., resedimented basalt detritus).
41R-3	315.04	315.19	20		Volcaniclastic sandstone	0.15	0.15	The primary depositional contact between Units 20 and 21 is placed at Section 41R-3, 115 cm.	Sedimentary interbed		Epiclastic sandstone. Nearshore depositional environment.
41R-3 to 45R-2	315.19	331.68	21	X	Sparsely olivine-plagioclase-phyric basalt	2.04	16.49	The primary depositional contact between Units 21 and 22 is at Section 45R-2, 68 cm.	A'a		Flow-top rubble infiltrated by sand from the above sediment unit.
45R-3 to 45R-2	331.68	335.20	22		Calcareous lithic-vitric sandstone	1.76	3.52	Unit 22 is the deepest, so there is no contact at its base (not reached).	Sedimentary interbed		Epiclastic sandstone. Nearshore depositional environment.

Notes: * = lava units formed in the same eruption.

Table T4. Key structural and morphological features of the basement lava units, Site 1206.

Unit name	Unit/ Subunit	Unit thickness (m)	Eruption unit	Architecture	Pahoehoe		Lower vesicular crust		Lobe interior		Upper vesicular crust		Segregation structure	Breccia		Viscous flow fabric			Lava flow type
					Base	Top	Present	Vesicularity (modal %)	Present	Vesicularity (modal %)	Present	Vesicularity (modal %)		Top	Base	ff	pf	vf	
Sparsely to moderately olivine-phyric basalt	1	16.4	I	L (13)	Y	Y	Y	20–35	Y	3–20	Y	25–35	pv, vc, mv	N	N	N	N		Compound pahoehoe
Hyaloclastite olivine-basalt breccia	2a–2c	13.8	I	(L)	(y)	(y)			Y	10–20									Flow-foot breccia with two coherent lava intervals consisting of pillowlike lobes
Sparsely to highly olivine-phyric basalt	4	39.3	II	L (>12)	Y	Y	Y	30–35	Y	3–25	Y	30–35	vc	N	N	N	N		Compound pahoehoe
Moderately olivine-plagioclase-Phyric basalt	5	7.1	III	S	N	—	y	8	Y	5–8	N			—	Y	Y	N	Y	A'a
Moderately to highly olivine-phyric basalt	6	21.3	IV	L (>14)	Y	Y	Y	30–35	Y	3–15	Y	25–40	vc	N	N	N	N		Compound pahoehoe
Aphyric to moderately olivine-phyric basalt	7	17.0	V	L (7)	—	—	Y	20–35	Y	<15	Y	25–40		N	N	N	N		Compound pahoehoe
Hyaloclastite olivine basalt breccia and moderately olivine-phyric basalt	8a–8o	12.7	V	(L)	(y)	(y)			Y	3–40									Flow-foot breccia with seven intervals consisting of pillowlike lobes; lobe vesicularity decreases downcore
Aphyric to sparsely olivine-phyric basalt	10	20.7	VI	L (5)	—	—	Y	30–35	Y	1–15	Y	30–35	vc, hvs	N	N	N	N		Compound pahoehoe
Hyaloclastite basalt breccia and aphyric to sparsely olivine-phyric basalt	11a–11ae	34.8	VI	(L)	(y)	(y)			Y	3–40									Flow-foot breccia with 15 intervals consisting of pillowlike lobes; lobe vesicularity decreases downcore
Aphyric to sparsely olivine-phyric basalt	13	1.1	VII	—	—	—	—	—	—	—	—	—	—	—	—	—	—	—	Not possible to determine due to poor recovery
Hyaloclastite basalt breccia and sparsely olivine-phyric basalt	14a–14d	21.3	VII	(L)	(y)	(y)			Y	3–20									Flow-foot breccia with 15 intervals consisting of pillowlike lobes; lobe vesicularity decreases downcore
Highly olivine-phyric basalt	17a, b	18.5	VIII	L	N	N	N		Y	<3	N			Y	Y	Y	N	Y	A'a
Aphyric basalt	18b	3.1	IX	S	Y	N	Y	15–25	Y	3–30	Y	15–25	vc	Y	N	N	N	Y	Transitional
Sparsely olivine-plagioclase-phyric basalt	21	16.5	X	S	N	N	N		Y	<3				Y	Y	Y	N	Y	A'a

Notes: ff = flow foliation, pf = crystal fabric (alignment of tabular and lath-shaped plagioclase phenocrysts and groundmass phases), vf = vesicle fabric. L = lobed consisting of multiple flow lobes (number in parenthesis indicates number of flow lobes), S = simple flow consisting of a single lobe (flow unit), — = cannot tell from the recovered core. Y = present as a major component, y = present as a minor component, N = not present. pv = pipe vesicles, vc = vesicle cylinders, mv = megavesicles, hvs = horizontal vesicle sheets (segregation veins).

Table T5. List of cores and recovery, Site 1206.

Core, section	Depth (mbsf) Top	Bottom	Thickness (m) Recovered	Cored	Recovery (%)
197-1206A-					
1W-2	0.00	57.00	2.30	57.00	4.04
2R-2	57.00	58.50	1.62	1.50	108.00
3R-6	58.50	66.10	6.75	7.60	88.82
4R-5	66.10	75.10	5.54	9.00	61.56
5R-2	75.10	79.80	1.89	4.70	40.21
6R-2	79.80	84.70	1.42	4.90	28.98
7R-4	84.70	90.40	3.88	5.70	68.07
8R-3	90.40	94.70	2.60	4.30	60.47
9R-2	94.70	104.40	2.14	9.70	22.06
10R-1	104.40	106.10	0.25	1.70	14.71
11R-1	106.10	114.00	0.12	7.90	1.52
12R-1	114.00	118.70	0.02	4.70	0.43
13R-1	118.70	123.60	0.04	4.90	0.82
14R-2	123.60	128.20	2.02	4.60	43.91
15R-4	128.20	133.20	3.62	5.00	72.40
16R-6	133.20	142.80	6.56	9.60	68.33
17R-2	142.80	152.40	1.94	9.60	20.21
18R-2	152.40	153.80	1.40	1.46	95.89
19R-3	153.80	162.20	3.87	8.40	46.07
20R-4	162.20	171.80	5.22	9.60	54.38
21R-5	171.80	181.40	4.98	9.60	51.88
22R-4	181.40	191.00	3.86	9.60	40.21
23R-1	191.00	192.70	1.13	1.70	66.47
24R-5	192.70	200.60	6.20	7.90	78.48
25R-2	200.60	210.20	2.42	9.60	25.21
26R-3	210.20	219.80	2.73	9.60	28.44
27R-2	219.80	224.00	1.82	4.20	43.33
28R-4	224.00	229.60	4.04	5.60	72.14
29R-3	229.60	239.30	2.48	9.70	25.57
30R-3	239.30	248.90	4.59	9.60	47.81
31R-1	248.90	258.50	0.71	9.60	7.40
32R-3	258.50	268.10	2.50	9.60	26.04
33R-1	268.10	269.90	1.14	1.80	63.33
34R-5	269.90	277.70	6.68	7.80	85.64
35R-6	277.70	287.30	8.17	9.60	85.10
36R-4	287.30	291.90	4.40	4.60	95.65
37R-4	291.90	296.90	4.53	5.00	90.60
38R-5	296.90	301.50	4.81	4.60	104.57
39R-4	301.50	306.50	3.97	5.00	79.40
40R-4	306.50	311.10	4.34	4.60	94.35
41R-4	311.10	316.10	4.12	5.00	82.40
42R-3	316.10	320.60	3.72	4.50	82.67
43R-2	320.60	323.20	1.50	2.60	57.69
44R-2	323.20	329.50	2.13	6.30	33.81
45R-3	329.50	335.20	3.40	5.70	59.65
		Total core:	136.54	320.66	42.58
		Total basement:	118.44	240.86	49.17

Table T6. Statistics on flow types, Site 1206.

Flow type	Number	Average thickness in succession (m)	Lobe thickness of flow type in succession (m)	Cumulative thickness of units (m)	Proportion of volcanic succession (%)
Compound pahoehoe	5	19.1	0.1–7.3	114.7	47.1
Flow-foot breccia	4	20.7	0.1–1.6	82.7	33.9
A'a	3	14.0	6.5–16.5	42.1	17.3
Transitional	1	3.1	3.1	3.1	1.3
Unclassified	1	1.1	1.1	1.1	0.5

Table T7. Summary of the opaque mineralogy of basement rocks, Site 1206. (Continued on next page.)

Basalt unit	Core, section, piece, interval (cm)	Size (μm)	Titanomagnetite description	Estimated modal abundance (%)	Other opaque minerals	Photomicrograph
	197-1206A-					
1	3R-2 (Piece 8, 94–96)	≤80	Skeletal octahedra and dendrites; ilmenite oxidation lamellae are well developed and maghemite is developed along cleavage planes	6–8	Cr spinel inclusions are present in altered olivine phenocrysts; these usually have a titanomagnetite overgrowth, but occasionally are unaltered; no sulfide or Fe oxyhydroxide	1206A-289, 1206A-290, 1206A-291, 1206A-292
1	4R-3 (Piece 4A, 72–74)	≤100	Skeletal octahedra and dendrites (up to 200 μm); slight development of ilmenite oxidation lamellae, but no maghemite	6–8	Cr spinel inclusions are present in olivine; these usually have a titanomagnetite overgrowth, but occasionally are unaltered; no sulfide or Fe oxyhydroxide	1206A-293, 1206A-294, 1206A-295, 1206A-296, 1206A-297, 303, 1206A-304
2c	7R-1 (Piece 9, 123–125)	—	Lobe margin; no titanomagnetite is present	—	Cr spinel inclusions in olivine phenocrysts; glass is now altered to a black-brown amorphous clay; no sulfide or Fe oxyhydroxide	
4	8R-1 (Piece 1, 2–3)	≤30	Skeletal octahedra and dendrites; extensive alteration to maghemite; rare titanomagnetite relicts are present parallel to cleavage planes	2–4	Cr spinel inclusions are present in altered olivine phenocrysts; Fe oxyhydroxide is present; no sulfide	
4	8R-1 (Piece 24, 99–101)	≤30	Skeletal octahedra and dendrites; extensive development of ilmenite oxidation lamellae and alteration to maghemite along cleavage planes and fractures; rare titanomagnetite relicts are present parallel to cleavage planes	2–4	Cr spinel inclusions are present in altered olivine phenocrysts; Fe oxyhydroxide is pervasive; no sulfide	
4	8R-2 (Piece 1, 2–3)	≤30	Skeletal octahedra and dendrites; extensive alteration to maghemite; rare titanomagnetite relicts are present parallel to cleavage planes	2–4	Cr spinel inclusions are present in altered olivine phenocrysts; Fe oxyhydroxide is present; no sulfide	
5	15R-1 (Piece 7A, 72–74)	≤50	Skeletal octahedra; mostly unaltered, but there is some development of ilmenite oxidation lamellae; maghemite is rarely present along fractures	7–9	Cr spinel is present with extensive titanomagnetite overgrowths (e.g., photomicrograph 1206A-323), but not distinguished as inclusions in olivine; no sulfide or Fe oxyhydroxide	1206A-323, 1206A-324
5	15R-3 (Piece 15, 87–89)	≤70	Skeletal octahedra; titanomagnetite is altered to maghemite along cleavage planes and fractures; ilmenite oxidation lamellae are present in unaltered titanomagnetite	5–7	Chromite inclusions are present in clinopyroxene and plagioclase crystals that form glomerocrysts; Fe oxyhydroxide is present in altered olivine phenocrysts; no sulfide	1206A-322, 1206A-325, 1206A-326, 1206A-327
6	16R-4 (Piece 8B, 80–82)	≤60	Anhedral, skeletal dendrites; ilmenite oxidation lamellae are probably present and the titanomagnetite may be partially altered to maghemite; small size and skeletal form makes positive identification difficult	4–6	Cr spinel inclusions are present in altered olivine phenocrysts; most Cr spinel inclusions have been replaced by titanomagnetite; olivine is replaced by Fe oxyhydroxide (iddingsite); no sulfide	1206A-1206A-368, 369, 1206A-370
6	16R-5 (Piece 8, 66–67)	≤20	Anhedral, skeletal dendrites; ilmenite oxidation lamellae are probably present and the titanomagnetite may be partially altered to maghemite; small size and skeletal form makes positive identification difficult	2–4	Largest opaque minerals are the Cr spinel inclusions in altered olivine phenocrysts; most Cr spinel inclusions have been replaced by titanomagnetite; olivine is replaced by Fe oxyhydroxide (iddingsite); no sulfide	1206A-371, 1206A-372, 1206A-373
6	17R-2 (Piece 6, 74–76)	≤100	Skeletal octahedra and dendrites; titanomagnetite is relatively unaltered with only modest development of ilmenite oxidation lamellae; maghemite is rarely developed along fractures	8–10	Cr spinel or chromite inclusions are present in altered olivines and are occasionally replaced by titanomagnetite; Fe oxyhydroxide is present in altered olivine phenocrysts; no sulfide	
6	18R-1 (Piece 4, 49–51)	≤50	Skeletal octahedra and dendrites; titanomagnetite is altered to maghemite along cleavage planes, fractures, and on crystal margins; ilmenite oxidation lamellae are present in unaltered titanomagnetite	4–6	Cr spinel is a discrete phenocryst phase (with thin overgrowths of titanomagnetite) and forms ~1% of the rock; it is also present as inclusions in olivine phenocrysts; no sulfide or Fe oxyhydroxide	1206A-328, 1206A-331, 1206A-332, 1206A-333
6	18R-1 (Piece 4, 80–83)	≤100	Skeletal octahedra and dendrites; development of ilmenite oxidation lamellae is extensive; maghemite is developed along fractures and cleavage planes, but some titanomagnetite crystals are maghemite free	4–6	Cr spinel is a discrete phenocryst phase (with thin overgrowths of titanomagnetite) and forms ~1% of the rock; it is also present as inclusions in olivine phenocrysts; olivine phenocrysts have a rim of Fe oxyhydroxide (iddingsite); no sulfide	1206A-374, 1206A-375, 1206A-376, 1206A-377, 1206A-378, 1206A-379, 1206A-380

Table T7 (continued).

Basalt unit	Core, section, piece, interval (cm)	Size (μm)	Titanomagnetite description	Estimated modal abundance (%)	Other opaque minerals	Photomicrograph
7	19R-3 (Piece 2, 46–48)	10–150	Skeletal octahedra and dendrites; mostly unaltered, but there is some development of ilmenite oxidation lamellae; maghemite is rarely present along fractures	5–7	A minor amount of secondary pyrite is present; no Fe oxyhydroxide	1206A-334
8	21R-5 (Piece 9, 66–68)	—	Lobe margin; no titanomagnetite is present	—	Glass is now altered to a black-brown amorphous clay; no sulfide or Fe oxyhydroxide	
10	24R-3 (Piece 2, 10–12)	10–150	Skeletal octahedra and dendrites; development of ilmenite oxidation lamellae is extensive; maghemite is developed along fractures and cleavage planes, but many titanomagnetite crystals are maghemite free	4–6	No sulfide or Fe oxyhydroxide	1206A-335, 1206A-336
11	28R-1 (Piece 17C, 100–102)	—	Lobe margin; no titanomagnetite is present	—	Cr spinel inclusions are present in altered olivine phenocrysts; glass is now altered to a black-brown amorphous clay; no sulfide or Fe oxyhydroxide	1206A-337
13	31R-1 (Piece 11, 60–63)	≤20	Skeletal octahedra and dendrites; slight development of ilmenite oxidation lamellae; no maghemite	4–6	Cr spinel inclusions are present in altered olivine phenocrysts; olivine is replaced by Fe oxyhydroxide (iddingsite); no sulfide	1206A-339
14	32R-2 (Piece 26, 136–137)	—	Lobe margin; no titanomagnetite is present	—	Glass is now altered to a black-brown amorphous clay; no sulfide or Fe oxyhydroxide	1206A-367
17	38R-1 (Piece 2B, 55–58)	≤50	Skeletal octahedra and dendrites plus anhedral masses; groundmass titanomagnetite is ≤50 μm; where it has replaced Cr spinel phenocrysts, it is between 150–250 μm; extensive development of ilmenite oxidation lamellae; no maghemite alteration	8–10	Cr spinel is present as inclusions in olivine phenocrysts and as discrete phenocrysts (now replaced by titanomagnetite); occasional Cr spinel relicts are present in the larger titanomagnetites; no sulfide or Fe oxyhydroxide	1206A-349, 1206A-350, 1206A-360, 1206A-361, 1206A-362, 1206A-363, 1206A-364
18b	41R-1 (Piece 5A, 22–24)	≤150	Skeletal octahedra and dendrites; ilmenite oxidation lamellae are present; rare maghemite is developed along fractures	7–9	Cr spinel inclusions in altered olivine phenocrysts have mostly been replaced by titanomagnetite; no sulfide or Fe oxyhydroxide	1206A-365, 1206A-366
21	42R-2 (Piece 3, 76–78)	≤30	Subhedral octahedra; slight development of ilmenite oxidation lamellae; no maghemite	9–11	A minor amount of secondary pyrite is present; no Fe oxyhydroxide	1206A-383

Table T8. Whole-rock major and trace element abundances in basement rocks determined by ICP-AES, Hole 1206A. (Continued on next page.)

Core, section:	3R-2	4R-3	7R-1	8R-1	8R-1	8R-2	15R-1	16R-4	16R-5	17R-2
Interval (cm):	94–96	72–74	123–125	2–3	99–101	3–5	72–74	80–82	66–67	74–76
Piece:	8	4A	21	1	24	1	7A	8	8	6
Basement unit:	1	1	2c	4	4	4	5	6	6	6
Eruption unit*:	I	I	I	II	II	II	III	IV	IV	IV
Rock type:	Sparsely to moderately olivine-phyric basalt	Sparsely to moderately olivine-phyric basalt	Hyaloclastite olivine-basalt breccia	Sparsely to highly olivine-phyric basalt	Sparsely to highly olivine-phyric basalt	Sparsely to highly olivine-phyric basalt	Moderately olivine-plagioclase-phyric basalt	Moderately to highly olivine-phyric basalt	Moderately to highly olivine-phyric basalt	Moderately to highly olivine-phyric basalt
Depth (mbsf):	60.84	69.56	85.93	90.42	91.39	91.93	128.92	138.29	139.60	145.04
Major element oxide (wt%):										
SiO_2	48.43	50.15	47.10	49.90	47.18	46.44	48.94	47.11	46.38	47.25
TiO_2	2.32	1.88	2.14	2.16	2.35	2.21	2.35	2.82	2.80	2.56
Al_2O_3	14.36	13.14	14.26	14.78	15.72	14.13	13.74	14.69	13.69	12.82
Fe_2O_3	13.25	13.64	12.20	11.42	13.60	14.20	12.96	12.15	12.83	13.67
MnO	0.14	0.17	0.23	0.10	0.09	0.11	0.17	0.15	0.12	0.16
MgO	7.47	10.61	7.83	8.08	7.10	7.99	7.84	7.56	8.11	9.60
CaO	8.99	8.06	10.05	8.53	7.19	6.53	10.53	10.65	8.48	9.28
Na_2O	3.24	2.73	3.06	2.95	3.20	2.54	2.44	2.70	2.70	2.44
K_2O	0.27	0.30	0.35	0.54	0.78	0.88	0.31	0.35	0.67	0.26
P_2O_5	0.30	0.21	0.35	0.19	0.20	0.15	0.25	0.35	0.37	0.29
Totals:	98.77	100.89	97.58	98.64	97.42	95.17	99.53	98.52	96.14	98.33
LOI	1.67	2.39	2.96	1.96	2.93	4.85	0.01	0.95	3.81	1.59
Mg#	0.55	0.63	0.59	0.61	0.53	0.55	0.57	0.58	0.58	0.61
Trace element (ppm):										
Sr	287	237	364	274	255	158	331	376	378	356
Ba	86.7	76.9	73.5	56.1	59.6	44.6	88.3	47.4	57.5	71.2
Sc	28.2	25.1	28.1	29.6	33.6	32.8	31.7	32.1	30.4	28.4
V	342	287	318	301	304	289	295	335	342	291
Cr	300	435	411	401	419	388	355	330	526	583
Co	52.0	59.2	49.2	51.2	44.8	54.5	54.9	58.7	64.4	56.5
Ni	161	307	199	135	119	134	136	142	237	220
Cu	34.3	80.9	97.8	117	158	145	189	84.9	50.1	95.8
Zn	148	126	191	117	142	121	121	150	250	122
Y	32.6	27.1	37.4	24.5	25.1	21.7	28.9	30.7	29.6	25.9
Zr	168	142	155	128	136	128	152	150	250	173

Notes: * = See Table T3, p. 99, for eruption unit information. LOI = loss on ignition at 1025°C for 4 hr; Mg# = MgO/(MgO+FeO), in molar percent, with FeO calculated (as 90% of total Fe); in all figures all data are renormalized to 100% to correct for variable LOI. This table is also available in ASCII.

Table T8 (continued).

Core, section:	18R-1	19R-3	21R-5	24R-3	28R-1	31R-1	32R-2	38R-1	41R-1	42R-2
Interval (cm):	80–83	46–48	66–68	10–12	100–102	60–63	136–137	55–58	22–24	76–78
Piece:	4	4B	9	2	17C	11	26	2B	5A	3
Basement unit:	6	7	8i	10	11	13	14	17	18b	21
Eruption unit*:	IV	V	V	VI	VI	VI	VII	VIII	IX	X
Rock type:	Moderately to highly olivine-phyric basalt	Aphyric to moderately olivine-phyric basalt	Hyaloclastite olivine basalt breccia and moderately olivine-phyric basalt	Aphyric to sparsely olivine-phyric basalt	Hyaloclastite basalt breccia and aphyric to sparsely olivine-phyric basalt	Calcareous lithic-vitric sandstone	Hyaloclastite basalt breccia and sparsely olivine-phyric basalt	Hyaloclastite basalt breccia and sparsely olivine-phyric basalt	Aphyric basalt	Sparsely phyric basalt
Depth (mbsf):	153.20	157.26	178.39	195.80	225.00	249.50	261.36	297.45	311.32	318.03
Major element oxide (wt%):										
SiO_2	45.25	48.91	47.28	50.07	48.32	49.01	46.64	46.28	48.37	49.06
TiO_2	1.92	2.71	3.14	2.44	2.99	2.53	2.33	1.86	2.84	2.09
Al_2O_3	10.80	14.39	17.17	14.57	15.08	15.41	15.36	10.64	15.49	13.75
Fe_2O_3	10.87	13.19	10.31	14.16	10.51	10.59	10.65	12.15	11.97	12.82
MnO	0.17	0.18	0.23	0.18	0.31	0.12	0.26	0.16	0.17	0.16
MgO	14.76	7.54	7.32	6.64	6.63	7.40	8.09	17.27	6.26	7.33
CaO	8.63	10.91	6.80	10.38	9.10	8.35	10.28	7.25	9.69	9.84
Na_2O	1.56	2.55	3.36	2.70	2.84	2.88	2.75	1.70	3.03	2.45
K_2O	0.13	0.31	0.54	0.31	0.55	0.64	0.43	0.20	0.95	0.20
P_2O_5	0.21	0.26	0.39	0.24	0.40	0.25	0.33	0.17	0.39	0.21
Totals:	1.69	100.95	96.54	101.67	96.73	97.19	97.13	97.69	99.17	97.91
LOI	94.30	0.65	3.66	–0.24	3.35	1.98	2.41	3.23	–0.32	0.34
Mg#	0.53	0.56	0.61	0.51	0.58	0.61	0.63	0.76	0.53	0.56
Trace element (ppm):										
Sr	204	363	395	311	351	327	331	198	357	294
Ba	35.3	90.3	48.0	51.8	44.4	80.5	44.7	93.0	102	069
Sc	27.5	34.2	35.3	29.4	32.8	35.3	31.0	25.0	30.2	27.0
V	241	337	380	332	342	324	296	244	314	263
Cr	768	303	335	260	238	304	308	743	235	277
Co	61.1	61.8	63.3	64.7	79.3	57.7	56.1	69.5	61.4	62.2
Ni	574	115	95.3	84.5	90.8	95.7	120	670	79.9	82.8
Cu	131	52.6	111	95.5	132	103	119	67.3	217	111
Zn	128	120	146	119	225	181	151	120	159	304
Y	19.2	27.8	32.5	27.5	34.3	22.2	28.0	23.4	36.0	29.8
Zr	128	163	206	145	225	181	151	120	159	304

Table T9. Summary of rock magnetic parameters for lava flow samples, Site 1206.

Core, section, interval (cm)	H_{cr} (mT)	MDF_{ARM} (mT)	MDF_{SIRM} (mT)	MDF_{NRM} (mT)
197-1206A-				
3R-2, 99	17.1	11.9	9.6	22.9
4R-5, 55	30.7	30.7	24.6	37.5
7R-4, 64	39.6	28.1	21.3	34.2
9R-1, 29	39.8	22.8	22.2	38.7
15R-2, 108	18.2	11.4	10.6	27.2
16R-5, 75	20.5	18.0	15.6	26.0
18R-1, 56	36.0	20.7	19.6	47.3
22R-1, 117	46.8	41.7	33.7	51.0
27R-1, 47	35.6	32.5	27.6	44.1
28R-1, 97	84.2	57.2	59.3	73.2
33R-1, 26	21.8	31.2	24.2	37.9
41R-2, 26	31.0	16.8	19.0	28.3

Note: H_{cr} = coercive field, MDF = median destructive field, ARM = anhysteretic remanent magnetization, SIRM = saturation isothermal remanent magnetization, NRM = natural remanent magnetization.

Table T10. Shipboard characteristic remanent magnetization inclination averages and summary statistics based on principal component analyses of alternating-field demagnetization data for volcaniclastic samples, Site 1206.

N	Sediment point inc (°)	Inc_{95} (°)	*k*
9	42.5	2.5	443

Notes: *N* = number of determinations within each unit. Sediment point inc = estimation of the inclination mean based on the averaging method of McFadden and Reid (1982). Inc_{95} = estimation of 95% confidence interval of inclination. *k* = estimate of precision parameter.

Table T11. Shipboard characteristic remanent magnetization inclination averages and summary statistics based on principal component analyses of alternating-field demagnetization data for lava flow samples, Site 1206.

Inclination unit	Core, section interval (cm)	Basalt unit	*N*	Point inc (°)	Inc_{95} (°)	*k*
	197-1206A-					
1	2R-1 to 4R-5	1	12	27.2	3.7	137
2	7R-2 to 9R-1	4	7	–35.6	6.1	113
3	9R-2	4	1	33.3	—	—
4	15R-1 to 16R-1, 33	5	4	45.1	11.5	108
5a	16R-1, 77, to 16R-4	6	4	47.6	8.7	189
5b	16R-5 to 17R-2	6	3	6.7	10.8	364
5c	18R-1 to 19R-1, 55	6	3	61.7	22.4	86
6	19R-1, 133, to 20R-4	7	9	53.5	2.4	485
7	22R-3 to 25R-2	10	9	34.1	3.4	245
8	26R-1 to 29R-3	11	5	44.4	10.0	81
10	32R-2 to 33R-1	14	2	37.8	—	2026
11	37R-3 to 40R-1	17	9	44.8	3.2	276
12	40R-4 to 41R-2	18	3	25.8	8.1	350
13	42R-1 to 42R-3	21	3	23.4	—	67
		Average:	14	38.5	9.6	17

Notes: Estimate of dispersion (°), based on the transformation of Cox (1970) = 16.2°. *N* = number of determinations within each unit. Point inc = estimation of the inclination mean based on the averaging method of McFadden and Reid (1982). Inc_{95} = estimation of 95% confidence interval of inclination. *k* = estimate of precision parameter. *N* for "average" values is the estimated number of independent time units (see text). — = not applicable.

Table T12. Magnetic susceptibility measurements, Site 1206.

Core, section, interval (cm)	Depth (mbsf)	Magnetic susceptibility (10^{-6} SI)	Corrected susceptibility (10^{-6} SI)
197-1206A-			
34R-2, 5	271.40	20.0	20.00
34R-2, 10	271.45	48.2	48.20
34R-2, 15	271.50	98.8	98.80
34R-2, 20	271.55	108.6	108.60
34R-2, 25	271.60	124.8	124.80
34R-2, 30	271.65	118.0	118.00
34R-2, 35	271.70	104.4	104.40
34R-2, 40	271.75	90.2	90.20
34R-2, 45	271.80	70.4	70.40
34R-2, 50	271.85	83.2	83.20
34R-2, 55	271.90	90.2	90.20
34R-2, 60	271.95	96.2	96.20
34R-2, 65	272.00	95.4	95.40
34R-2, 70	272.05	85.8	85.80
34R-2, 75	272.10	87.2	87.20
34R-2, 80	272.15	70.2	70.20
34R-2, 85	272.20	60.8	60.80
34R-2, 90	272.25	53.4	53.40
34R-2, 95	272.30	54.8	54.80
34R-2, 100	272.35	92.8	92.80
34R-2, 105	272.40	155.0	155.00
34R-2, 110	272.45	193.0	193.00
34R-2, 115	272.50	213.4	213.40
34R-2, 120	272.55	188.2	188.20
35R-1, 5	277.75	457.4	457.42
35R-1, 10	277.80	499.2	499.25
35R-1, 15	277.85	461.8	461.87
35R-1, 20	277.90	320.2	320.29
35R-1, 25	277.95	313.8	313.91
35R-1, 30	278.00	507.2	507.33
35R-1, 35	278.05	535.4	535.55
35R-1, 40	278.10	517.0	517.17
35R-1, 45	278.15	558.4	558.59
35R-1, 50	278.20	548.6	548.82
35R-1, 55	278.25	487.2	487.44
35R-1, 60	278.30	461.0	461.28
35R-1, 65	278.35	547.6	547.91
35R-1, 70	278.40	546.0	546.35
35R-1, 75	278.45	349.0	349.39
35R-1, 80	278.50	191.6	192.03
35R-1, 85	278.55	229.0	229.47
35R-1, 90	278.60	108.6	109.11
35R-1, 95	278.65	114.2	114.75
35R-2, 5	278.75	130.4	130.42
35R-2, 10	278.80	126.8	126.83
35R-2, 15	278.85	113.8	113.84
35R-2, 20	278.90	98.4	98.46
35R-2, 25	278.95	145.6	145.67
35R-2, 30	279.00	122.8	122.89
35R-2, 35	279.05	113.2	113.30
35R-2, 40	279.10	93.6	93.72
35R-2, 45	279.15	133.4	133.53
35R-2, 50	279.20	122.2	122.35
35R-2, 55	279.25	103.4	103.56
35R-2, 60	279.30	78.2	78.39
35R-2, 65	279.35	79.0	79.21
35R-2, 70	279.40	87.0	87.24
35R-2, 75	279.45	91.0	91.26
35R-2, 80	279.50	65.6	65.89
35R-2, 85	279.55	71.8	72.12
35R-2, 90	279.60	80.4	80.74
35R-2, 95	279.65	241.4	241.77
35R-2, 100	279.70	440.0	440.40
35R-2, 105	279.75	466.6	467.02
35R-2, 110	279.80	320.8	321.25
35R-3, 5	279.86	372.6	372.61
35R-3, 10	279.91	477.2	477.23
35R-3, 15	279.96	483.0	483.04
35R-3, 20	280.01	483.6	483.65
35R-3, 25	280.06	457.2	457.26
35R-3, 30	280.11	464.2	464.28
35R-3, 35	280.16	458.6	458.69
35R-3, 40	280.21	454.8	454.90
35R-3, 45	280.26	365.6	365.71
35R-3, 50	280.31	407.8	407.93
35R-3, 55	280.36	230.4	230.54
35R-3, 60	280.41	246.8	246.96
35R-3, 65	280.46	208.4	208.58
35R-3, 70	280.51	252.2	252.41
35R-3, 75	280.56	422.2	422.43
35R-3, 80	280.61	793.2	793.45
35R-3, 85	280.66	742.4	742.67
35R-3, 90	280.71	1053.2	1053.50
35R-3, 95	280.76	1062.0	1062.32
35R-3, 100	280.81	782.8	783.14
35R-3, 105	280.86	1058.4	1058.76
35R-3, 110	280.91	1152.4	1152.79
35R-3, 115	280.96	831.2	831.61
35R-3, 120	281.01	707.4	707.83
35R-3, 125	281.06	575.6	576.08
35R-3, 130	281.11	544.6	545.10
35R-3, 135	281.16	736.2	736.74
35R-3, 140	281.21	825.6	826.17
35R-4, 5	281.36	774.4	774.42
35R-4, 10	281.41	909.8	909.83
35R-4, 15	281.46	966.2	966.24
35R-4, 20	281.51	993.0	993.06
35R-4, 25	281.56	1027.8	1027.87
35R-4, 30	281.61	1072.8	1072.88
35R-4, 35	281.66	858.6	858.70
35R-4, 40	281.71	690.8	690.91
35R-4, 45	281.76	628.2	628.33
35R-4, 50	281.81	659.4	659.54
35R-4, 55	281.86	647.0	647.15
35R-4, 60	281.91	538.0	538.18
35R-4, 65	281.96	633.0	633.20
35R-4, 70	282.01	583.2	583.43
35R-4, 75	282.06	709.6	709.85
35R-4, 80	282.11	745.2	745.48
35R-4, 85	282.16	743.6	743.90
35R-4, 90	282.21	737.2	737.53
35R-4, 95	282.26	746.2	746.55
35R-4, 100	282.31	749.4	749.78
35R-4, 105	282.36	785.0	785.40
35R-4, 110	282.41	780.0	780.43
35R-4, 115	282.46	765.6	766.05
35R-4, 120	282.51	680.0	680.48
35R-4, 125	282.56	709.2	709.73
35R-4, 130	282.61	704.0	704.55
35R-4, 135	282.66	711.8	712.40
35R-4, 140	282.71	689.6	690.23
35R-4, 145	282.76	509.4	510.07
35R-5, 5	282.86	547.0	546.99
35R-5, 10	282.91	655.0	654.98
35R-5, 15	282.96	595.6	595.57
35R-5, 20	283.01	531.4	531.37
35R-5, 25	283.06	570.0	569.96
35R-5, 30	283.11	570.2	570.15
35R-5, 35	283.16	572.4	572.34
35R-5, 40	283.21	450.6	450.53
35R-5, 45	283.26	482.0	481.92
35R-5, 50	283.31	551.4	551.32

Note: Only a portion of this table appears here. The complete table is available in **ASCII.**

Table T13. GRA bulk density measurements, Site 1206.

Core, section, interval (cm)	Depth (mbsf)	Bulk density (g/cm^3)
197-1206A-		
34R-2, 5	271.40	0.932
34R-2, 10	271.45	1.936
34R-2, 15	271.50	2.013
34R-2, 20	271.55	1.986
34R-2, 25	271.60	1.964
34R-2, 30	271.65	1.844
34R-2, 35	271.70	1.641
34R-2, 40	271.75	1.601
34R-2, 45	271.80	1.774
34R-2, 50	271.85	1.838
34R-2, 55	271.90	1.869
34R-2, 60	271.95	1.850
34R-2, 65	272.00	1.859
34R-2, 70	272.05	–0.689
34R-2, 75	272.10	1.938
34R-2, 80	272.15	2.022
34R-2, 85	272.20	1.426
34R-2, 90	272.25	0.619
34R-2, 95	272.30	0.027
34R-2, 100	272.35	0.862
34R-2, 105	272.40	1.580
34R-2, 110	272.45	2.081
34R-2, 115	272.50	2.016
34R-2, 120	272.55	1.895
35R-1, 5	277.75	2.047
35R-1, 10	277.80	2.051
35R-1, 15	277.85	2.111
35R-1, 20	277.90	1.150
35R-1, 25	277.95	0.651
35R-1, 30	278.00	1.996
35R-1, 35	278.05	2.036
35R-1, 40	278.10	2.006
35R-1, 45	278.15	2.038
35R-1, 50	278.20	2.016
35R-1, 55	278.25	2.002
35R-1, 60	278.30	2.038
35R-1, 65	278.35	2.036
35R-1, 70	278.40	2.060
35R-1, 75	278.45	0.715
35R-1, 80	278.50	1.978
35R-1, 85	278.55	1.986
35R-1, 90	278.60	1.461
35R-1, 95	278.65	1.457
35R-2, 5	278.75	1.988
35R-2, 10	278.80	1.434
35R-2, 15	278.85	1.867
35R-2, 20	278.90	1.708
35R-2, 25	278.95	0.783
35R-2, 30	279.00	1.366
35R-2, 35	279.05	1.181
35R-2, 40	279.10	–0.429
35R-2, 45	279.15	1.767
35R-2, 50	279.20	1.943
35R-2, 55	279.25	1.949
35R-2, 60	279.30	0.655
35R-2, 65	279.35	1.588
35R-2, 70	279.40	1.923
35R-2, 75	279.45	1.899
35R-2, 80	279.50	0.301
35R-2, 85	279.55	1.620
35R-2, 90	279.60	1.425
35R-2, 95	279.65	1.933
35R-2, 100	279.70	2.088
35R-2, 105	279.75	2.058
35R-2, 110	279.80	1.890
35R-3, 5	279.86	1.951
35R-3, 10	279.91	2.003
35R-3, 15	279.96	1.987
35R-3, 20	280.01	1.990
35R-3, 25	280.06	1.955
35R-3, 30	280.11	1.953
35R-3, 35	280.16	1.987
35R-3, 40	280.21	1.958
35R-3, 45	280.26	0.903
35R-3, 50	280.31	2.007
35R-3, 55	280.36	1.054
35R-3, 60	280.41	1.036
35R-3, 65	280.46	1.893
35R-3, 70	280.51	1.827
35R-3, 75	280.56	1.824
35R-3, 80	280.61	2.082
35R-3, 85	280.66	1.763
35R-3, 90	280.71	2.081
35R-3, 95	280.76	2.033
35R-3, 100	280.81	1.850
35R-3, 105	280.86	2.113
35R-3, 110	280.91	2.061
35R-3, 115	280.96	1.969
35R-3, 120	281.01	–0.103
35R-3, 125	281.06	2.007
35R-3, 130	281.11	1.745
35R-3, 135	281.16	1.884
35R-3, 140	281.21	2.097
35R-4, 5	281.36	2.061
35R-4, 10	281.41	1.107
35R-4, 15	281.46	2.044
35R-4, 20	281.51	2.184
35R-4, 25	281.56	1.653
35R-4, 30	281.61	1.863
35R-4, 35	281.66	1.541
35R-4, 40	281.71	1.884
35R-4, 45	281.76	2.036
35R-4, 50	281.81	2.034
35R-4, 55	281.86	2.063
35R-4, 60	281.91	1.912
35R-4, 65	281.96	2.066
35R-4, 70	282.01	1.675
35R-4, 75	282.06	2.029
35R-4, 80	282.11	1.946
35R-4, 85	282.16	1.870
35R-4, 90	282.21	1.924
35R-4, 95	282.26	1.896
35R-4, 100	282.31	1.869
35R-4, 105	282.36	1.843
35R-4, 110	282.41	1.985
35R-4, 115	282.46	1.989
35R-4, 120	282.51	1.848
35R-4, 125	282.56	1.908
35R-4, 130	282.61	1.932
35R-4, 135	282.66	1.995
35R-4, 140	282.71	2.029
35R-4, 145	282.76	1.864
35R-5, 5	282.86	1.844
35R-5, 10	282.91	1.778
35R-5, 15	282.96	1.939
35R-5, 20	283.01	1.969
35R-5, 25	283.06	1.929
35R-5, 30	283.11	1.616
35R-5, 35	283.16	2.004
35R-5, 40	283.21	1.824
35R-5, 45	283.26	1.827
35R-5, 50	283.31	1.998
35R-5, 55	283.36	1.916
35R-5, 60	283.41	1.873
35R-5, 65	283.46	1.982
35R-5, 70	283.51	1.944
35R-5, 75	283.56	1.968
35R-5, 80	283.61	1.890
35R-5, 85	283.66	1.111
35R-5, 90	283.71	1.486
35R-5, 95	283.76	2.103
35R-5, 100	283.81	1.967
35R-5, 105	283.86	1.995
35R-5, 110	283.91	1.964
35R-5, 115	283.96	1.905
35R-5, 120	284.01	1.821
35R-5, 125	284.06	1.755
35R-5, 130	284.11	1.806
35R-5, 135	284.16	1.890
35R-5, 140	284.21	1.810
35R-6, 5	284.36	2.122
35R-6, 10	284.41	1.930
35R-6, 15	284.46	2.098
35R-6, 20	284.51	1.899
35R-6, 25	284.56	1.975
35R-6, 30	284.61	1.465
35R-6, 35	284.66	2.161
35R-6, 40	284.71	1.946
35R-6, 45	284.76	1.803
35R-6, 50	284.81	1.819
35R-6, 55	284.86	1.849
35R-6, 60	284.91	1.874
35R-6, 65	284.96	1.826
35R-6, 70	285.01	1.879
35R-6, 75	285.06	1.880
35R-6, 80	285.11	1.851
35R-6, 85	285.16	1.858
35R-6, 90	285.21	1.873
35R-6, 95	285.26	1.883
35R-6, 100	285.31	1.902
35R-6, 105	285.36	1.889
35R-6, 110	285.41	1.886
35R-6, 115	285.46	1.885
35R-6, 120	285.51	1.809
35R-6, 125	285.56	1.642
35R-6, 130	285.61	1.814
35R-6, 135	285.66	1.753
35R-6, 140	285.71	0.462

Note: This table is also available in **ASCII.**

Table T14. Natural gamma ray measurements, Site 1206.

Core, section, interval (cm)	Depth (mbsf)	Corrected counts (cps)	Total counts (cps)
197-1206A-			
2R-1, 10	57.10	11.43	27.30
2R-1, 20	57.20	9.01	24.88
2R-1, 30	57.30	8.46	24.33
2R-1, 40	57.40	11.53	27.40
2R-1, 50	57.50	18.41	34.28
2R-1, 60	57.60	8.35	24.22
2R-1, 70	57.70	2.66	18.53
2R-1, 80	57.80	2.06	17.93
2R-1, 90	57.90	2.60	18.47
2R-1, 100	58.00	3.93	19.80
2R-1, 110	58.10	6.88	22.75
2R-1, 120	58.20	5.05	20.92
2R-2, 10	58.33	12.48	28.35
2R-2, 20	58.43	11.58	27.45
2R-2, 30	58.53	9.05	24.92
2R-2, 40	58.63	10.80	26.67
3R-1, 10	58.60	4.61	20.48
3R-1, 20	58.70	2.35	18.22
3R-1, 40	58.90	3.16	19.03
3R-1, 60	59.10	1.96	17.83
3R-1, 70	59.20	5.80	21.67
3R-1, 100	59.50	3.70	19.57
3R-1, 120	59.70	2.73	18.60
3R-1, 130	59.80	3.18	19.05
3R-2, 10	60.00	2.86	18.73
3R-2, 40	60.30	2.90	18.77
3R-2, 50	60.40	0.88	16.75
3R-2, 60	60.50	1.81	17.68
3R-2, 70	60.60	3.11	18.98
3R-2, 80	60.70	1.55	17.42
3R-2, 100	60.90	2.26	18.13
3R-2, 110	61.00	2.53	18.40
3R-2, 130	61.20	3.40	19.27
3R-3, 10	61.45	2.38	18.25
3R-3, 20	61.55	3.80	19.67
3R-3, 30	61.65	3.16	19.03
3R-3, 40	61.75	3.65	19.52
3R-3, 50	61.85	4.33	20.20
3R-3, 80	62.15	3.38	19.25
3R-3, 90	62.25	5.38	21.25
3R-3, 100	62.35	4.56	20.43
3R-3, 120	62.55	4.98	20.85
3R-3, 130	62.65	4.53	20.40
3R-4, 10	62.93	1.70	17.57
3R-4, 20	63.03	4.40	20.27
3R-4, 30	63.13	3.08	18.95
3R-4, 50	63.33	3.51	19.38
3R-4, 60	63.43	2.10	17.97
3R-4, 70	63.53	3.41	19.28
3R-4, 80	63.63	3.28	19.15
3R-4, 90	63.73	3.30	19.17
3R-4, 110	63.93	2.93	18.80
3R-4, 130	64.13	3.23	19.10
3R-5, 10	64.43	4.21	20.08
3R-5, 20	64.53	3.60	19.47
3R-5, 30	64.63	6.00	21.87
3R-5, 50	64.83	4.40	20.27
3R-5, 60	64.93	3.68	19.55
3R-5, 70	65.03	4.33	20.20
3R-5, 90	65.23	0.88	16.75
3R-5, 100	65.33	1.90	17.77
3R-5, 110	65.43	1.80	17.67
3R-5, 120	65.53	4.08	19.95
3R-6, 10	65.93	2.00	17.87
3R-6, 20	66.03	4.50	20.37
3R-6, 40	66.23	8.53	24.40
4R-1, 10	66.20	2.51	18.38
4R-1, 20	66.30	4.48	20.35
4R-1, 30	66.40	4.05	19.92
4R-1, 40	66.50	4.00	19.87
4R-1, 50	66.60	4.03	19.90
4R-1, 60	66.70	0.00	15.32
4R-1, 70	66.80	2.53	18.40
4R-1, 80	66.90	3.78	19.65
4R-1, 90	67.00	4.10	19.97
4R-1, 100	67.10	2.91	18.78
4R-1, 110	67.20	2.98	18.85
4R-1, 120	67.30	2.98	18.85
4R-1, 130	67.40	4.60	20.47
4R-2, 10	67.58	1.66	17.53
4R-2, 30	67.78	2.66	18.53
4R-2, 50	67.98	2.20	18.07
4R-2, 70	68.18	1.48	17.35
4R-2, 90	68.38	3.36	19.23
4R-2, 100	68.48	2.46	18.33
4R-2, 120	68.68	2.48	18.35
4R-2, 130	68.78	2.81	18.68
4R-3, 10	68.94	1.58	17.45
4R-3, 20	69.04	1.98	17.85
4R-3, 50	69.34	1.41	17.28
4R-3, 60	69.44	1.91	17.78
4R-3, 70	69.54	0.21	16.08
4R-3, 80	69.64	0.51	16.38
4R-3, 90	69.74	0.96	16.83
4R-3, 100	69.84	1.60	17.47
4R-3, 110	69.94	0.00	15.42
4R-3, 120	70.04	0.61	16.48
4R-3, 130	70.14	0.30	16.17
4R-4, 10	70.39	1.80	17.67
4R-4, 20	70.49	1.76	17.63
4R-4, 30	70.59	2.43	18.30
4R-4, 40	70.69	3.25	19.12
4R-4, 60	70.89	2.30	18.17
4R-4, 70	70.99	2.51	18.38
4R-4, 90	71.19	0.00	15.87
4R-4, 110	71.39	2.41	18.28
4R-4, 120	71.49	1.48	17.35
4R-4, 130	71.59	2.28	18.15
4R-5, 10	71.80	4.95	20.82
4R-5, 20	71.90	3.50	19.37
4R-5, 40	72.10	1.90	17.77
4R-5, 50	72.20	1.65	17.52
4R-5, 60	72.30	3.08	18.95
4R-5, 100	72.70	11.65	27.52
5R-1, 20	75.30	1.36	17.23
5R-1, 40	75.50	2.55	18.42
5R-1, 70	75.80	2.85	18.72
5R-1, 80	75.90	1.93	17.80
5R-1, 100	76.10	1.81	17.68
5R-1, 130	76.40	0.00	15.02
5R-2, 20	76.80	0.00	15.13
5R-2, 40	77.00	1.01	16.88
5R-2, 50	77.10	0.05	15.92
5R-2, 60	77.20	1.08	16.95
5R-2, 70	77.30	2.81	18.68
6R-1, 10	79.90	0.43	16.30
6R-1, 40	80.20	2.50	18.37
6R-1, 70	80.50	3.06	18.93
6R-1, 80	80.60	1.51	17.38
6R-1, 110	80.90	0.31	16.18
6R-1, 120	81.00	1.16	17.03
6R-2, 20	81.50	2.21	18.08
6R-2, 30	81.60	4.15	20.02
7R-1, 10	84.80	1.63	17.50
7R-1, 30	85.00	0.00	14.68
7R-1, 40	85.10	0.73	16.60
7R-1, 60	85.30	1.78	17.65
7R-1, 70	85.40	2.36	18.23
7R-1, 90	85.60	0.00	15.78
7R-1, 100	85.70	1.66	17.53
7R-1, 110	85.80	1.21	17.08
7R-1, 120	85.90	0.76	16.63
7R-1, 130	86.00	1.55	17.42
7R-2, 20	86.40	0.41	16.28
7R-2, 30	86.50	1.21	17.08
7R-2, 40	86.60	3.38	19.25
7R-2, 60	86.80	1.90	17.77
7R-2, 80	87.00	3.56	19.43
7R-2, 110	87.30	1.43	17.30
7R-2, 120	87.40	3.31	19.18
7R-3, 20	87.85	6.28	22.15
7R-3, 30	87.95	2.28	18.15
7R-3, 40	88.05	1.25	17.12
7R-3, 70	88.35	2.26	18.13
7R-3, 80	88.45	3.30	19.17
7R-3, 90	88.55	3.13	19.00
7R-3, 100	88.65	3.86	19.73
7R-3, 110	88.75	1.41	17.28
7R-3, 130	88.95	2.41	18.28
7R-4, 10	89.11	0.98	16.85
7R-4, 30	89.31	0.88	16.75
7R-4, 40	89.41	0.00	14.85
7R-4, 50	89.51	1.25	17.12
8R-1, 60	91.00	2.31	18.18
8R-1, 70	91.10	3.23	19.10
8R-1, 80	91.20	2.48	18.35
8R-1, 90	91.30	0.00	15.82
8R-1, 100	91.40	1.76	17.63
8R-1, 110	91.50	0.43	16.30
8R-1, 130	91.70	0.83	16.70
8R-2, 40	92.30	2.00	17.87
8R-2, 50	92.40	0.00	15.07
8R-2, 60	92.50	0.55	16.42
8R-2, 70	92.60	1.08	16.95
8R-2, 80	92.70	1.63	17.50
8R-2, 100	92.90	1.68	17.55
8R-2, 130	93.20	4.65	20.52
8R-3, 20	93.56	0.56	16.43
8R-3, 50	93.86	0.65	16.52
8R-3, 60	93.96	2.20	18.07
8R-3, 70	94.06	5.25	21.12
9R-1, 10	94.80	0.38	16.25
9R-1, 20	94.90	0.00	15.48
9R-1, 30	95.00	2.25	18.12
9R-1, 40	95.10	1.96	17.83
9R-1, 70	95.40	0.00	15.30
9R-1, 90	95.60	3.56	19.43
9R-1, 110	95.80	0.00	14.70
9R-1, 130	96.00	0.35	16.22
9R-2, 10	96.30	0.00	15.53
9R-2, 60	96.80	0.26	16.13
9R-2, 80	97.00	0.00	15.78
9R-2, 90	97.10	1.23	17.10
9R-2, 120	97.40	0.61	16.48
9R-2, 130	97.50	0.00	15.27
10R-1, 10	104.50	0.05	15.92
10R-1, 20	104.60	5.10	20.97
11R-1, 10	106.20	5.53	21.40
14R-1, 20	123.80	1.30	17.17

Note: Only a portion of this table appears here. The complete table is available in ASCII.

Table T15. Thermal conductivity measurements, Site 1206.

Core, section, interval (cm)	Depth (mbsf)	Thermal conductivity (W/[m·K])	Rock type
197-1206A-			
2R-1, 21–35	57.21	1.292	B
3R-3, 38–51	61.73	1.391	B
4R-3, 93–105	69.77	1.703	B
5R-2, 29–43	76.89	0.960	V
6R-1, 89–97	80.69	1.419	V
7R-4, 39–59	89.40	1.492	B
8R-2, 123–142	93.13	1.057	B
9R-2, 84–98	97.04	1.630	B
10R-1, 0–16	104.40	2.052	B
11R-1, 0–12	106.10	1.928	B
15R-3, 8–21	131.28	1.783	B
16R-1, 28–50	133.48	1.699	B
17R-2, 38–48	144.68	1.373	B
18R-1, 54–64	152.94	2.013	B
19R-3, 123–138	158.03	1.608	B
20R-4, 57–69	167.10	1.230	B
21R-4, 17–33	176.40	1.001	V
22R-1, 28–43	181.68	1.298	V
23R-1, 96–113	191.96	1.641	B
24R-3, 4–14	195.74	1.814	B
25R-1, 10–38	200.70	1.632	B
26R-1, 14–24	210.34	1.455	B
27R-2, 31–42	221.58	1.336	B
28R-1, 55–74	224.55	1.421	B
29R-3, 0–19	232.47	1.548	B
30R-2, 34–51	241.04	1.171	S
31R-1, 22–32	249.12	1.424	B
32R-2, 44–57	260.44	1.474	B
33R-1, 34–46	268.44	1.406	B
34R-3, 54–65	273.15	1.179	S
35R-4, 0–10	281.31	1.542	S
36R-1, 45–64	287.75	1.601	S
37R-3, 105–116	295.46	1.786	B
38R-1, 57–69	297.47	2.198	B
39R-3, 104–116	304.83	2.283	B
40R-1, 101–111	307.51	1.076	F
41R-3, 65–77	314.69	1.122	V
42R-3, 38–51	319.02	1.750	B
43R-1, 64–72	321.24	1.787	B
44R-2, 109–119	325.79	1.565	B
45R-2, 111–128	332.11	1.076	S

Notes: B = basalt, V = volcaniclastic, S = sediment, F = weathered lava flow top. This table is also available in **ASCII.**

Table T16. Index properties, Site 1206.

Core, section, interval (cm)	Depth (mbsf)	Water content (%)		Density (g/cm^3)			Porosity (%)	Void ratio
		Bulk	Dry	Bulk	Dry	Grain		
197-1206A-								
1W-1, 96–98	0.96	19.7	24.5	2.11	1.69	2.85	40.6	0.68
1W-2, 60–62	1.75	19.7	24.5	2.11	1.69	2.85	40.5	0.68
2R-1, 85–87	57.85	4.8	5.0	2.81	2.67	3.08	13.1	0.15
3R-4, 59–61	63.42	7.6	8.2	2.61	2.41	2.99	19.3	0.24
4R-4, 31–33	70.60	11.5	13.0	2.44	2.16	2.98	27.4	0.38
5R-1, 90–92	76.00	16.0	19.1	2.21	1.86	2.84	34.6	0.53
6R-1, 118–120	80.98	16.0	19.1	2.21	1.85	2.83	34.5	0.53
7R-4, 64–66	89.65	6.4	6.8	2.67	2.50	3.00	16.7	0.20
8R-3, 72–74	94.08	6.2	6.6	2.72	2.55	3.05	16.4	0.20
9R-1, 30–32	95.00	8.3	9.0	2.65	2.43	3.09	21.4	0.27
15R-2, 109–111	130.79	4.8	5.0	2.85	2.71	3.13	13.2	0.15
16R-5, 77–79	139.71	9.1	10.0	2.55	2.32	3.00	22.7	0.29
17R-2, 33–35	144.63	11.0	12.3	2.46	2.19	2.98	26.4	0.36
18R-1, 51–53	152.91	2.4	2.5	2.87	2.80	3.01	6.8	0.07
19R-2, 104–106	156.34	6.5	6.9	2.77	2.59	3.14	17.5	0.21
20R-3, 62–64	165.65	3.8	3.9	2.77	2.67	2.97	10.2	0.11
21R-4, 60–62	176.83	21.6	27.6	2.03	1.59	2.78	42.8	0.75
22R-1, 116–118	182.56	7.7	8.4	2.65	2.44	3.06	20.0	0.25
22R-2, 101–107	183.90	17.6	21.4	2.23	1.84	2.99	38.4	0.62
23R-1, 82–88	191.82	2.5	2.6	2.87	2.79	3.00	7.0	0.08
24R-3, 115–117	196.85	4.7	4.9	2.79	2.66	3.05	12.7	0.15
25R-1, 41–43	201.01	3.9	4.1	2.90	2.79	3.13	11.0	0.12
26R-1, 33–35	210.53	9.1	10.0	2.50	2.27	2.93	22.3	0.29
27R-1, 46–48	220.26	8.0	8.7	2.65	2.43	3.07	20.8	0.26
28R-1, 97–99	224.97	5.9	6.2	2.62	2.47	2.91	15.0	0.18
28R-3, 110–112	227.69	19.8	24.7	2.02	1.62	2.66	39.1	0.64
29R-1, 79–81	230.39	4.4	4.6	2.81	2.68	3.06	12.2	0.14
30R-4, 107–109	244.57	24.3	32.1	1.99	1.51	2.86	47.3	0.90
31R-1, 77–102	249.67	6.0	6.4	2.68	2.52	2.99	15.7	0.19
32R-2, 93–97	260.93	20.0	25.1	2.00	1.60	2.64	39.2	0.64
33R-1, 27–29	268.37	7.7	8.3	2.57	2.37	2.94	19.2	0.24
34R-2, 90–92	272.25	21.0	26.6	2.04	1.61	2.78	41.9	0.72
34R-3, 88–90	273.49	19.9	24.8	2.09	1.68	2.83	40.7	0.69
34R-4, 47–49	274.55	16.1	19.1	2.21	1.86	2.85	34.7	0.53
34R-5, 72–74	276.23	20.9	26.4	2.08	1.65	2.86	42.4	0.74
35R-1, 30–32	278.00	18.6	22.8	2.15	1.75	2.87	39.0	0.64
35R-2, 63–65	279.33	20.4	25.6	2.04	1.62	2.73	40.6	0.68
35R-3, 56–58	280.37	21.5	27.4	2.06	1.62	2.85	43.3	0.76
35R-4, 70–72	282.01	20.9	26.4	2.04	1.62	2.77	41.6	0.71
35R-5, 54–56	283.35	17.5	21.2	2.13	1.76	2.77	36.4	0.57
35R-6, 92–94	285.23	22.8	29.6	2.02	1.56	2.85	45.1	0.82
36R-1, 14–16	287.44	22.1	28.4	2.01	1.57	2.77	43.5	0.77
36R-3, 79–81	289.80	3.4	3.6	2.79	2.70	2.97	9.4	0.10
37R-1, 84–86	292.74	3.6	3.7	2.80	2.70	3.00	9.8	0.11
37R-4, 0–5	295.91	9.0	9.9	2.51	2.28	2.93	22.2	0.28
38R-3, 60–62	299.14	1.8	1.9	2.92	2.87	3.03	5.2	0.05
39R-3, 128–133	305.07	2.2	2.3	2.91	2.85	3.04	6.3	0.07
40R-1, 35–37	306.85	2.3	2.4	2.98	2.91	3.12	6.8	0.07
40R-2, 50–52	308.11	23.9	31.4	1.98	1.51	2.80	46.2	0.86
40R-3, 24–26	309.35	26.1	35.4	1.93	1.43	2.82	49.4	0.98
40R-4, 32–34	310.20	7.3	7.8	2.71	2.51	3.11	19.2	0.24
41R-1, 46–48	311.56	4.5	4.7	2.84	2.71	3.10	12.5	0.14
42R-3, 70–72	319.34	2.9	3.0	2.88	2.79	3.05	8.3	0.09
43R-1, 85–87	321.45	4.7	4.9	2.72	2.59	2.96	12.5	0.14
44R-1, 88–91	324.08	2.1	2.2	2.87	2.81	2.99	6.0	0.06

Note: This table is also available in **ASCII.**

Table T17. Compressional wave velocity measurements, Site 1206.

Core, section interval (cm)	Depth (mbsf)	Direction	Velocity (m/s)
197-1206A-			
1W-1, 50	0.50	x	3452.1
1W-2, 101	2.16	x	3041.3
2R-1, 85	57.85	x	4571.3
2R-1, 85	57.85	z	4573.2
2R-1, 116	58.16	x	3990.6
2R-1, 116	58.16	z	3739.0
2R-2, 27	58.50	x	3634.6
2R-2, 27	58.50	z	3884.2
3R-1, 70	59.20	x	3916.9
3R-1, 70	59.20	z	3950.2
3R-2, 100	60.90	x	4690.6
3R-2, 100	60.90	z	4524.4
3R-3, 41	61.76	x	4866.1
3R-3, 41	61.76	z	3795.4
3R-4, 60	63.43	x	4051.6
3R-4, 60	63.43	z	3989.5
3R-5, 116	65.49	x	4383.2
3R-5, 116	65.49	z	4546.2
3R-6, 19	66.02	x	4118.0
3R-6, 19	66.02	z	3916.8
4R-1, 43	66.53	x	4365.2
4R-1, 43	66.53	z	4116.9
4R-2, 100	68.48	x	3957.4
4R-2, 100	68.48	z	3796.0
4R-3, 70	69.54	x	4588.9
4R-3, 70	69.54	z	4754.5
4R-4, 32	70.61	x	3977.9
4R-4, 32	70.61	z	3858.0
4R-5, 55	72.25	x	4094.7
4R-5, 55	72.25	z	3691.2
7R-2, 118	87.38	x	3640.9
7R-2, 118	87.38	z	3565.3
7R-3, 39	88.04	x	3994.8
7R-3, 39	88.04	z	4004.2
7R-4, 64	89.65	x	4159.2
7R-4, 64	89.65	z	4135.4
8R-1, 147	91.87	x	3010.1
8R-1, 147	91.87	z	3099.9
8R-2, 127	93.17	x	2512.7
8R-2, 127	93.17	z	2329.4
8R-3, 73	94.09	x	3878.9
8R-3, 73	94.09	z	3907.5
9R-1, 29	94.99	x	4001.9
9R-1, 29	94.99	z	4079.5
9R-2, 110	97.30	x	4379.1
9R-2, 110	97.30	z	4494.2
15R-1, 58	128.78	x	5131.4
15R-1, 58	128.78	z	5100.2
15R-2, 108	130.78	x	4620.1
15R-2, 108	130.78	y	4761.1
15R-3, 118	132.38	x	5092.8
15R-3, 118	132.38	z	5059.7
16R-1, 33	133.53	x	4903.9
16R-1, 33	133.53	z	4909.7
16R-1, 77	133.97	x	3753.0
16R-1, 77	133.97	y	3668.9
16R-2, 11	134.78	x	4324.2
16R-2, 11	134.78	z	4405.2
16R-3, 55	136.54	x	4188.1
16R-3, 55	136.54	y	4118.1
16R-4, 101	138.50	x	4688.2
16R-4, 101	138.50	z	4639.2
16R-5, 75	139.69	x	4001.8
16R-5, 75	139.69	z	3760.1
17R-1, 28	143.08	x	4107.1
17R-1, 28	143.08	z	3932.8
17R-2, 32	144.62	x	3610.8
17R-2, 32	144.62	z	3317.8
18R-1, 56	152.96	x	5192.3
18R-1, 56	152.96	z	5072.1
18R-2, 3	153.90	x	3468.7
19R-1, 56	154.36	x	3732.9
19R-1, 56	154.36	z	3870.6
19R-1, 134	155.14	x	3338.5
19R-1, 134	155.14	z	3318.4
19R-2, 104	156.34	x	4651.9
19R-2, 104	156.34	z	4597.6
19R-3, 119	157.99	x	5153.9
19R-3, 119	157.99	z	5133.0
20R-1, 80	163.00	x	4584.6
20R-1, 80	163.00	z	4571.1
20R-2, 85	164.46	x	4378.4
20R-2, 85	164.46	y	4253.2
20R-3, 64	165.67	x	5224.1
20R-3, 64	165.67	z	5310.6
20R-4, 41	166.94	x	4223.3
20R-4, 41	166.94	z	3854.9
21R-1, 98	172.78	x	2715.0
21R-2, 104	174.27	x	2928.6
21R-2, 104	174.27	z	2739.3
21R-3, 47	175.20	x	2749.4
21R-3, 47	175.20	y	2806.3
21R-4, 60	176.83	x	2856.7
21R-4, 60	176.83	z	2785.1
22R-1, 117	182.57	x	3944.6
22R-1, 117	182.57	z	3999.8
22R-2, 28	183.17	x	4040.7
22R-2, 28	183.17	z	4082.7
22R-3, 138	185.77	x	4593.9
22R-3, 138	185.77	z	4466.8
23R-1, 109	192.09	x	4425.2
23R-1, 109	192.09	z	4444.1
24R-1, 87	193.57	x	4938.6
24R-1, 87	193.57	z	4965.4
24R-2, 112	195.32	x	4575.4
24R-2, 112	195.32	z	4596.5
24R-3, 115	196.85	x	4669.5
24R-3, 115	196.85	z	4671.8
24R-4, 112	198.25	x	4306.4
24R-4, 112	198.25	z	4447.9
24R-5, 64	199.24	x	4637.1
24R-5, 64	199.24	z	4674.0
25R-1, 40	201.00	x	5009.5
25R-1, 40	201.00	z	4942.8
25R-2, 70	202.80	x	4202.6
25R-2, 70	202.80	z	4338.2
26R-1, 32	210.52	x	3586.9
26R-1, 32	210.52	z	3589.2
27R-1, 47	220.27	x	4407.2
27R-1, 47	220.27	z	4579.3
28R-1, 98	224.98	x	4080.2
28R-1, 98	224.98	z	3892.4
28R-2, 98	226.26	x	2904.4
28R-3, 111	227.70	x	2724.6
28R-4, 52	228.57	x	2748.0
28R-4, 52	228.57	z	2721.6
29R-1, 78	230.38	x	4269.4
29R-1, 78	230.38	z	4700.0
29R-3, 4	232.51	x	4941.9
29R-3, 4	232.51	z	4954.2
30R-2, 37	241.07	x	2790.2
30R-2, 37	241.07	z	2776.0
30R-3, 16	242.16	x	2670.2
30R-3, 16	242.16	z	2762.4
30R-4, 76	244.26	x	2425.1
30R-4, 76	244.26	z	2403.3
32R-2, 124	261.24	x	4188.5
32R-2, 124	261.24	z	4149.9
33R-1, 26	268.36	x	3826.2
33R-1, 26	268.36	x	3813.7
34R-3, 68	273.29	x	2776.2
34R-3, 68	273.29	z	2726.2
34R-4, 71	274.79	x	2756.0
34R-4, 71	274.79	z	2782.7
34R-5, 76	276.27	x	2650.4
34R-5, 76	276.27	z	2678.6
35R-1, 70	278.40	x	2770.8
35R-1, 70	278.40	z	2752.9
35R-2, 106	279.76	x	2687.8
35R-2, 106	279.76	z	2706.0
35R-3, 45	280.26	x	2673.8
35R-3, 45	280.26	z	2713.9
35R-4, 64	281.95	x	3199.2
35R-4, 64	281.95	z	3051.5
35R-5, 138	284.19	x	2631.4
35R-5, 138	284.19	y	2682.6
35R-6, 120	285.51	x	2261.5
35R-6, 120	285.51	z	2213.1
36R-1, 35	287.65	x	3444.9
36R-1, 35	287.65	z	2802.9
37R-3, 142	295.83	x	3360.1
37R-3, 142	295.83	z	3573.4
37R-4, 46	296.37	x	3687.7
37R-4, 46	296.37	z	3849.9
38R-1, 57	297.47	x	5414.1
38R-1, 57	297.47	z	5186.7
38R-3, 5	298.59	x	5489.3
38R-3, 5	298.59	z	5647.6
38R-4, 43	300.47	x	5596.2
38R-4, 43	300.47	y	5436.8
39R-2, 134	303.63	x	5544.9
39R-2, 134	303.63	z	5819.0
39R-3, 106	304.85	x	5808.7
39R-3, 106	304.85	z	5667.4
39R-4, 43	305.55	x	5737.5
39R-4, 43	305.55	z	5721.4
40R-1, 35	306.85	x	5259.3
40R-1, 35	306.85	z	5117.4
40R-4, 32	310.20	x	4361.4
40R-4, 32	310.20	z	4114.6
41R-1, 43	311.53	x	4886.3
41R-1, 43	311.53	z	4784.6
41R-2, 26	312.83	x	3853.9
41R-2, 26	312.83	y	3843.5
41R-2, 26	312.83	y	3843.5
42R-1, 69	316.79	x	3554.7
42R-1, 69	316.79	z	3503.3
42R-2, 77	318.04	x	4593.9
42R-2, 77	318.04	z	4594.1
42R-3, 71	319.35	x	4687.3
42R-3, 71	319.35	z	4975.4

Note: This table is also available in **ASCII.**

Table T18. SIOSEIS process parameters for predictive deconvolution, bandpass filtering, and finite-difference migration.

```
Line 3:
  decon
    fno 2943 lno 2943 sedts 2.10 2.80 fillen .008 pdist .002 prewhi 1 double yes end
    fno 3000 lno 3060 sedts 2.02 2.80 fillen .008 pdist .002 prewhi 1 double yes end
    fno 3093 lno 3093 sedts 1.99 2.80 fillen .008 pdist .002 prewhi 1 double yes end
     end
  filter
    fno 1 lno 5062 pass 55 150 fillen 55 ftype 99 end
    end
  fdmigr
    fno 2943 lno 2943 vtp 1500 2.144 1500 2.163 1800 2.276 2100 3 dx 13.01 nx 421 bpad 100 epad 100 tsteps 2 .1 2.6 .005 end
    fno 2953 lno 2953 vtp 1500 2.119 1500 2.138 1800 2.246 2100 3 dx 13.01 nx 421 bpad 100 epad 100 tsteps 2 .1 2.6 .005 end
    fno 2963 lno 2963 vtp 1500 2.101 1500 2.120 1800 2.236 2100 3 dx 13.01 nx 421 bpad 100 epad 100 tsteps 2 .1 2.6 .005 end
    fno 2973 lno 2973 vtp 1500 2.091 1500 2.110 1800 2.226 2100 3 dx 13.01 nx 421 bpad 100 epad 100 tsteps 2 .1 2.6 .005 end
    fno 2983 lno 2983 vtp 1500 2.079 1500 2.098 1800 2.216 2100 3 dx 13.01 nx 421 bpad 100 epad 100 tsteps 2 .1 2.6 .005 end
    fno 2993 lno 2993 vtp 1500 2.068 1500 2.087 1800 2.206 2100 3 dx 13.01 nx 421 bpad 100 epad 100 tsteps 2 .1 2.6 .005 end
    fno 3003 lno 3033 vtp 1500 2.061 1500 2.080 1800 2.196 2100 3 dx 13.01 nx 421 bpad 100 epad 100 tsteps 2 .1 2.6 .005 end
    fno 3043 lno 3043 vtp 1500 2.059 1500 2.078 1800 2.196 2100 3 dx 13.01 nx 421 bpad 100 epad 100 tsteps 2 .1 2.6 .005 end
    fno 3053 lno 3053 vtp 1500 2.060 1500 2.079 1800 2.196 2100 3 dx 13.01 nx 421 bpad 100 epad 100 tsteps 2 .1 2.6 .005 end
    fno 3063 lno 3063 vtp 1500 2.056 1500 2.075 1800 2.186 2100 3 dx 13.01 nx 421 bpad 100 epad 100 tsteps 2 .1 2.6 .005 end
    fno 3073 lno 3073 vtp 1500 2.048 1500 2.067 1800 2.176 2100 3 dx 13.01 nx 421 bpad 100 epad 100 tsteps 2 .1 2.6 .005 end
    fno 3083 lno 3083 vtp 1500 2.041 1500 2.060 1800 2.176 2100 3 dx 13.01 nx 421 bpad 100 epad 100 tsteps 2 .1 2.6 .005 end
    fno 3093 lno 3093 vtp 1500 2.034 1500 2.053 1800 2.176 2100 3 dx 13.01 nx 421 bpad 100 epad 100 tsteps 2 .1 2.6 .005 end
    fno 3103 lno 3103 vtp 1500 2.030 1500 2.049 1800 2.176 2100 3 dx 13.01 nx 421 bpad 100 epad 100 tsteps 2 .1 2.6 .005 end
    fno 3113 lno 3113 vtp 1500 2.030 1500 2.049 1800 2.176 2100 3 dx 13.01 nx 421 bpad 100 epad 100 tsteps 2 .1 2.6 .005 end
    fno 3123 lno 3123 vtp 1500 2.031 1500 2.050 1800 2.176 2100 3 dx 13.01 nx 421 bpad 100 epad 100 tsteps 2 .1 2.6 .005 end
    fno 3133 lno 3133 vtp 1500 2.033 1500 2.052 1800 2.176 2100 3 dx 13.01 nx 421 bpad 100 epad 100 tsteps 2 .1 2.6 .005 end
    fno 3143 lno 3143 vtp 1500 2.033 1500 2.052 1800 2.176 2100 3 dx 13.01 nx 421 bpad 100 epad 100 tsteps 2 .1 2.6 .005 end
    fno 3153 lno 3153 vtp 1500 2.037 1500 2.056 1800 2.176 2100 3 dx 13.01 nx 421 bpad 100 epad 100 tsteps 2 .1 2.6 .005 end
    fno 3163 lno 3163 vtp 1500 2.044 1500 2.063 1800 2.176 2100 3 dx 13.01 nx 421 bpad 100 epad 100 tsteps 2 .1 2.6 .005 end
    end
Line 4:
  decon
    fno 4797 lno 4797 sedts 1.79 2.8 fillen .008 pdist .002 prewhi 1 double yes end
    fno 4840 lno 4840 sedts 1.84 2.8 fillen .008 pdist .002 prewhi 1 double yes end
    fno 4883 lno 4883 sedts 1.9 2.8 fillen .008 pdist .002 prewhi 1 double yes end
    fno 4952 lno 4952 sedts 2.02 2.8 fillen .008 pdist .002 prewhi 1 double yes end
    fno 4975 lno 4975 sedts 2.09 2.8 fillen .008 pdist .002 prewhi 1 double yes end
    fno 5000 lno 5000 sedts 2.12 2.8 fillen .008 pdist .002 prewhi 1 double yes end
    fno 5037 lno 5037 sedts 2.28 2.8 fillen .008 pdist .002 prewhi 1 double yes end
    end
  filter
    fno 1 lno 5062 pass 45 120 fillen 55 ftype 99 end
    end
  fdmigr
    fno 4797 lno 4797 vtp 1500 1.829 1500 1.848 1800 2.176 2100 3 dx 13.08 nx 441 bpad 100 epad 100 tsteps 1.8 .1 2.6 .005 end
    fno 4807 lno 4807 vtp 1500 1.841 1500 1.860 1800 2.176 2100 3 dx 13.08 nx 441 bpad 100 epad 100 tsteps 1.8 .1 2.6 .005 end
    fno 4817 lno 4817 vtp 1500 1.853 1500 1.872 1800 2.176 2100 3 dx 13.08 nx 441 bpad 100 epad 100 tsteps 1.8 .1 2.6 .005 end
    fno 4827 lno 4827 vtp 1500 1.867 1500 1.886 1800 2.176 2100 3 dx 13.08 nx 441 bpad 100 epad 100 tsteps 1.8 .1 2.6 .005 end
    fno 4837 lno 4837 vtp 1500 1.882 1500 1.901 1800 2.176 2100 3 dx 13.08 nx 441 bpad 100 epad 100 tsteps 1.8 .1 2.6 .005 end
    fno 4847 lno 4847 vtp 1500 1.897 1500 1.916 1800 2.176 2100 3 dx 13.08 nx 441 bpad 100 epad 100 tsteps 1.8 .1 2.6 .005 end
    fno 4857 lno 4857 vtp 1500 1.903 1500 1.922 1800 2.176 2100 3 dx 13.08 nx 441 bpad 100 epad 100 tsteps 1.8 .1 2.6 .005 end
    fno 4867 lno 4867 vtp 1500 1.911 1500 1.930 1800 2.176 2100 3 dx 13.08 nx 441 bpad 100 epad 100 tsteps 1.8 .1 2.6 .005 end
    fno 4877 lno 4877 vtp 1500 1.922 1500 1.941 1800 2.176 2100 3 dx 13.08 nx 441 bpad 100 epad 100 tsteps 1.8 .1 2.6 .005 end
    fno 4887 lno 4887 vtp 1500 1.952 1500 1.971 1800 2.176 2100 3 dx 13.08 nx 441 bpad 100 epad 100 tsteps 1.8 .1 2.6 .005 end
    fno 4897 lno 4897 vtp 1500 1.967 1500 1.986 1800 2.176 2100 3 dx 13.08 nx 441 bpad 100 epad 100 tsteps 1.8 .1 2.6 .005 end
    fno 4907 lno 4907 vtp 1500 1.987 1500 2.006 1800 2.176 2100 3 dx 13.08 nx 441 bpad 100 epad 100 tsteps 1.8 .1 2.6 .005 end
    fno 4917 lno 4917 vtp 1500 2.007 1500 2.026 1800 2.176 2100 3 dx 13.08 nx 441 bpad 100 epad 100 tsteps 1.8 .1 2.6 .005 end
    fno 4927 lno 4927 vtp 1500 2.026 1500 2.045 1800 2.176 2100 3 dx 13.08 nx 441 bpad 100 epad 100 tsteps 1.8 .1 2.6 .005 end
    fno 4937 lno 4937 vtp 1500 2.042 1500 2.061 1800 2.176 2100 3 dx 13.08 nx 441 bpad 100 epad 100 tsteps 1.8 .1 2.6 .005 end
    fno 4947 lno 4947 vtp 1500 2.056 1500 2.075 1800 2.186 2100 3 dx 13.08 nx 441 bpad 100 epad 100 tsteps 1.8 .1 2.6 .005 end
    fno 4957 lno 4957 vtp 1500 2.078 1500 2.097 1800 2.206 2100 3 dx 13.08 nx 441 bpad 100 epad 100 tsteps 1.8 .1 2.6 .005 end
    fno 4967 lno 4967 vtp 1500 2.110 1500 2.129 1800 2.236 2100 3 dx 13.08 nx 441 bpad 100 epad 100 tsteps 1.8 .1 2.6 .005 end
    fno 4977 lno 4977 vtp 1500 2.134 1500 2.153 1800 2.266 2100 3 dx 13.08 nx 441 bpad 100 epad 100 tsteps 1.8 .1 2.6 .005 end
    fno 4987 lno 4987 vtp 1500 2.144 1500 2.163 1800 2.276 2100 3 dx 13.08 nx 441 bpad 100 epad 100 tsteps 1.8 .1 2.6 .005 end
    fno 4997 lno 4997 vtp 1500 2.161 1500 2.180 1800 2.296 2100 3 dx 13.08 nx 441 bpad 100 epad 100 tsteps 1.8 .1 2.6 .005 end
    fno 5007 lno 5007 vtp 1500 2.187 1500 2.206 1800 2.316 2100 3 dx 13.08 nx 441 bpad 100 epad 100 tsteps 1.8 .1 2.6 .005 end
    fno 5017 lno 5017 vtp 1500 2.231 1500 2.250 1800 2.366 2100 3 dx 13.08 nx 441 bpad 100 epad 100 tsteps 1.8 .1 2.6 .005 end
    fno 5027 lno 5027 vtp 1500 2.275 1500 2.294 1800 2.406 2100 3 dx 13.08 nx 441 bpad 100 epad 100 tsteps 1.8 .1 2.6 .005 end
    fno 5037 lno 5037 vtp 1500 2.316 1500 2.335 1800 2.446 2100 3 dx 13.08 nx 441 bpad 100 epad 100 tsteps 1.8 .1 2.6 .005 end
    end
```

Note: Processing was performed in the order shown.